12-2021

Investigation of Optical and Structural Properties of GeSn Heterostructures

Oluwatobi Gabriel Olorunsola
University of Arkansas, Fayetteville

Investigation of Optical and Structural Properties of GeSn Heterostructures

A dissertation submitted in partial fulfillment
of the requirements for the degree of
Doctor of Philosophy in Microelectronics-Photonics

by

Oluwatobi Gabriel Olorunsola
Obafemi Awolowo University, Ile-Ife, Nigeria
Bachelor of Science in Engineering Physics, 2007
Western Illinois University, Macomb
Master of Science in Physics, 2013
University of Oklahoma, Norman
Master of Science in Geophysics, 2017
University of Arkansas, Fayetteville
Master of Science in Electrical Engineering, 2020

December 2021
University of Arkansas

This dissertation is approved for recommendation to the Graduate Council.

Shui-Qing Yu, Ph.D.
Dissertation Director

Gregory Salamo, Ph.D.
Dissertation Co-Director

Hammed Naseem, Ph.D.
Committee Member

Zhong Chen, Ph.D.
Committee Member

Mathew Leftwich, Ph.D.
Ex-Officio Member

The following signatories attest that all software used in this dissertation was legally licensed for use by Oluwatobi Olorunsola for research purposes and publication.

_____	_____
Mr. Oluwatobi Olorunsola, Student	Dr. Shui-Qing Yu, Dissertation Co-Director
	_____
	Dr. Gregory Salamo, Dissertation Co-Director

This dissertation was submitted to http://www.turnitin.com for plagiarism review by the TurnItIn company's software. The signatories have examined the report on this dissertation that was returned by TurnItIn and attest that, in their opinion, the items highlighted by the software are incidental to common usage and are not plagiarized material.

_____	_____
Dr. Mathew Leftwich, Program Director	Dr. Shui-Qing Yu, Dissertation Co-Director
	_____
	Dr. Gregory Salamo, Dissertation Co-Director

Abstract

Silicon (Si)-based optoelectronics have gained traction due to its primed versatility at developing light-based technologies. Si, however, features indirect bandgap characteristics and suffers relegated optical properties compared to its III-V counterparts. III-Vs have also been hybridized to Si platforms but the resulting technologies are expensive and incompatible with standard complementary-metal-oxide-semiconductor processes. Germanium (Ge), on the other hand, have been engineered to behave like direct bandgap material through tensile strain interventions but are well short of attaining extensive wavelength coverage. To create a competitive material that evades these challenges, transitional amounts of Sn can be incorporated into Ge matrix to form direct bandgap GeSn alloys that have led to the increasing possibility of engineering a suite of low-cost, light emission sources that applies to a wide range of infrared photonics and optoelectronics systems. Hence, the importance of studying the structural and optical properties of these GeSn heterostructures cannot be overemphasized.

The first part of this dissertation investigates the structural and optical properties of SiGeSn/GeSn/SiGeSn quantum wells (QWs) where the photoluminescence (PL) behaviors of thick (22 nm in well) and thin (9 nm in well) GeSn QW samples are compared. Using PL results from two excitation lasers (532 nm and 1550 nm lasers) as well as studying their respective optical transitions, the result reveals that the thicker well sample shows i) a more direct bandgap outcome in addition to a much lower ground energy Γ valley; ii) a higher carrier density within the well, and iii) an increased barrier height coupled with improved carrier confinement. All of these resulted in a significantly enhanced emission that allows for the first-ever estimation of GeSn QWs quantum efficiency (QE) while also suggesting a path towards efficient mid-infrared devices.

To further improve the carrier confinement while also reducing the carrier leakage in the thicker well design, a SiGeSn/GeSn/GeSn/SiGeSn separate confinement heterostructure (SCH) is introduced. The sample is characterized and the optical properties are compared with the previously reported 9 nm and 22 nm well non-SCH samples. Based on the optical transition analysis, the SCH QW also shows significantly higher carrier confinement compared to reference samples. In addition to these studies, an attempt is made to investigate advanced quantum well structures through an all-inclusive structural and optical study of SiGeSn/GeSn/SiGeSn multi-quantum wells (MQWs). The resulting analysis shows evidence of intermixing diffusion during growth.

The second part of this work provides insights into the behavior of annealed GeSn bulk samples near the indirect-to-direct transition point. The study attempts to provide connections between the strain, composition, and defect densities before and after annealing. The result reveals the impact of annealing on a sample may either i) lower the strain giving rise to an increased PL while reducing the energy separation or ii) introduce misfit dislocation/ surface roughness leading to an affected or decreased PL.

Finally, this work also explores the low-temperature capability of our in-house plasma-enhanced ultra-high vacuum chemical vapor deposition system through the growth of Si-on-Ge epitaxy and pressure-dependent growth of GeSn bulk heterostructures.

Acknowledgment

As I pen the last few of my time here in Fayetteville, Arkansas, I'm reminded of the scripture that says; "Except the Lord builds the house, those that build, build in vain'' (Ps. 127:1) My life till as I write, is a testament of the Almighty's faithfulness, a succession of unfettered graces, and everything that gave same grace the fullest expression of the times and seasons that led to this doctoral degree. Humbled by the many events of the last decade and enamored in the confidence that God always has a plan. He has never failed. He will never fail!

While the unpopular decision to pursue a Ph.D. hasn't been the easiest, I have been blessed by an advisor that makes excellence an everyday mantra. Dr. Yu's enthusiasm, dedication and vision for semiconductor research is matchless and certainly needs mention in the historical timelines of (Si)GeSn research! Through him, I have learned the detective's paradigm – A mindset that readily questions an objective till it births sought and unsought revelations while inspiring new ways of innovative thinking. While there are quite a few more genius to moon over Dr. Yu's strategic visionary, I am profoundly grateful for the gift of a co-advisor, Dr. Gregory Salamo. As one who has been away from my home country for nearly a decade, I'm endlessly chuffed by the blessing of having a father and an advisor in one person. Very few advisors are as humble – a very likeable persona that makes him a special kind of amazing! Dr. Salamo's pedagogy is one that emphasizes critical thinking, voracious curiosity and a constant chase for truth in data. A story-teller per excellence and an all-round blessed researcher with far too many accomplishments to show for it.

While it is far too uncommon to have two-member doctoral committees in academia, I'm reminded of the completion of a five-membered committee brings to the experience, my immense gratitude goes to Dr. Hameed Naseem (The Great One – and easily one of my best

Professors of all time), Dr. Zhong Chen and Dr. Mathew Leftwich. I'm thankful for these ones, their availabilities and the critical assessment of my candidacy and defense presentations. Special, special thanks go to the incredible Dr. Wei Du (Wilkes University) for needed help offered me during the manuscript writing and review process. I also appreciate the incredible contributions of Dr. Baohua Li and Dr. Aboozar Mosleh to my research work. My appreciation also goes to past a current member of Yu's lab between 2018 and 2021: Dr. P.C. Grant, Dr. Bader Alharthi, Dr. Wei Dou, Dr. Yiyin Zhou (Angel in human form), Dr. Huong Tran, Dr. Abass Sabar, Solomon Ojo, Abass Grey Abernathy, Joshua Grant, Sylvester Amoah, Emmanuel Wangila, Abdulla Ali, Alexander Golden, Sudip Acharya and Justin Rudie.

The research was partially supported by Air Force Office of Scientific Research (AFOSR) under contract number FA9550-18-1-0045, and FA9550-19-1-0341. Any opinions, findings, and conclusions or recommendations expressed in this material are those of the author and do not necessarily reflect the views of the AFOSR.

In this distant place, I have learnt the true meaning of a thriving and supportive community (Family). These ones, these angels that show up when you are at the tail end of letting away: Solomon and Olamiposi Ojo, Abayomi and Abigail Omolewu, Afolabi Olomola, Drs. Oluwaseyi and Dolapo Ogunsola, Aunty Oluremi Kuti, Aunty Biodun Olusola, Omolayo Bada, Dr. Olanrewaju Aboaba, and Ademide Mabadeje, David Sumbo Onifade, Rudy Acosta, Olivia Kolenc, Mona Alli, and Oluwaseye Dada. Because of the example set by my parents and siblings, I have learned to appreciate life, the love of God, and the drive to succeed. I've grown as a person because of their selfless act of love, and I'm grateful for it. I'm eternally grateful for that and everything else. To my siblings, Oluwatoni (& Olalekan Bamiteko) and Oluwatosin (&

Adetutu Olorunshola). Thanks for believing in me, and thanks for taking care of our parents while I was gone. I'm beyond blessed to have you in my life!

Dedication

To my Lord Jesus Christ,
The center of my life and my reason for my being.

To Mum and Dad,
Bamitale & Shola,
The fighters of my wars

To the men and women in my corner,
Indeed, there are angels in distant places.

To Tosin & Toni,
The color and the wing.

Every storm truly runs out of rain…

- Maya Angelou

Table of Contents

List of Figures

List of Table

List of Published and Planned Papers Used in this Dissertation

Part of Chapter 3 was originally published as:

> Reprinted with permission from "Impact of Long-Term Annealing on Photoluminescence from $Ge_{1-x}Sn_x$ Alloys" Olorunsola O, Stanchu H, Ojo S, Pandey K, Said A, Margetis J, Tolle J, Kuchuk A, Mazur Y I, Salamo G and Yu S-Q *Crystals* 11 905 (2021) with the permission of MDPI Publishing.

Part of Chapter 4 was originally published as:

> Reprinted with permission from "Investigation of SiGeSn/GeSn/SiGeSn single quantum well with enhanced well emission" Oluwatobi Olorunsola, Wei Du, Solomon Ojo, Grey Abernathy, Yiyin Zhou, Sylvester Amoah, P.C. Grant, Wei Dou, Joe Margetis, John Tolle, Baohua Li, Yong-Hang Zhang, and Shui-Qing Yu, Nanotechnology (2021) with the permission of Nanotechnology

Part of Chapter 5 was originally submitted as:

> "Enhanced carrier confinement of GeSn single quantum well towards all-group-IV photonics applications Oluwatobi Olorunsola, Abdulla Said, Solomon Ojo, Grey Abernathy, Samir Saha, Emmanuel Wangila, Hryhorii Stanchu, Joe Margetis, John Tolle, Wei Du, Baohua Li, and Shui-Qing Yu, APL (2021)

Part of Chapter 6 was originally submitted as:

> "Optical and structural properties of multiple quantum wells for infrared optoelectronics" Oluwatobi Olorunsola, Hryhorii Stanchu, Abdulla Said, Solomon Ojo, Emmanuel Wangila, Mohammad Alavijeh, Gregory Salamo, and Shui-Qing Yu, submitted to APL (2021)

Chapter 1: Introduction

1.1 Background

Recent material development breakthroughs in GeSn technology have led to the increasing possibility of engineering a suite of low-cost, valuable and efficient detection devices and light emission sources that can be applied to a wide range of infrared photonics and optoelectronics systems. Although, the elevated significance of Moore's law sustained progressive novelties in the microelectronics community over a decade ago, its current regressed practicality in the face of fast-paced developments is starkly dwarfed by the parasitic competition between device performance and miniaturization efforts. The revival or hitherto renaissance of arguably the most-popularized law of modern times is largely dependent on a new field of semiconductor physics (Si photonics). Since the failure of Moore's law was shunted by the limitation of metallic interconnects in providing efficient data transmission, the use and replacement of it with light-enabled optical interconnects in miniaturized systems has given rise to high-speed, low-cost and efficient data transfers [1–3] – An inestimable technological revolution of today's optoelectronics and photonics technology made possible by the monolithic integration of photonic chip on complementary metal oxide (CMOS) platform/chip.

Early realization of this innovation initiated the idea to create a suite of integrable photonic devices such as detectors, emitters, modulators and switches on Si platforms. Since one of the criterium for achieving efficient light source is a direct bandgap material, the integration of Si and Ge, which are indirect bandgap materials will prove ineffective for this application. Figure 1.1 below shows an array of optoelectronics devices on a silicon platform. The image was modified after Soref et al's 1993 envisioned integrated architecture [4].

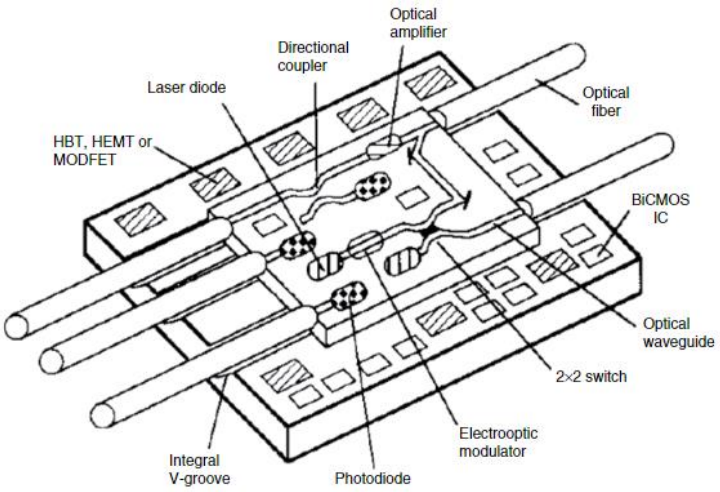

Figure 1.1. Idealized Si-based platform with a suite of integrated optoelectronic devices [4]

While concerted efforts has birthed critical components on the envisioned architecture, the creation of a reliable and efficient light emission source integrated to a silicon platform is still far-regressed. In contrast to these efforts, competing light-emitting products in the market such as III-V materials on InP platforms are currently leading the light-emitting space and are far ahead in performance and sophistication. Of course, the limitation of these technologies is that they are expensive and incompatible with current CMOS processes. To create a light-based system that functions correctly with CMOS processes, early researchers introduced the integration of III-V materials such as InP [5] and/or GaAs [6] on Si platforms using wafer-bonding [7] or selective area growth strategies [5].

Regarded as hybrid silicon lasers, these III-V/Si laser-based devices suffer from differences in thermal coefficients, lattice constants and chemical polarity, all of which can drive the immediate cost of fabrication up. Besides these identified limitations, other factors such as the complicated sets of fabrication procedures as well as the fragility of III-V materials has made them difficult to use and impractical to attain a potential electronic revolution.

Group IV alloy material systems (specifically GeSn and SiGeSn alloys) on the other hand offers the advantage of low-cost fabrication commitment, chemical and physical compatibility with Si platforms and seamless monolithic integration to Si substrate to form functional optoelectronic systems that has a comparatively higher device performance and reliability.

Although traditional group IV elements such as Si and Ge possess indirect bandgap natures with low optical emission efficiencies, GeSn binary alloys of appropriate Sn compositions (> 8%) can be engineered or tuned to behave like direct bandgap material suitable for light emission practicalities [8,9] while also covering a wide range of spectral reach up to the infrared spectrum from 2 up to 12μm [10]. Figure 1.2 (a) shows a GeSn alloy material with Sn composition of ~8%. As clearly depicted, there are more carrier populations in the L valley characteristically exhibiting the behavior of an indirect bandgap materials based on Sn composition. Above the 13% Sn composition (Figure 1.2 (b)), the material crosses the transition point to exhibit a direct bandgap property with more carriers in the Γ valley which will eventually lead to a faster recombination process.

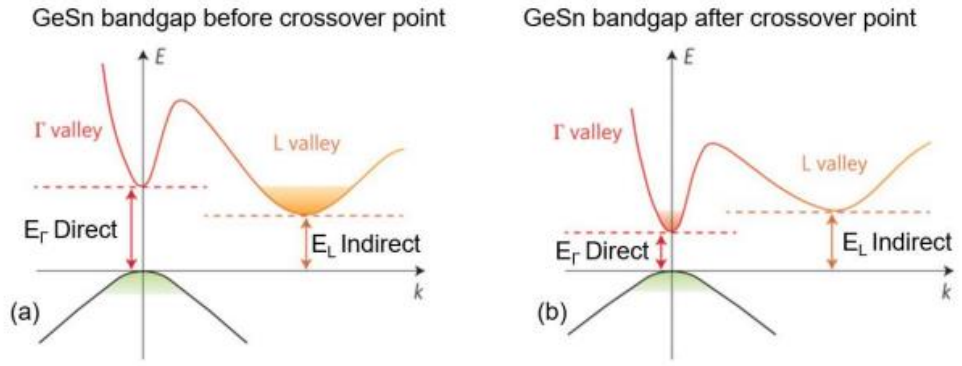

Figure 1.2. Band diagram of a strain-relaxed GeSn alloy (b) before (b) after the transition point [11].

While the uniqueness of the GeSn lies in the inherent ability to engineer its bandgap by tuning the Sn incorporation, another exceptional attributes that makes it seamless for monolithic integration to CMOS processes is its potential for low temperature epitaxial growth.

It is noteworthy to mention the economic benefits of the Group IV alloy materials, especially within the application scope of the Si photonics industry. With the exception of a well-developed room-temperature light-based source[12,13], other components such as photodetectors, modulators, waveguide and switches have reached market-level product maturity. Currently the Si photonics market is projected to exceed about $1.5 billion in 2025 [14]. Due to its immense economic potential, the American Institute for Manufacturing Integrated Photonics (AIMS Photonics) invested about $0.6 billion in year 2015 as a five-year seed investment aimed to transform academic innovations to commercialization photonics and optoelectronics products [15].

Early predictions favored the viability of (Si)GeSn binary and ternary for photonic and optoelectronic device applications. Among these are the notable contributions of R.A. Soref and C.H. Perry that used the energies of $Si_{1-y}Ge_y$, $Si_{1-y}Sn_y$ and $Ge_{1-x}Sn_x$ to theoretically predict the existence and possible variations of compositionally-dependent indirect and direct $Si_{1-x-y}Ge_xSn_y$ bandgaps [16]. Two years after their novel discovery, the work of L. Friedman and R.A. Soref led to the proposal of direct bandgap GeSn/Ge/Si and Ge/GeSn/Si heterostructures [17].

It is also noteworthy to emphasize that each sub-band region of the extended 12-micron SiGeSn material/device functionality can be targeted to different applications depending on their respective wavelengths of operation. This extensive wavelength capability has also found application use in missile tracking and atmospheric transmission systems. Despite the extensive commercial potential of this material, a number of challenges still needs to be attended to

compete with state-of-art commercial technologies. While these challenges are gradually being solved, some solutions have resulted in GeSn-enabled applications. For instance, the fabrication of a novel GeSn-pixeled focal plane array with a characteristic operation IR wavelength range of 1.5-3.0 μm has been demonstrated to apply to night vision and photodetection devices [18]. In addition, advances in GeSn laser development have also featured considerable performance improvements. These include: i) the achievement of continuous wavelength at low temperature up to 70 K [19]; ii) 2-3 μm lasing spectrum coverage with tunable emission wavelength [20] iii) the operational lasing temperature near room temperature (RT) under pulse pumping conditions [21,22], and more recently; iv) the discovery and demonstration of the first electrically injected edge emitting laser operating at lasing temperature of up to 100 K [23]. While considerable low threshold has been achieved for bulk GeSn materials, incremental contributions to instigate a lower threshold and higher device performance is currently being pursued through novel GeSn/SiGeSn QW heterostructure designs [24].

Generally, the SiGeSn material system is still very much understudied owing to challenges in growth (low temperature and material stability), characterization (structural and optical), and device fabrication. This work wholly investigates challenges relating to post-growth stability and optical property improvements through the optimization of GeSn/SiGeSn QWs.

It should be noted that binary and ternary versions of the Si-Ge-Sn material system are not exclusive supplements to each other. While the GeSn binaries have limited alloy compositions to achieve direct bandgap possibilities, ternary SiGeSn alloys on the other hand possess far more degrees of freedom since their bandgaps and lattice constant can be tuned extensively by simultaneously varying the Si, Ge and Sn compositions. Figure 1.3 below shows the bandgap dependence on the lattice constants of different semiconductor alloys and elements.

This figure validates the uniqueness of SiGeSn alloys in covering an extensive energy band covering the entire infrared spectrum, from near IR to mid-IR to far-IR (2-12 μm) and is realized under high injection through an Auger-assisted band-to-band transitions.

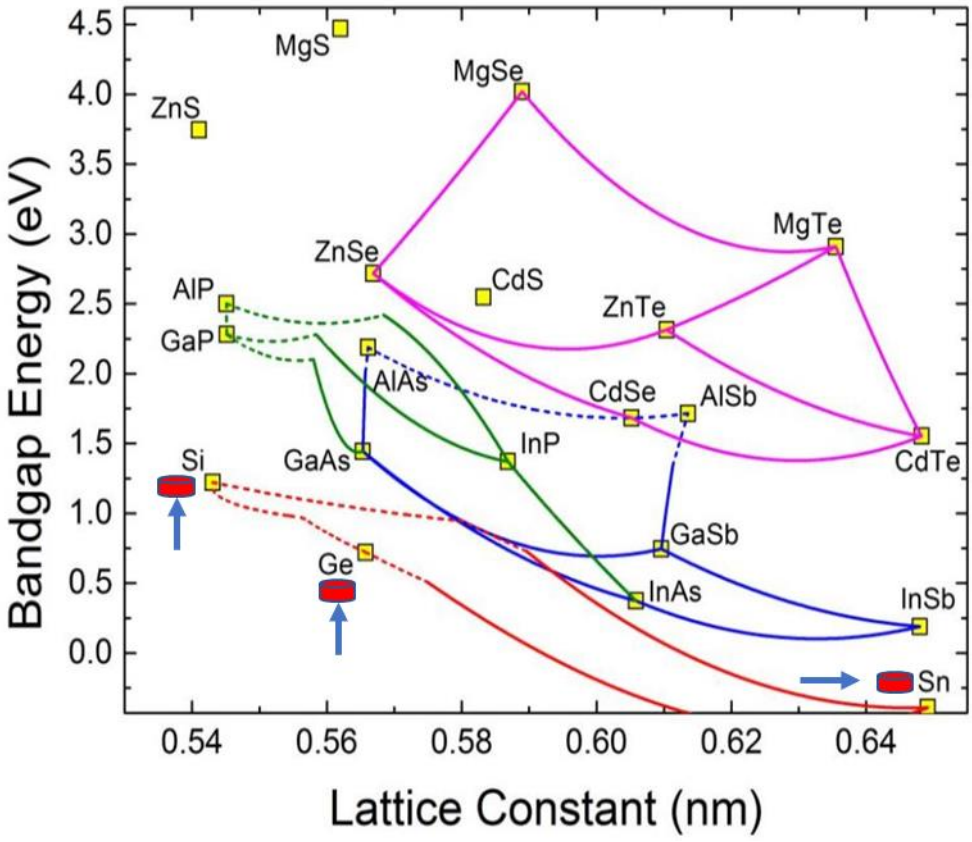

Figure 1.3. Bandgap dependence on the lattice constants of different semiconductor alloys and elements. Notice the arrowed-cylinder benchmarks on the Si, Ge and Sn.

In addition to these, the requirement of an ultra-high-quality growth is a major factor in realizing the full broad range IR wavelength. However, the current material development suffers greatly from a number of growth challenges ranging from low solid solubility limitations of α-Sn in Ge and Si (< 1%), Sn instability at temperatures above 13.2°C [25,26], large lattice mismatch between Si, Ge and Sn to large GeSn-on-Si lattice mismatch. Furthermore, for SiGeSn optoelectronics devices to attain full industry acceptance, low temperature objectives of < 400°C

are required since at this temperature CMOS process compatibility is achieved. A number of growth strategies have been employed to ratify the low temperature and high Sn incorporation issues. These range from the use of low-cost gas precursors to the utilization of plasma-assisted technologies to engaging pressure-dependent strategies. This work also explored the low-temperature capability of our chemical vapor deposition (CVD) machine, through the growth of Si on Ge before transitioning to a systematic pressure-dependent objective that aims to improve Sn incorporation at higher than already explored pressures (2-15 torrs).

1.1.1 Band Structure of GeSn alloy

Ge is an indirect bandgap material since the L-valley of conduction band (CB) minima is not only aligned with the highest curvature of the valence band (VB) but also the closest to it. α-Sn, on the other hand is a semi-metal and manifests a negative bandgap material in its 'cooled' diamond structure state. While the conduction band minimum of Sn at the T-valley exhibits a negative bandgap of -0.41 eV characterized by its T-valley 'sitting' below the VB minima, the minima of indirect Ge T-valley is above the minima of the VB (~0.79 eV). The effect of the band character of Sn is easily observed in Ge band structure as it experiences a shrinkage in both the direct (Γ-valley) and indirect (L-valley) components of its conduction band (CB) with the direct valley shrinking more rapidly than the direct L-valley band. Figure 1.4 shows that the band structures of the two elements. The direct bandgap character of the GeSn alloy is determined by the amount of Sn composition applied to a Ge matrix. The ability to change the bandgap by simply tuning the Sn composition has resulted in the today's technological breakthrough for GeSn-based photonics and optoelectronics devices.

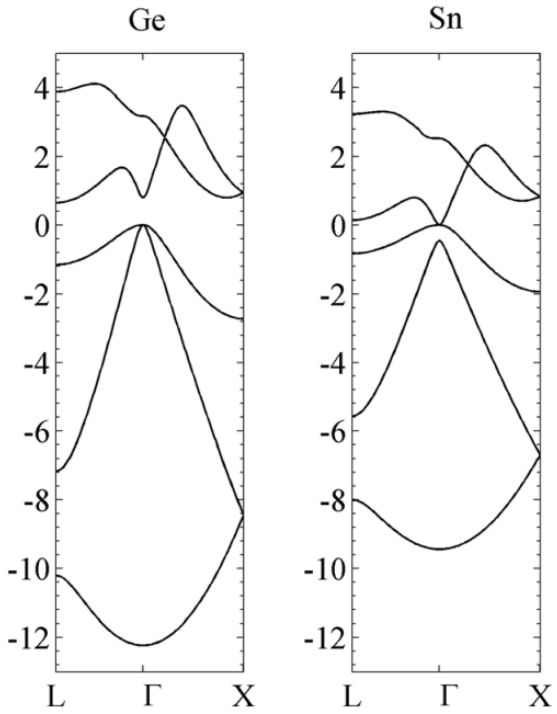

Figure 1.4. Band Structure of bulk Ge and α-Sn [27]

The effect of the variation of the Sn composition on the direct and indirect bandgap character of the GeSn alloy is provided by the Vegard's law expressions below:

For direct bandgap:

$$E_g^{\Gamma}(Ge_{1-x}Sn_x) = E_{gSn}^{\Gamma}(x) + E_{gGe}^{\Gamma}(1-x) - b_{GeSn}^{\Gamma}x(1-x) \qquad \text{(Equation 1.1)}$$

For Indirect bandgap:

$$E_g^{L}(Ge_{1-x}Sn_x) = E_{gSn}^{L}(x) + E_{gGe}^{L}(1-x) - b_{GeSn}^{L}x(1-x) \qquad \text{(Equation 1.2)}$$

where E^{Γ}_{gGe} and E^{Γ}_{gSn} and are direct bandgap energies of Ge and Sn respectively, with and E^{L}_{gGe} and E^{L}_{gSn} representing the indirect bandgap energies of Ge and Sn. The bowing parameters, b^{L}_{GeSn} and b^{Γ}_{GeSn} also represents the indirect and direct components of the parameters. The summarized values of all the parameters are shown in Table 1.1.

Table 1.1. Bandgap energies and bowing parameters for Ge, Sn and GeSn alloy.

E^{Γ}_{gGe} (eV)	E^{Γ}_{gSn} (eV)	E^{L}_{gGe} (eV)	E^{L}_{gSn} (eV)	b^{Γ}_{GeSn} (eV)	b^{L}_{GeSn} (eV)
0.79	-0.41	0.66	0.09	2.92	0.68

1.1.2 SiGeSn Material System

As previously discussed, the incorporation of group IV Sn element into Ge matrix (GeSn) and now SiGe alloys (SiGeSn) will result in direct bandgap materials. Clearly, GeSn and SiGeSn direct bandgap characters are achieved due when transitional amounts of Sn are incorporated. This transformative prowess of the Sn element is possible due to its unique optical property. For instance, the energy bandgap of Sn consists of overlapping conduction and valence bands exhibiting a zero-bandgap character at the Γ valley position in momentum space [28]. A commonplace knowledge of Sn is that it morphs into white metallic form or the so-called β-Sn phase body-centered tetragonal crystal geometry at room temperature exhibiting a negative bandgap character (-0.41 eV bandgap). Upon cooling below 13.2^{o}C, β-Sn affectedly undergoes a phase transformation to become a more stable diamond structure α-Sn (or gray Sn) with semiconducting properties [29]. The pioneering record of metastable Sn growth was achieved in 1981 by a group of material scientists led by R.F.C Farrow [30]. In their work, molecular beam epitaxy (MBE) machine was used to realize near-lattice matched heteroepitaxial growth of α-Sn to CdTe and InSb substrates. Learnings from this work was then applied to Ge crystals by incorporating Sn into it since Ge and Hg-Cd-Te materials system possess similar material properties [25,26]. The impact of the Sn in the Ge matrix has been previously emphasized but now it is clear that the specific reason is due to the negative bandgap character of the Sn that makes for a direct bandgap GeSn material.

The expression for estimating the lattice constant of a bulk GeSn alloy material is represented below through Vegard's law [31]:

$$a_{GeSn} = a_{Ge}(1-x) + xa_{sn} + bx(1-x) \qquad \text{(Equation 1.3)}$$

where the lattice constants of the Germanium and Tin are 5.657 and 6.489 Å respectively [32]. The parameter, *b*, is referred to as the bowing parameter (usually 0.066 Å) [33] and accounts for the deviation in the measured experimental values of the lattice constant and the Vegard's law estimation. The deviation typically stems from the effect of the strain-induced deformation of the crystal structure. Estimated lattice mismatch values from the growth of GeSn-on-Si substrate is within the range of 4.48% to 19% while that of GeSn-on-Ge buffer is between 0.41% to 15%. The effect of GeSn-on-Si typically accelerates strain and defect occurrence more than GeSn-on-Si growths. An additional growth that is yet mentioned is the prevalence of Sn surface segregation at high growth temperatures. This events limits/reduces Sn composition close to the sample's interfacial regions while also giving rise to the formation of surface level droplets which are strongly inimical to device performance [32,34].

The epitaxial deposition of (Si)GeSn alloys has been explored across variegated growth schemes and systems. For instance, a number of publications has demonstrated the practicality of these growths using magnetron sputtering techniques [35], molecular beam epitaxial approach [36–40] as well as the renowned chemical vapor deposition (CVD) method [41–46]. Although, the CVD products mentioned these references were deposited using higher hydrides precursors (Si_xH_{2x+2} and $Ge_xH_{2x+2)}$ which are either expensive or are not compatible with industry-wide systems and use. While SnD_4 (Stannane) and $SnCl_4$ (Tin tetrachloride) are the most applied Sn precursors, $SnCl_4$ is unique in the sense that it forms by-products of HCl upon reaction with Sn

and Ge precursors and also functions as an etching agent that etches Ge more rapidly than Si [47].

The structural explanation for what happens when Sn is introduced into Ge is that strain is built up or introduced in the process. The strain deforms the periodic potential with a reduction in the energy separation between T and the L valleys as well as the splitting the heavy hole (HH) and the light hole (LH) in the valence band (VB). The direct effect of the introduced tensile strain is that it shortens the Γ and the L valleys, but shrinks the Γ valley faster to result in a direct GeSn bandgap material. The next question is what happens to the GeSn alloy when Si is introduced to it? Well, first things first, it becomes ternary SiGeSn material to result in a much-separated conduction and valence band. Figure 1.4 below illustrates this behavior accordingly. An advantage of the formation of SiGeSn is that it improves the thermal stability of GeSn binaries making them suitable for high temperature applications without Sn segregation events [46]. The identified merits of growing SiGeSn alloys makes them apt for space photovoltaic applications [48]. Although the merits of these ternary materials apply appreciably, growing these materials presents a higher level of difficulty compared to GeSn growths. SiGeSn alloys are grown at higher temperatures since Silane can only breakdown at far higher temperatures [48]. Sn also suffer immense stability issues in SiGe owing to large atomic size difference between Si and SiGe [49]

1.1.3 GeSn Quantum Wells

Efficient light emitting GeSn photonics devices can be realized through the structural optimization of current GeSn bulk materials or the introduction of advanced structures such as quantum wells. The latter is vastly adopted given their proven abilities to improve light emission efficiencies while increasing carrier and optical confinements. A number of designs have been

explored to create GeSn laser devices [20,50,51], but issues such as carrier leakage, relatively low emission efficiencies and device instability still persists opening up opportunities for future innovative solutions. As such, a fuller understanding of the SiGeSn material system is required solve this challenge. While there are still a lot of need gaps to the fill, the exploration of these novel material optimization design strategies was adopted to achieve significant progresses that created Type-I direct bandgap QWs structures.

For instance, to create an all group IV QW structure, candidate barrier types were used. In one case, Ge was used as a barrier while GeSn and SiGeSn barriers were used in other cases. The adoption of Ge as barrier in a Ge/GeSn QW system has been vastly reported in previous studies [42,52–58]. Summarized versions of these body of work revealed that a direct bandgap material cannot be realized due to the large compressive strain in the QW well. The authors also proposed the use of GeSn as barriers to mitigate this challenge [59]. Interestingly, this strategy worked as it eased the compressive strain while also achieving a direct bandgap QW with Type I band-alignment. However, beyond a compositional alloy range the material fails giving rise to the suggestion of SiGeSn barrier.

The introduction of the SiGeSn barrier opens up a wide range of possibilities since their lattice parameters and bandgaps can be engineered by tuning the Si and Sn compositions. Although, the SiGeSn/GeSn are slightly more stable than the previous design adoptions they still suffer from carrier leakage inefficiencies. To solve this challenge, an incremental design strategy was suggested to increase the thickness of the GeSn QW which significantly improved the PL emission [60]. To further improve PL emission and carrier confinement with reduced leakage, a separate confined heterostructure was suggested. The details of the last two strategies are presented in subsequent chapters of this dissertation.

1.2 Dissertation Organization

This dissertation discusses the structural and optical properties of GeSn heterostructures. The chapters are organized in the order presented below:

Chapter 2 discusses the growth and characterization techniques used in this dissertation. The unique capabilities of the ultra-high chemical vapor deposition (UHV-CVD) and reduced-pressure chemical vapor deposition (RP-CVD) systems are also discussed. The underlying theory of the characterization methods as well as their working principles also covered. As part of the optical properties theme, Chapter 3 investigates the optical emission properties of SiGeSn/GeSn quantum well materials where the PL properties of thick and thin QW samples are compared. The introductory part of this work presents a thorough review of past literatures followed by a summarized version of the growth and structural characteristics of the samples. The optical properties are then analyzed using photoluminescence data from both 532 nm and 1550 nm excitation lasers. The chapter ends with the first-ever reported calculation of the quantum efficiency. The theory and experimental background of this portion of the work are also discussed accordingly. Following similar theme, Chapter 4 compares the PL emission of the QW samples in Chapter 4 to a newly grown separate confined heterostructure (SCH) quantum well samples under low power injections. The results were compared and analyzed.

Chapter 5 attempts to provide insights into the behavior of annealed GeSn bulk samples near the transition point. The study attempts to provide connections between the strain, composition and defect densities before and after annealing. The impact of annealing on PL of samples with Sn compositions near the indirect to direct optical transition points were analyzed and discussed accordingly. In Chapter 6, an experimental account of the impact of QW intermixing on the PL emission of multiple quantum well (MQWs) samples are discussed. X-ray

diffraction (XRD), Secondary Ion Spectrometry (SIMS) and modeled defect density data were thoroughly analyzed for connections. Chapter 6 seems to provide some insights into why higher period QWs suffer from reduced PL intensities.

Chapter 7 explores the low-temperature capability of our in-house ultra-high chemical vapor deposition (UHV-CVD) machine, through the growth of Si on Ge before transitioning to a systematic pressure-dependent objective that aims to improve Sn incorporation at higher than already explored pressures (2-15 Torrs). Finally, a summary of the dissertation as well as the future work strategies are presented.

Chapter 2: Growth techniques and characterization methods

2.1 Introduction

This chapter introduces the reader to the growth deposition and characterization technologies used in this dissertation. In appropriate order, the ultra-high chemical deposition (UHVCVD) and reduced pressure chemical deposition (RPCVD) machines were discussed with primary focus on their operational and componential uniqueness. The low-epitaxy Si and pressure-dependent GeSn growths are accomplished using our in-house UHVCVD system, while majority of the quantum well (QW) growths were carried out using by commercial RPCVD machines. Summarized overview of the respective of structural and optical characterization methods used are provided in subsequent sections where the underlying theoretical frameworks and working principles of each technique are explained accordingly.

2.2 Ultra-high vacuum Chemical Vapor Deposition System (UHCVD)

The later portion of this dissertation explores low temperature Group IV elemental and alloy thin films epitaxial deposition using a customized UHVCVD system developed at the University of Arkansas, Fayetteville. Unique system functionalities and operational procedures are designed to accommodate research exploration objectives such as is uncommon to traditional CVD assemblies. For research purposes, the state-of-the-art assembly design was adopted to study the growth mechanism of the group IV elemental and alloy deposition; and more specifically, provide in-situ and ex-situ accounts of the strain behavior, atomic ordering and stability dynamics while aiming for higher Sn incorporation that favors exceptional device performance. The unique capabilities of our UHCVD system are provided as follows:

i) Double-chambered stainless-steel enclosures: The connected stainless-steel system consists of a double-chambered load-lock and process system with sub-atmospheric pressure capacities in the order of 10^{-9} to 10^{-10} torrs.

ii) Broad-range deposition pressure usage: With an extensive deposition pressure range it is possible to simulate growth realities in sub-atmospheric, atmospheric, reduced pressure conditions.

iii) Diagnostics, Etching and plasma-enhanced technologies: These integrated components are generally responsible for the low-temperature epitaxial objectives and process chamber 'hygiene' procedures of the machine. Armed with a combination of RF and remote plasma sources, the plasma etching capability takes care of ensuring the system is cleaned and prepped for vacuum, while the RF plasma produces low plasma radicals to speed up the reaction dynamics.

iv) Hotwire and atomic hydrogen technologies: This exclusive system functionality is one of the most prominent differentiators of this system since it engages tungsten-assisted filaments to ease the hydrogen desorption process pre-epitaxy. The machine system can also generate atomic hydrogen from hydrogen gas through a catalytic activation process.

v) Cold-wall requirement: With the cold-wall capability, the possibility of depositions clinging to the chamber walls are lowest, especially in situations when multiple elemental compositional variations are applied.

vi) Rapid thermal annealing (In-situ): Strain-relaxed films and reduced-defect objectives are realized using an in-built annealing arrangement that connects to the machine's substrate holder.

vii) Substrate Holder (Customized): Customized to fulfil the above annealing objective, the substrate holder design is also customizable to a plethora of substrate sizes.

viii) Sample Probe (Customized): In-situ reactive radical monitoring is possible with the customized mass-spectrometry enabled-sampling probe.

ix) Adaptable precursor gas delivery system: The system consists of a unique gas mixing system that customize to SnD_4 and $SnCl_4$ precursor gases. Precise and extended dilution ratios are achieved using technologies that allows for controlled gas flow rates and gas phase monitoring.

Figures 2.1 and 2.2 shows the UHVCVD system schematics, the image of the machine, and the gas mixing system. Other system components such as the gas reactor columns and pumps are shown. The pictures are taken in the current working states of the CVD assembly. The next section discusses the merits and capabilities of the RP-CVD system.

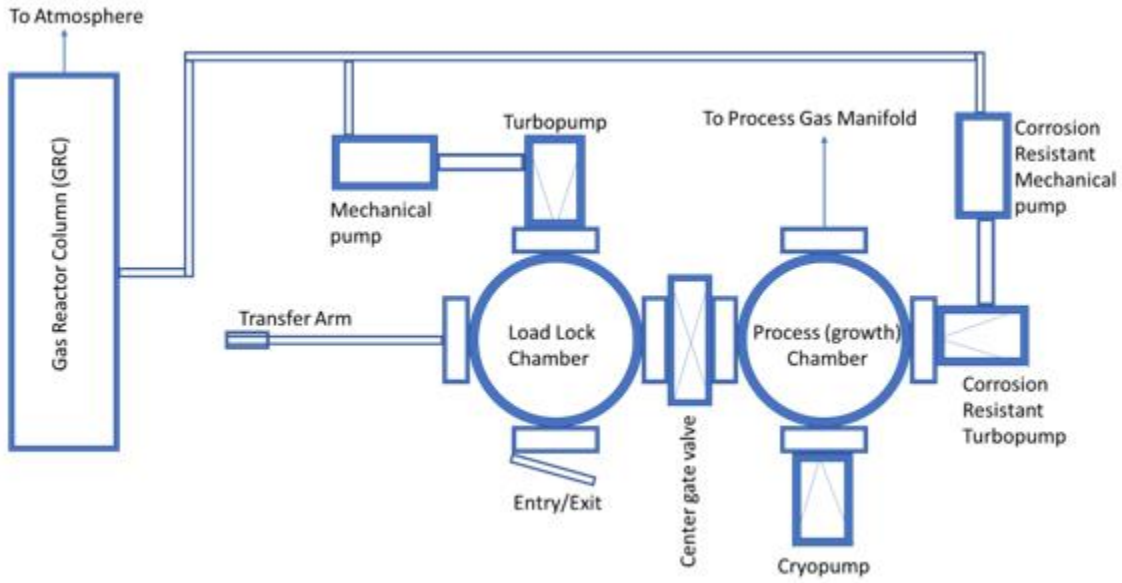

Figure 2.1. Pictorial representation of the UHV-CVD system [61]

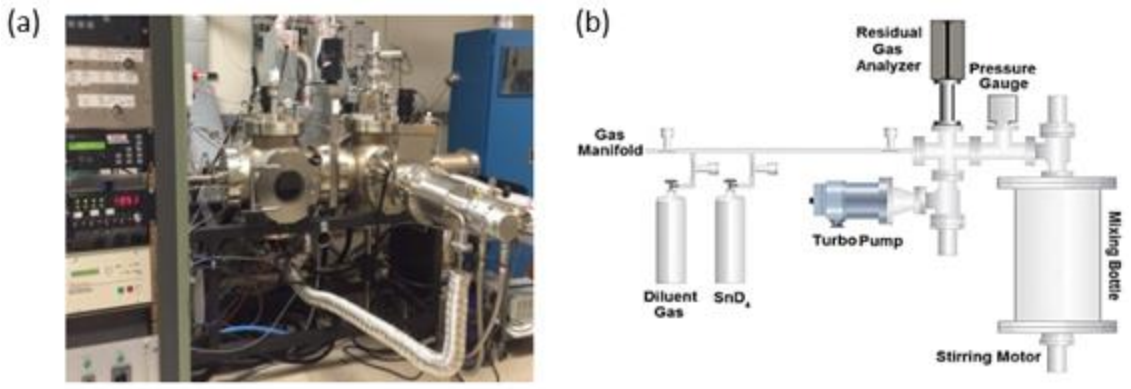

Figure 2.2. (a) Pictorial representation of the UHV-CVD system [61], (b) Gas delivery and mixing schematics.

2.3 Reduced-pressure chemical vapor deposition (RP-CVD) system

Healthy and productive collaboration between academia and industry is essential for the fast-paced development and adoption of potentially disruptive technologies. In this vein, our research group has joined effort with an industry leader in CVD growths to bring to fruition GeSn-based optoelectronics and photonics systems. Part of this efforts is our collaboration with ASM America Inc., Phoenix, AZ to deliver GeSn and SiGeSn bulk and QW growths.

Figure 2.3 shows the image of a single-wafer RP-CVD system. GeSn/Ge/Si Bulk and SiGeSn/GeSn QW structures grown using this system are accomplished using ASM's Epsilon® 2000 Plus reactor system. Like the UHV-CVD system, the Epsilon-model RP-CVD has unique components that makes it suitable for thin film heterostructure growths. The system is a load-locked reactor system that allows for the horizontal flow of precursor gases in a cold-walled quartz chamber that consists of a lamp-heated silicon carbide (SiC) graphite susceptor [62]. The next section discusses all characterization techniques used in this work.

Figure 2.3. ASM's Epsilon® 2000 Plus reduced-pressure CVD assembly.

2.4 Thin Film Characterization

2.4.1 Ellipsometry

The ellipsometry characterization technique employs the use of an ellipsometer to measure nano-scale thicknesses of a grown thin film sample. As a first procedure in the entire growth process, GeSn materials grown in either UHVCVD or RP-CVD machine are passed on to the ellipsometry machine for a quantitative measure of the sample's thickness and or the Sn composition. The technique bases off a simple principle where light impinged on a film experiences a change in polarization usually in the form of intensity and phase. This implies that two light waves in phase will experience a change of polarization when they impinge a thin film material. This polarization change is typically expressed in circularly (circular polarization) or elliptically (elliptical polarization) forms. The ellipsometry process occurs in two disparate yet connected stages. The first is the polarized light emission stage involving the polarizer and light source of a particular polarization while the second stage handles detection events through an

analyzer and a detector. Imaginatively, this can be thought as having a sample (film) in the middle of a light source and a detector, such that light incident on a sample is reflected and undergoes a polarization change as result of its interaction with the sample. The analyzer on the other side of divide is set to a continuous rotational motion that allows for light of different polarizations to be sensed and processed by the detector. The measured polarization changes are recorded as angular measurements of Ψ (Psi) and Δ (Delta). Values of these angular measurements are then modeled using a combination of material model parameters and regression analysis. Models are easily built for standard materials with parameters in the ellipsometer's database while materials like GeSn that are yet to have their database updated/stored would usually require the development of a new model. Estimated GeSn models used in this research uses Ge as the base material. To create an acceptable model, measured GeSn ellipsometry data are deftly fitted by moving/reducing the bandgap to lower energy until an approximate model is realized. Although errors due to the inaccurate optical constants are introduced in the process, but are ignored since they are idealized to be very small. For this work, a variable-angle ellipsometry system (J.A. Wollam's WVASE32 model) was used to carry out needed measurements.

2.4.2 Raman Spectroscopy

Analyzed Raman scattered lights provide information about the composition, crystallinity and strain of a thin film material. This method explores the low energy interactions that occur when light is inelastically scattered off atoms and molecules in a thin film material. Low energy interactions manifest in rotational and vibrational modes, and since vibrational energies are uniquely tied to the chemical bonding state of a material, they can be used to identify materials. In this method, monochrome lights incident on a material are scattered off as splits of elastic and

inelastic scattered photons which are then later collected. While the inelastically scattered light responsible for providing information about the low interaction energy interactions (Raman scattered lights) are preserved, the elastically scattered lights (Rayleigh scattered lights) are eliminated using a special type of notch filter. Collected scattered photons often experience a shift as a result of the vibrational and rotational energies created through their interactions. This photon energy shifts are known as Stokes or anti-Stokes shifting. Figure 2.5 below shows the schematics of our in-house Raman system. This system consists of an assemblage of lens, grating-based spectrometer, a Liquid Nitrogen (LN_2) charged coupled device (CCD) camera that can also be replaced by photomultiplier tube (PMT) detector in the event of a vacuum degradation. Additionally, the system uses a 532 nm and a 632 nm laser source to illuminate target samples. Typical shifts observed for Si, Ge and α-Sn are 520 cm^{-1}, 300 cm^{-1} and 210 cm^{-1} respectively. Implying the characteristic shift observed for GeSn materials should be between 210 cm^{-1} and 300 cm^{-1}.

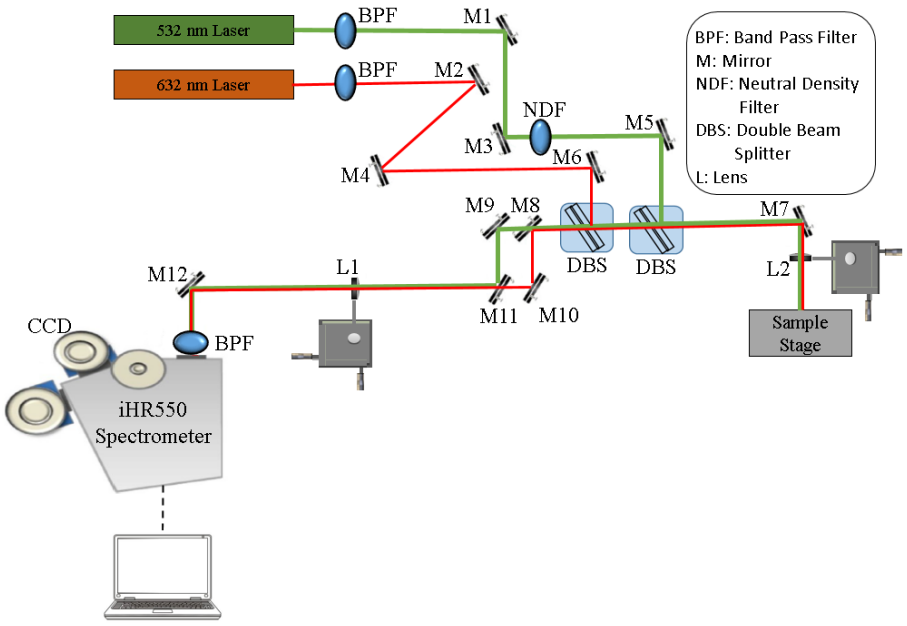

Figure 2.4. Schematics of in-house built Raman system.

2.4.3 Photoluminescence

This method typically investigates the bandgap character of semiconductor thin film materials. As an optical characterization of note, photoluminescence (PL) involves the process of light emission from a target sample after it has undergone photon absorption. Following the interaction of photons with electrons in the probed materials, electrons are excited to higher energy level, thereby creating an electron-hole pair that radiatively recombine to reproduce a photon energy that equates the probed sample's bandgap. In addition to providing the bandgap information, optical properties such as the recombination processes, carrier lifetimes and a myriad of semiconductor material properties can be measured as well.

All PL measurements obtained in this dissertation were carried out using an in-house PL multifunctional set up that integrates six (6) different excitation pumping lasers namely: i) the 532 nm continuous wavelength (CW) laser, ii) 1064 nm pulsed laser, iii) 1550 nm CW laser, iv) 2000 nm CW lase v) 780 nm Ti-sapphire femtosecond laser (pulsed) and the vi) Nd: YAG laser. The setup also consists of the Horiba grating-based spectrometer (iHR320) that is easily attached to three (3) detectors of different wavelength capabilities – PbS (3 μm cut-off), InSb (> 3 μm cut-off) and InGaAs (2.3 μm cut-off) detectors. Although the system is primarily used for off-axis PL collections at room and low temperatures, other adjoining sub-systems such as the micro-PL and the optical pumping set ups are also used per need basis. As far as this work is work in concerned, only the 532 nm, 1064 nm and the 1550 nm laser were used. A generalized depiction of the PL set up shown in Figure 2.5 below.

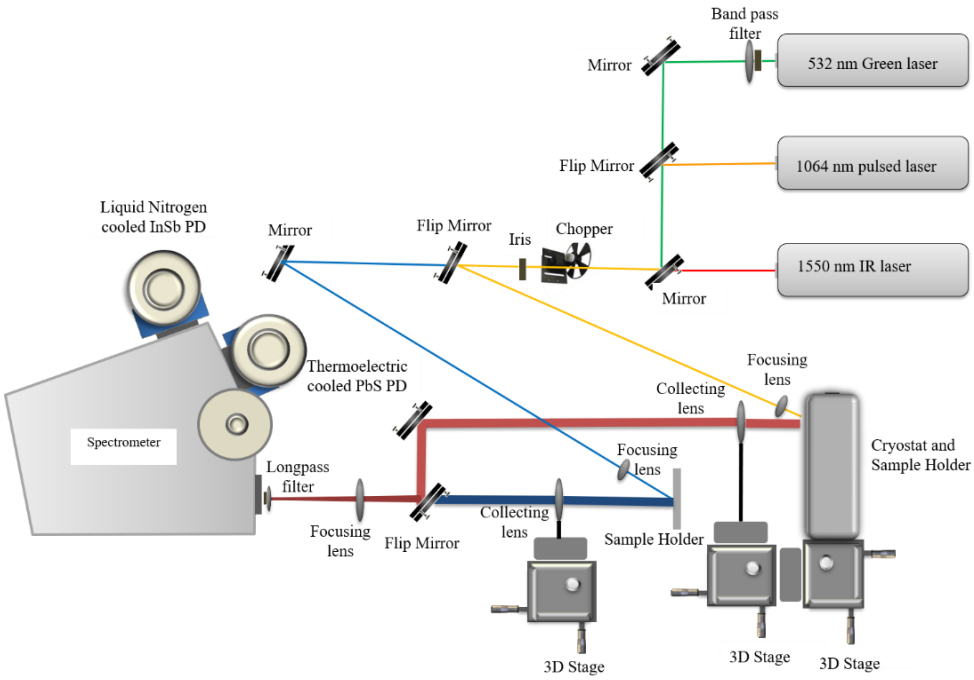

Figure 2.5. A generalized depiction of the PL set up consisting of different excitation pumping sources.

2.4.4 X-ray diffraction

X-ray diffraction (XRD) is regarded as a non-invasive characterization technique that measures the lattice constant, composition, strain and the overall material quality of a semiconductor film. Early in 1913, William Henry Bragg described the internal architecture of a material by exploiting its most important structural character - the spacing between the atomic arrangements [63]. The XRD technique works by applying high voltages to two electrodes. This prompts a sea of electrons to accelerate from an x-ray source towards a sample target and also opens up the possibility of two reactional pathways before x-rays are generated. These are: i) the possibility electrons being decelerated by the atoms in sample (bremsstrahlung radiation) and, ii) the likely excitation of the atoms in the sample due to collisional interactions between the 'sea' of electrons and the atoms in the sample (collision radiation). The combination of these two occurrences are responsible for the generation of x-rays. Using Bragg's relation, it is possible to

determine the distance between the atomic planes of a crystal structure. Consider a beam of x-ray incident on an atomic crystal of lattice spacing, d, the Bragg's condition relates its wavelength, λ, to the angle of diffraction θ through the equation below:

$$n\lambda = 2d\sin\theta \qquad \text{(Equation 2.1)}$$

where *n* also represents the order of diffraction. Two interaction pathways depicting symmetrical and asymmetrical measurement geometries are shown in Figure 2.6 below. In the former case (Figure 2.6 (a)), the incident angle (ω_i) is kept constant while the 2θ angle varies across the planes. It is also noteworthy to mention that the incident angle (ω_i) equals the diffraction angle (ω_d) in this case which is also referred to as the rocking curve method. As for the latter case (asymmetrical), all the three parameters are varied accordingly, i.e., 2θ, ω_i and ω_d. This is realization is aptly depicted in Figure 2.6 (b). The asymmetrical measurement approach results in the two-dimensional XRD scan of a semiconductor film structure and refers to a process called the reciprocal space mapping (RSM). Compared to XRD rocking curve scans (along the 004 direction), reciprocal space maps the information extracted from reciprocal space maps are much more detailed. This is due the possibility of decoupling of the lateral correlation and the mosaic spread direction, which is usually along the $\bar{2}\bar{2}4$ direction[64].

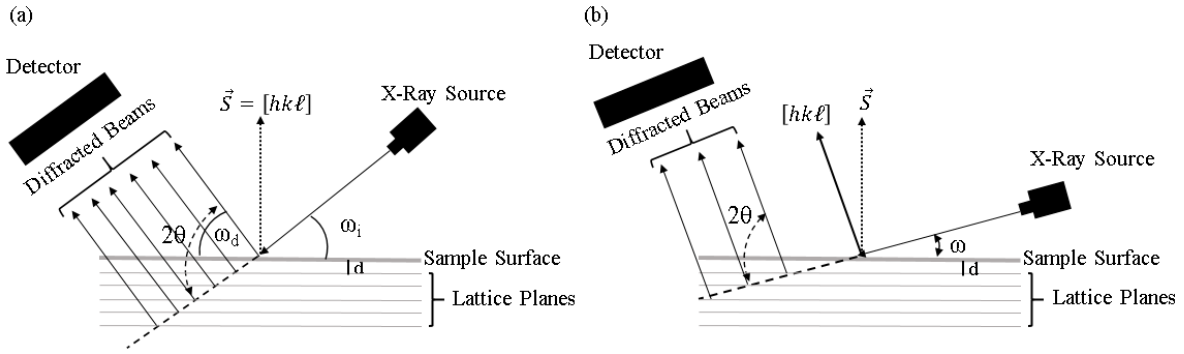

Figure 2.6. Schematics of two X-ray diffraction approach (a) symmetrical geometry (b) asymmetrical geometry.

In addition to the wealth of details that can be obtained using the asymmetric measurement approach, specific information about the misfit and threading dislocation densities can also be extracted when integrated with existing modelling functions. As already established, epitaxial GeSn growths are sustained by compressive strain that originates from the 15% lattice mismatch between Germanium (Ge) and alpha-Tin (α-Sn). The relief of this compressive strain is hinged on a specific critical thickness that causes strain relaxation. This strain relaxation event is perhaps accompanied by the generation of threading and misfit dislocation (TDs and MDs) that provoke displacement fields that alter the distribution of scattered x-ray intensity. Note that scattering events from a strain-relaxed are different from that of a non-defective ideal crystal[65]. The theoretical framework for estimating the x-ray scattering intensity of a significantly defective crystal is based on the generalized kinematic theory for scattered x-rays. The theory heavily leans on considerations for misfit dislocations, and as such, contributions from threading defects were intentional omitted in the calculations[66]. Therefore, the intensity of scattered x-rays emanating from a densely-defected epilayer-substrate interface is given as follows [67],

$$I\left(q_x, q_z\right) = \pi \int_0^h \frac{dz}{\sqrt{\det \hat{w}}} \exp\left(-\frac{1}{4} w_{ij}^{-1} (q - q_0)_i (q - q_0)_j \right) \qquad \text{(Equation 2.2)}$$

here, $q = Q - Q_0$ represents the difference between the scattering vector, Q, and the reciprocal lattice vector, Q_0, h is the thickness of the epilayer while $\hat{w}$ is a symmetric matrix consisting of w_{ij} number of elements with $i, j = x, z$. The diffraction peak shifts due to the presence of the MDs are q_{0x} and q_{0z} respectively. These are expressed below as,

$$q_{0x} = \rho Q_x b_x \qquad \text{(Equation 2.3)}$$

$$q_{0z} = -\frac{2\nu}{1-\nu} \rho Q_z b_x + q_z^c \qquad \text{(Equation 2.4)}$$

here, ρ is the defect density of the MDs, ν is the Poisson ratio, b_x is the burger vector along the x-axis, $q_z^c = \frac{1+\nu}{1-\nu} Q_{0z} f(z)$ is the diffraction peak shift due to the composition of the alloy, where $f(z)$ represents the lattice mismatch parameter. The reciprocal space elements, w_{ij}, is responsible for defining geometry of the diffuse scattering are expressed below according to Kaganer et al. [67]

$$w_{xx}(z) = \frac{\rho}{2} \sum_{\sigma=x,z} \int_{-\infty}^{\infty} dx \left(Q_x^2 u_{x,x}^{(\sigma)2} + Q_z^2 u_{z,x}^{(\sigma)2} \right) \quad \text{(Equation 2.5)}$$

$$w_{xz}(z) = \frac{\rho}{2} Q_x Q_z \sum_{\sigma=x,z} \int_{-\infty}^{\infty} dx \left(u_{x,x}^{(\sigma)} u_{z,z}^{(\sigma)} + u_{x,z}^{(\sigma)} u_{z,x}^{(\sigma)} \right) \quad \text{(Equation 2.6)}$$

$$w_{zz}(z) = \frac{\rho}{2} \sum_{\sigma=x,z} \int_{-\infty}^{\infty} dx \left(Q_x^2 u_{x,z}^{(\sigma)2} + 2Q_z^2 u_{z,z}^{(\sigma)2} + Q_x^2 u_{x,z}^{(\sigma)2} \right) \quad \text{(Equation 2.7)}$$

here, the displacements, $u_{ij} = \partial u_i / \partial x_j$ are due to the presence of MDs as expressed in Appendix B of Kaganer et. al. [67]. The theoretical narrative for x-rays scattering in a multilayered and heterogeneous systems are not exactly similar as expressed in reference [68]. Of course, in this case, MDs are present along all the interfaces based on the number of layers. Correspondingly, MDs inputs from all the layers are factored into the expressions of q and w that introduces a new function, H, known as the Heaviside function. The expressions are as follows:

$$q_{0x}(z) = Q_x b_x \sum_k \rho_k H(d_k - z) \quad \text{(Equation 2.8)}$$

$$q_{0z}(z) = -\frac{2\nu}{1-\nu} Q_z b_x \sum_k \rho_k H(d_k - z) + q_{kc}^c \quad \text{(Equation 2.9)}$$

$$w_{ij}(z) = \sum_k \left[w_{ij}^k(z) H(d_j - z) + \tilde{w}_{ij}^k(z) H(z - d_k) \right] \quad \text{(Equation 2.10)}$$

In the above expressions, parameter k is the number of identified interfaces, ρ_k is the MDs density at the kth interface and d_k is the kth layer thickness. The layers above and below the kth interface are represented by the parameters $w_{ij}^{k}(z)$ and $\tilde{w}_{ij}^{k}(z)$.

The samples used in this dissertation were characterized using a Phillips (Malvern, UK www.malvernpanalytical.com) X'pert Pro x-ray diffractometer (XRD). The crystalline material, as well as the in-plane (a) and out-of-plane (a) lattice constants, were obtained by measuring the symmetric (004) rocking curves and asymmetric $\bar{2}\bar{2}4$ reciprocal space mapping (RSM).

2.4.5 Transmission Electron Microscopy (TEM)

This technique was developed to generate semiconductor images using the physics of electrons diffraction. The process entails the interaction of high beam electrons (>200 keV) with a thin semiconductor surface (<100 nm) thereby resulting in a resolved image of its target layers. Fundamentally, the transmission electron microscopes function the same way as conventional optical microscopes, the difference seems to be the difference in the system sizes, the probe source (light vs electron) and type of lens (quartz vs electromagnetic) required for the source probe to traverse. While the optical microscope can be utilized in ambient settings, the TEM only finds use in ultrahigh vacuum (UHV) environments. Before subjecting a thin film material to high electron beam bombardment, the film is made to undergo a sample preparation process that involves sample dicing and gluing procedure, where two 2.5 x 5 square-inch samples are cleaved apart and glued together. The glued material is then passed through a mechanical thinning system to be thoroughly polished to an approximate thickness of nearly 30-micron. Polished specimens are ion-milled until a hole is drilled in the middle with the resulting product sent

through the TEM assembly for imaging. The TEM used in this work is the standardized FEI Titan TEM assembly located in the Institute of Nanoscience and Engineering building at the University of Arkansas, Fayetteville.

2.4.6 Atomic Force Microscopy (AFM)

Since the mid-1980s, the introduction of suitable instrumentation for various types of scanning probe microscopy ushered in an entire new era of understanding in the area of material surface technology[69,70]. Of particular interest is the development of the Atomic Force Microscopy (AFM) technique by Binning et al., in 1987 [71]. This technique routinely examines the topography of surfaces down to the nanoscale level. This is based on the force interaction between the surface of the sample and a cantilever-supported probing tip. During measurement, the cantilever bends following the interaction between the tip and the sample surface. This interaction is then sensed by a photodetector and a laser diode. The schematic representation of the major parts of the AFM assembly is presented below in Figure 2.7.

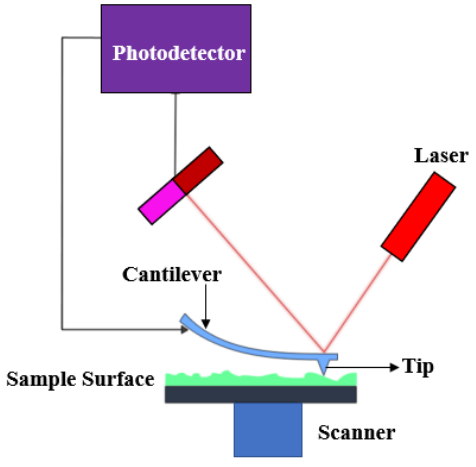

Figure 2.7 Schematic representation of the AFM setup. Modified after Rajagopal [72]

This research utilized a standard Nanoscope IIIa scanning probe microscope (Dimension 3000) engaged in tapping mode status to conduct AFM measurements. To estimate the surface roughness of a semiconductor film, a silicon cantilever tip of nearly 10 nm in diameter is positioned to make contact with the film surface by taking an average of 512 measurements (in one direction) over a 10 μm x 10 μm unit area of a probe point.

Chapter 3: Investigation of SiGeSn/GeSn Single Quantum Well with Enhanced Well Emission

3.1 Introduction

SiGeSn/GeSn material systems have increasingly gained traction in the optoelectronics space in recent times. While these binary and ternary group IV alloy variants have characteristically featured compatibility to standardized Si complementary metal oxide semiconductor processes [49,73,74], they also possess the ease of tunability from indirect to direct bandgap transition [75–77], in addition to covering an extensive broad wavelength through the near- to midinfrared. These unique possibilities have continued to inspire the development of SiGeSn-based nanophotonics and optoelectronics devices such as emitters [56,78,79], lasers [11,20,80,81], modulators and photodetectors [82] to mention a few [83,84].

The practical realization of a true direct bandgap GeSn has been made possible leading to variegated novelties in GeSn-based double heterostructure and QW LEDs as well as the first-demonstrated optically-pumped GeSn lasers[9,85]. Advances in laser development has also featured considerable performance improvements. These include: i) the achievement of continuous wavelength at low temperature up to 70 K [19]; ii) 2-3 μm lasing spectrum coverage with tunable emission wavelength[20] iii) the operational lasing temperature near room temperature (RT) under pulse pumping conditions [21,22], and more recently; iv) the discovery and demonstration of the first electrically injected edge emitting laser operating at lasing temperature of up to 100 K [23]. While these breakthroughs are established via GeSn bulk structures, QW structures are desired for improved performance with promise to manifest low threshold and high carrier confinement lasers and LEDs [59,86–92]. The initial realization of this pursuit led to the investigation of Ge/GeSn/Ge QW structures. However, detailed analysis

revealed that using Ge as a barrier in GeSn QW result in a type-II band alignment whilst featuring a direct bandgap well character that owes to increased compressive strain in the QW layer [59,86,87]. To circumvent these limitations, SiGeSn barrier layers were suggested as alternative material to ease the compressive strain leading to bandgap directness and improved confinement within the well [89,92]. This is achieved by appropriately tuning the bandgap and lattice constant through the incorporation of desired Si an Sn amounts into the Ge matrix. The growth of high-quality ternary SiGeSn alloy layers has been demonstrated using low-temperature growth strategy[93,94]. Recently, our previous study has investigated the PL characteristic and associated optical transitions in a relatively thin well (9-nm) GeSn/SiGeSn/GeSn structure although type-I band alignment and direct bandgap QW was obtained, the carrier confinement was still low. Accordingly, an optimized QW structure with a relatively thicker QW well layer is suggested for much-improved carrier confinement.

To improve the carrier confinement in direct type-I bandgap SiGeSn/GeSn QW structures further increasing the thickness of the GeSn active layer region upended to enhance light absorption while also lowering the first energy level in the T-valley is a feasible solution towards an optimized direct bandgap semiconductor. In this work, temperature and power dependent PL measurements of a thicker SiGeSn/GeSn QW were obtained, analyzed and compared with a sample (22-nm) with similar QW structural configuration but relatively thinner active region (9-nm). For in-depth analysis, two continuous wavelength (CW) pumping lasers (532-nm vs. 1550-nm) with different penetration depths were utilized to further investigate the emission and optical characteristics of the thicker well sample. Temperature dependent PL spectra obtained under 532-nm pumping laser for the thicker well sample show a significantly improved carrier confinement as evidenced by the stronger integrated intensity compared to sample B. This

thicker well optimized QW design is further validated by the pumping power-dependent PL spectra which exhibits stronger (more than 2-times) peak intensities under each pumping laser. As a result, significantly enhanced emission from the quantum well was observed. The strong photoluminescence signal allows for the estimation of quantum efficiency (QE), which was unattainable in previous studies. Based on pumping-power-dependent photoluminescence spectra at 20 K, the peak spontaneous quantum efficiency (SQE) and external quantum efficiency (EQE) were measured as 37.9% and 1.45%, respectively.

3.2 Experimental Approach

3.2.1 Material Growth and Characterization

A SiGeSn/GeSn QW structure (Sample A) was epitaxially deposited on a Ge-GeSn buffered Si substrate using a conventional industry-standard ASM Epsilon 2000-Plus reduced pressure chemical vapor deposition (RPCVD) growth machine. Similar to our previous works[95], Silane (SiH_4), Germane (GeH_4) and Tin Tetrachloride ($SnCl_4$) reactor gases were utilized as dominant precursors of Si, Ge and Sn respectively. The layer-by-layer structural configuration features a nominal 700-nm grown Ge buffer, a 600-nm thick $Ge_{0.915}Sn_{0.085}$ buffer and a $Ge_{0.915}Sn_{0.085}$ well region bounded on opposite sides by a 70-nm thick $Si_{0.047}Ge_{0.890}Sn_{0.063}$ bottom barrier and a 64-nm-thick $Si_{0.050}Ge_{0.886}Sn_{0.064}$ top barrier (See Figure 3.1 for sample's structural profile). An in-depth explanation of our growth approach is presented in selected publications.[24,95] Following the growth procedure, the samples were subjected to an array of characterization techniques such as the cross-sectional transmission electron microscopy, high-resolution X-ray diffraction and Secondary Ion Spectrometry (SIMS) to inspect and analyze the film thicknesses and the silicon (Si) and tin (Sn) percentage compositions. XRD reciprocal space

maps (RSM) was also used to measure the strain within each layer. Figure 3.1 (b) & (c) shows the TEM cross-sectional profile of our study (shown for Sample A alone).

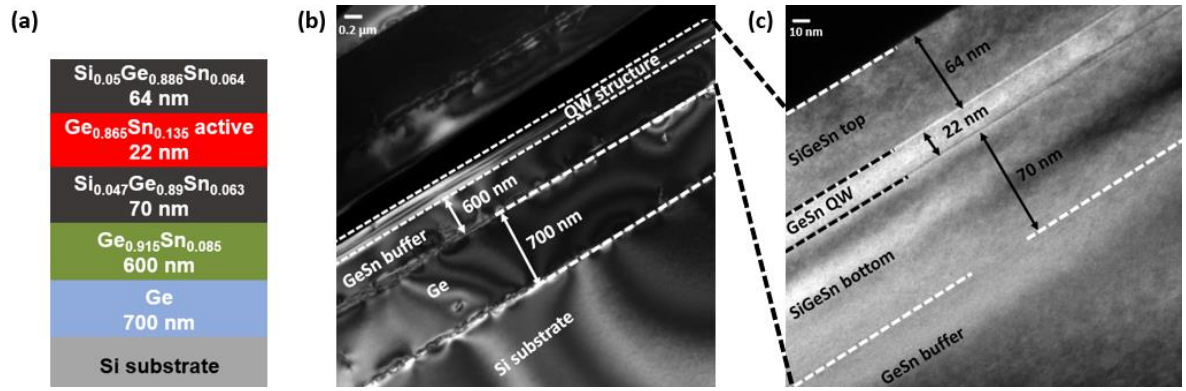

Figure 3.1. Cross-sectional representation of the QW sample (not drawn to scale) (b) TEM image of the sample showing the entire structure (c) Embossed TEM image of the QW active region.

Respective film layers are clearly resolved featuring low defect populations that owes to an optimized Ge-buffer growth that localizes defects within the Ge-Si interface while preventing possible threading dislocations from propagating through the QW active regions.

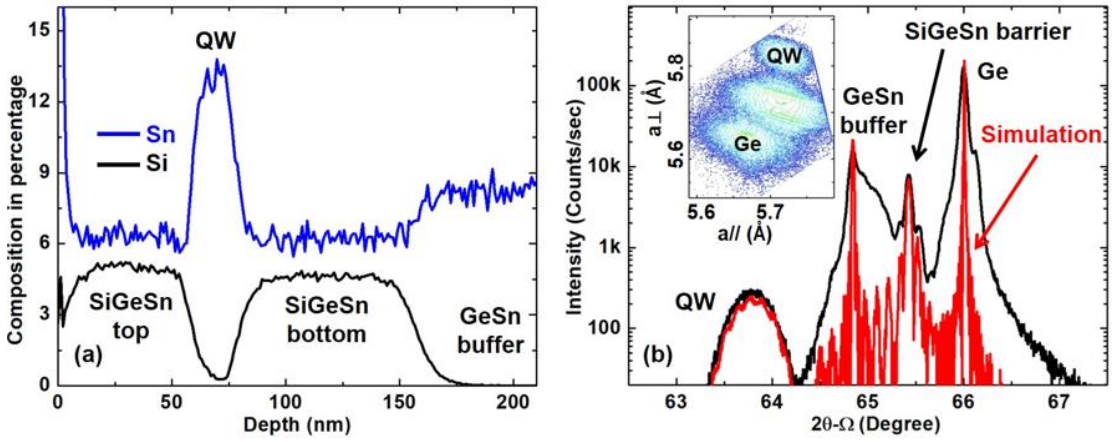

Figure 3.2. (a) SIMS profile of the QW sample showing respective Si and Sn compositions. Respective layered-film thicknesses can also be inferred from this plot. (b) High-resolution X-ray diffraction (HRXRD) 2θ-Ω scan showing clearly-resolved peaks corresponding to each layer. Black and red curves represent the experimental and simulated results. The inset figure shows the RSM contour plot.

Figure 3.2 (a) shows the SIMS profile of the QW sample showing the percentage compositions of the Si and Sn within each layer. As seen in the figure, each distinct discontinuity corresponds to respective layers starting with SiGeSn top barrier from the left to the GeSn QW, the SiGeSn bottom barrier and to the far right GeSn buffer. In the same order, the respective Sn percentage compositions are 6.4%, 13.5%, 6.5% and 8.5%, while the Si compositions in SiGeSn bottom and top barriers are 4.7% and 5.0%.

Due to the comparative objective of this study, a relatively thinner well sample (denoted as sample B) grown using similar growth strategy is used as reference sample. Sample B is characterized by a thinner 9-nm GeSn well and bounded by a 54-nm-thick $Si_{0.042}Ge_{0.892}Sn_{0.066}$ top barrier and a 54-nm-thick $Si_{0.036}Ge_{0.897}Sn_{0.067}$ bottom barrier. Sample B is presented to systematically analyze and compare the QW optical property of our study sample (Sample A). Thicknesses of the GeSn wells (for Samples A & B) can be obtained from through a Gaussian fit from the full width at half maximum (FWHM) of the assigned SIMS peak. This is then compared and verified with the extracted results of the TEM profile. The extracted value of thickness for sample A is 22-nm while that of Sample B is 9-nm – About twice the thickness of Sample B. Figure 3.2 (a) shows the HRXRD 2θ-ω scans of the study sample (Sample A) with black and red lines depicting both experimental and simulated results. The curves show distinct and well-resolved peaks assigned to the Ge buffer, GeSn buffer, SiGeSn barrier and the GeSn QW. The peaks corresponding to the elemental and alloy presence are 66.1°, 64.8°, 65.4° and 63.8° respectively. The 2θ-ω angular assignment of the GeSn well, GeSn buffer and SiGeSn barrier is due to the incorporation of Sn (Si) to Ge which shifts both peaks to lower (higher) angles. As mentioned above, the extracted thicknesses of the respective layers from the simulated data are matched with both the SIMS profile and TEM results to ensure accuracy.

Notice two subtly-pronounce peaks (around 65.4°) on opposite sides on the identified SiGeSn barrier peaks. These are called Pendellösung fringes [96] as they are often an indication of material growth quality especially with regards to the uniformity of the alloy compositions and smoothness of the interface. To quantify the structural parameters, theoretical derivations of Vegard's law was employed to infer the lattice constant of the respective layers [97–99]. To infer the complete strain information for these sample, an X-ray diffraction RSM measurement was carried out to extract the appropriate values within each layer. The results identifies both Ge and GeSn buffer layers to be almost fully relaxed with tensile (Ge) and compressive (GeSn) residual strains of 0.2%. On the other hand, the SiGeSn layers (barriers) and GeSn wells are subjected to compressive and tensile strain of 0.25% and 0.98% respectively. This is due to the fact that these epilayers are grown pseudomorphically to the GeSn buffer layer. In addition to the revelations on the material's structure, an observed SiGeSn contour broadening is noticed on the RSM plot. This hypothesized to be due to the slight disparity in Si and Sn compositions reported for the bottom and top barriers.

Table 3.1 Structural information of the QW study samples

Sample	Layer	Thickness (nm)	Si (%)	Sn (%)	Strain (%)
A	Ge Buffer	700	0	0	0.20
	GeSn Buffer	600	0	8.6	-0.20
	SiGeSn Bottom Barrier	78	4.2	6.6	0.28
	GeSn Quantum Well	9	0	13	-0.92
	SiGeSn Top Barrier	54	3.6	6.7	0.28
B (Ref.)	Ge Buffer	700	0	0	0.20
	GeSn Buffer	600	0	8.5	-0.20
	SiGeSn Bottom Barrier	70	4.7	6.3	0.25
	GeSn Quantum Well	22	0	13.5	-0.98
	SiGeSn Top Barrier	64	5.0	6.4	0.25

* Negative value indicates the compress strain.

A summary of the material characterization extracts for samples A and B (reference sample) are reported in Table 3.1 below.

Notice that besides the similarities in the thicknesses and Si and Sn compositions in the barrier and buffer layers, sample A differs significantly from sample B in its GeSn well thickness value (22-nm vs, 9-nm)

3.2.2 Photoluminescence Studies

Figure 3.3 (a) shows the normalized and stacked PL temperature measurement of sample A using a continuous-wave (CW) 532-nm pumping laser.

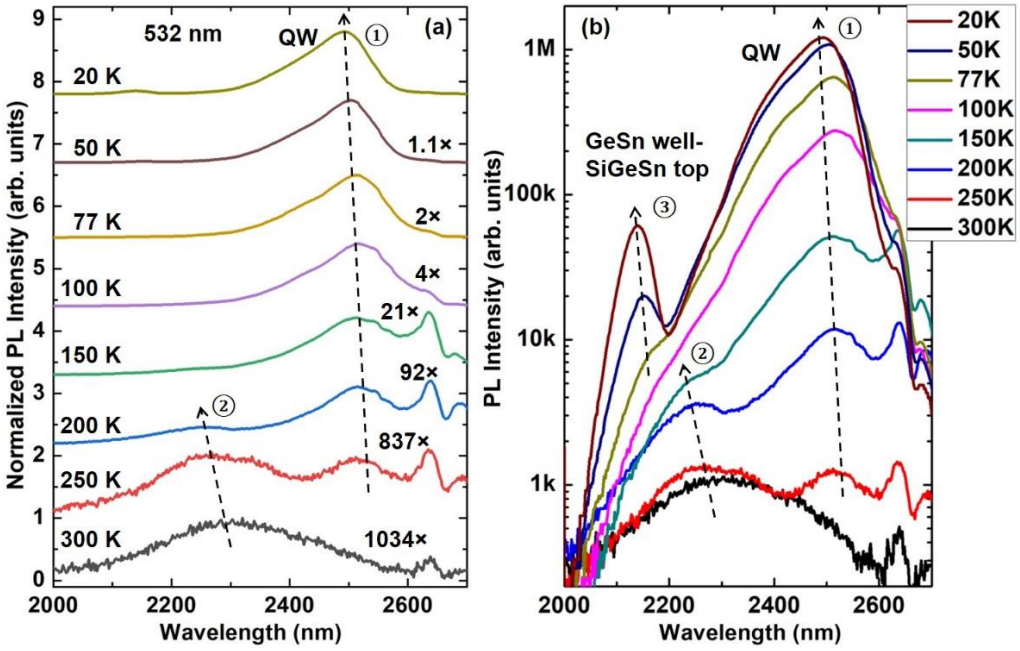

Figure 3.3. (a) Normalized temperature-dependent PL of sample A under 532 nm pumping laser (linear) (b) log-scale version of same. Dashed arrow indicates the shift in peaks as the temperature decreases from 300K to 20K.

The plot is presented in stacked and normalized format for easier identification of possible transition while comparing the evolution such transitions at different temperatures.

For instance, at room temperature (300 K), the PL spectra is observed to show a broadened peak from 2100 to 2500 nm, as defined and labeled by peak ②. Based on ellipsometry data, it is noteworthy to mention that the estimated penetration depth of the 532 nm laser through the SiGeSn structural layer is approximately 21 nm. This implies that majority of the light absorption would occur at the SiGeSn top barrier. As a result, the identified broadened peak at 300 K is hypothesized to be due to possible multiple transitions involving the SiGeSn top barrier. These transitions consist of: i) emissions from the SiGeSn top barrier typed to transitions from L valley to the heavy hole (HH) and the light hole (LH) band, and ii) first energy levels within the Γ and L valleys to HH and LH bands in the SiGeSn barrier. Note that PL transitions from the LH band is found to be more predominant at 300 K. This is due to the fact that more holes are likely to populate the LH band faster since it is approximately 30 meV above the HH band within the SiGeSn barrier.

Following a decrease in temperature, two distinct PL spectra are observed at 250 K. The first (left spectra) identifies and retains the character of peak ② at 300 K but now less broad and shifted to shorter wavelength following an expected increase in bandgap energies. The second spectra (right spectra) emerge as a longer wavelength peak at 2530 nm and based on band diagram calculation, is assigned to emissions from the GeSn well. This peak is labeled as peak ①. Note that it is difficult to resolve emissions from the GeSn QW layer at 300 K. This is partly due to the limitation of the 532 nm laser in penetrating the GeSn QW layer which causes light absorption to be limited to the SiGeSn barrier while also resulting in weak absorption from the well. The second reason also owes to the weak carrier confinement resulting in the possible thermal excitation and recombination of carriers in the QW to the SiGeSn barrier. A further reduction in PL measurement temperature to 250 K results in an enhanced, higher intensity PL

expression in the GeSn QW (Peak ①). This is a testament to the increased carrier confinement within the well at lower temperatures. This low-temperature character is strengthened as temperature further reduced. For instance, the intensity of the QW peak at 20 K is about a thousand (1000) times greater than same peak at room temperature (300 K). Peak ② on the other hand shows non-obvious trend below 150 K. The intensity is almost dwarfed to the background due the dramatic increase in the intensity of the QW emissions as temperature further reduces.

For a detailed interpretation of the transition properties, the temperature-dependent PL of Figure 3.3 (a) is re-plotted as Figure 3.3 (b) in log-scale. Peak ① is seen to manifest an increase in intensity at considerably high temperature above 150 K. While this trend is somewhat limited to higher temperatures for peak ①, peak ② on the other hand presents a more global intensity improvement growing significantly as the temperature decreases. The growth of new set of peaks are noticed below 77 K and characterized to a well-resolved peak of about 2130 nm. These new peaks are labelled as peak ③ and are attributed to transitions between the QW Γ valley's first energy level and the LH band in the SiGeSn top barrier. The emergence of these peaks is due to the improved carrier confinement at lower temperatures. At these low temperatures, electrons are better confined within the Γ valley of QW layer while holes are also as much confined to the LH band of the SiGeSn top barrier layer due to a significantly high hole population. As a result, transitions of these types are further enhanced.

Figure 3.4 (c) shows the normalized and stacked PL temperature measurement of sample A using a continuous-wave (CW) 1550 nm pumping laser. Note that the PL spectra at 300 K shows similar character as that observed using the 532 nm pumping laser.

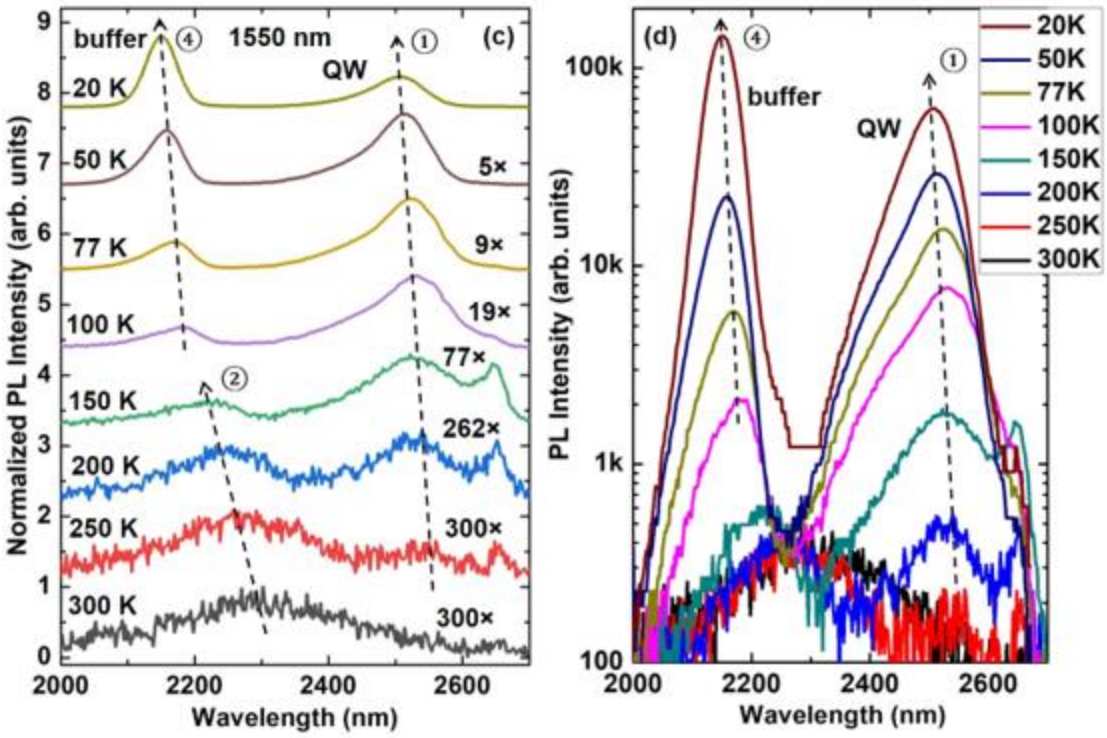

Figure 3.4. (a) Normalized temperature-dependent PL of sample A under 1550 nm pumping laser (linear) (b) log-scale version of same. Dashed arrow indicates the shift in peaks as the temperature decreases from 300K to 20K.

Since the 1550 nm laser operates at a relatively higher penetration depth, transitions assigned to the identified broad peak between 2100 nm and 2500 nm attributes to: i) possible emissions from both top and bottom SiGeSn barriers and ii) transitions between the QW conduction band (CB) and the valence band (VB) of the SiGeSn top and bottom barriers. These transitions are labelled as peak ②. At 250 K, we observe two PL spectra characterized by two noticeable peaks; the first peak (to the right) is noted as an extended evolution of the broadened peak identified as peak ② at 300 K, while the second (to the left) is a new and longer wavelength PL peak (peak ①) at nearly 2530 nm. This peak is assigned to emissions emanating from the GeSn well and further labeled as peak ①. This peak is characterized to a significant increase in intensity as the temperature decrease from 300 K to 20 K. On the other hand, it also

observed that both peaks ① and ② shift to lower/shorter wavelengths following temperature reduces from 300 K to 150 K. An additional peak is seen to emerge at 100 K. This peak differs significantly from peak 2 in that it is relatively stronger and is expressed as a shorter wavelength at ~ 2180 nm. Compared to peak 2, the intensity of this peak increases significantly as the temperature decreases while also growing at comparable rates as the QW peak (peak ①). This peak is assigned to as peak ④ and attributes based on band calculation to a direct bandgap emission from the GeSn buffer layer.

It is noteworthy to point out that the GeSn buffer emission observed in Figure 3.4 (a) is significantly stronger than the QW emission at 20 K. This is due to the possibility that carrier confinement is stronger at 20 K compared to emissions from the QW. The reverse is also holds true at higher temperatures, where relatively weak carrier confinements are observed in the GeSn buffer compared to stronger emissions in the QW layer. A trend is observed such that as the temperature decreases, the growth rate of the GeSn optical emission begins to rise to the point where it matches the QW emission and then later surpass it at 20 K. The comparatively high optical emission at 20 K could also be due to the thicker GeSn buffer (600-nm) which may favor the collective light absorption process.

For a clearer identification of the peaks, Figure 3.4 (b) is presented in log scale. Notice that the QW emissions increase significantly by approximately 300 times as the temperature decreases from 250 K to 20 K while emissions involving SiGeSn barriers grows slowly from 300 K to 150 K. The emergence of GeSn buffer emissions is also treated to a significant increase of about 100 times from 100 K to 20 K.

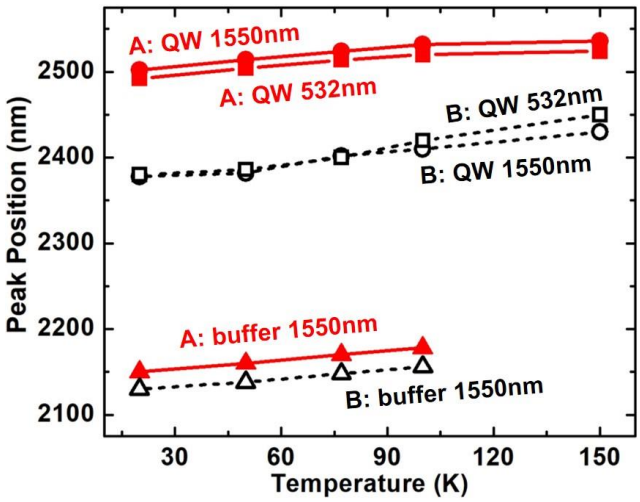

Figure 3.5. Peak wavelengths of samples A and B at each temperature for 532-nm and 1550-nm lasers

Figure 3.5 shows the peak wavelength positions of samples A and B extracted for each temperature using a Gaussian fitting procedure. Extracted peaks for both QW and buffer emissions show similar trends for both 532-nm and 1550-nm pumping lasers at each temperature of investigation. The diminutive difference in positions of the peaks for both lasers is possibly due to standard deviation errors. Note that the GeSn QW Sn composition of sample A is about 0.5 % higher than sample B, (Table 3.1 shows the detailed structural information) however, the QW emission wavelength is about 100-nm longer in sample A as shown in Fig. 3.4. This is attributed to the thickness of sample A which slightly doubles the thickness of sample B (22-nm vs. 9-nm).

The effect of which eases the compressive strain, and then extend the QW optical emission to about 2500-nm. The peak wavelengths of the GeSn buffer were also inspected since both samples have similar Sn compositions. As seen in the above plot, both samples show similar trend at each temperature for both 532-nm and 1550-nm lasers.

Figure 3.6 (a) shows the power-dependent PL measurement of sample A under 532-nm pumping laser at 20 K.

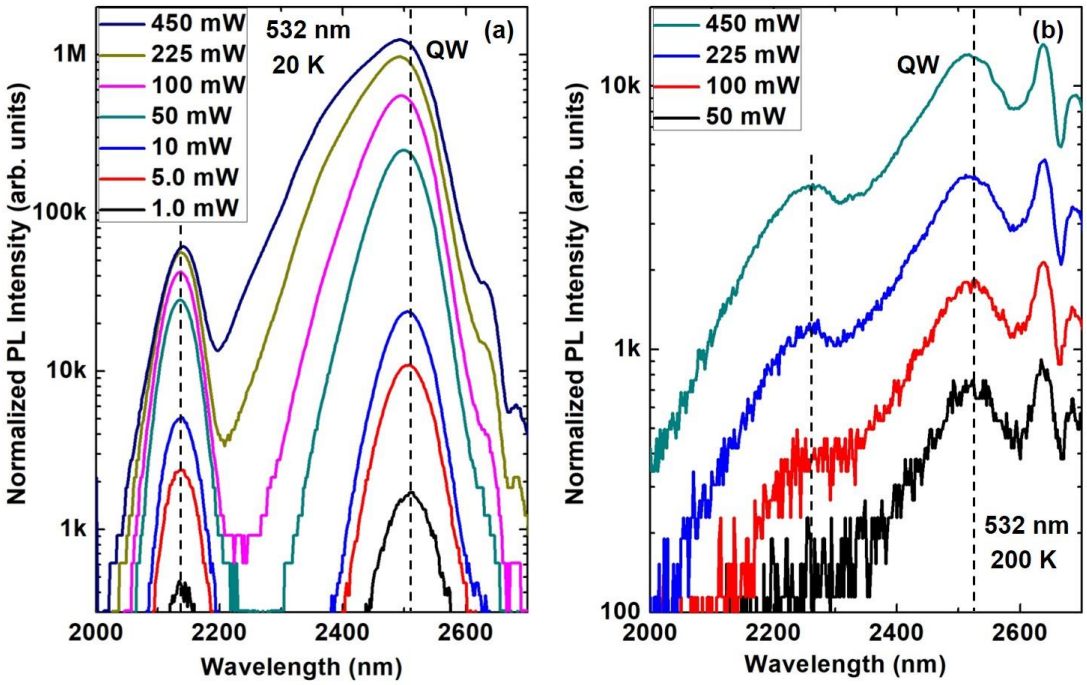

Figure 3.6. Power-dependent PL of sample A under 532-nm laser at (a) 20 K and (b) 200 K

The experiment was carried out using the same PL set-up configuration and measured at a constant temperature with the pumping power varied to further investigate the QW transition. As the pumping power increases, the longer wavelength peaks are blue-shifted which appearing as evidence for the band-filling effect [92] typically attributed to emissions originating from the QW. This shift is not observed for shorter wavelength peaks which based on observation, derives its origin from the conduction band (CB) in the GeSn QW and the light-hole (LH) band in the SiGeSn top barrier.

Figure 3.6 (b) shows the power-dependent PL measurement of sample A under 532-nm pumping laser at a 200 K where the emission from the QW is the more dominant PL. At this temperature, an increase in pumping power creates the possibility for electrons in the higher

energy levels in the GeSn QW to be thermally excited to the L valley in the SiGeSn barrier. As a result, majority of QW well emissions are attributed to transitions between the first energy level in the QW and the HH band which explains why there are no blue-peak shifts in the PL at shorter wavelengths. Furthermore, the broadened peaks in Figure 3.5(b) are associated with multiple optical transitions in the PL and feature as: i) transitions between the L valley and the HH bands which exists in the GeSn QW, and, ii) transitions between the GeSn QW conduction band and SiGeSn top barrier valence band as well as emissions from the SiGeSn top barriers which is associated with the shorter wavelength peaks. These transitions are difficult to identify due to the broad nature of the linewidth as well as the small energy separation.

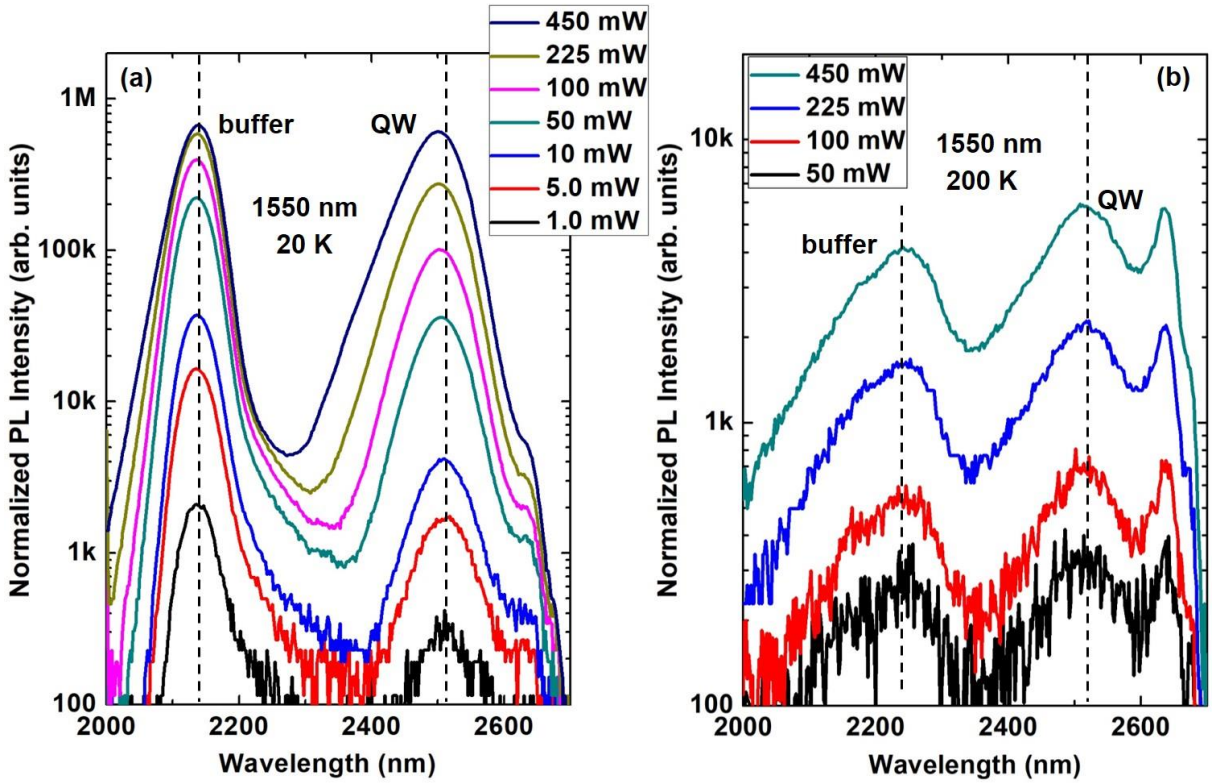

Figure 3.7. (a) Power-dependent PL of sample A under 532-nm laser at (a) 20 K and (b) 200 K

Figure 3.7 (a) shows the power-dependent PL measurement of sample A under 1550-nm pumping laser at 20 K. The QW peak shows pronounced spectral blue-shift upon pumping power increments which is characteristic of the earlier mentioned band-filling effect. As expected, the shorter wavelength peaks identified as, and originating from the GeSn buffer shows no distinct peak shift. Furthermore, it is observed that the peak assigned to the GeSn buffer is about 5 times higher than the emission from the QW peak. In fact, both peak intensities increase significantly upon pumping power increments with the QW emission showing a higher and more rapid growth rate comparatively. At the highest observable pumping power, in this case, at 450 mW, the peak intensities are seen to match equally. The intensity trends in the PL can be explained by the impact of the increased pumping power during measurement. This causes significant local heating effects that degrades carrier confinement in the GeSn buffer. As a consequence, carriers in the GeSn buffer are thermally excited to the conduction band of the SiGeSn bottom barrier which are eventually fed to the GeSn well, while leading to an enhanced QW emission.

Figure 3.7 (b) shows the power-dependent PL measurement of sample A under 1550-nm pumping laser at a 200 K. It is noteworthy to mention that the peak intensities of the shorter wavelength and QW peaks are comparable since all the layers are involved in the absorption and emission process. As a consequence of the degraded carrier confinement in GeSn buffer at high temperatures, the shorter wavelength peaks attributes to multiple optical transitions that originate from the GeSn buffer emissions as well as emissions from the SiGeSn barriers and transitions GeSn well CB and VB (LH) band in the SiGeSn top and bottom barriers.

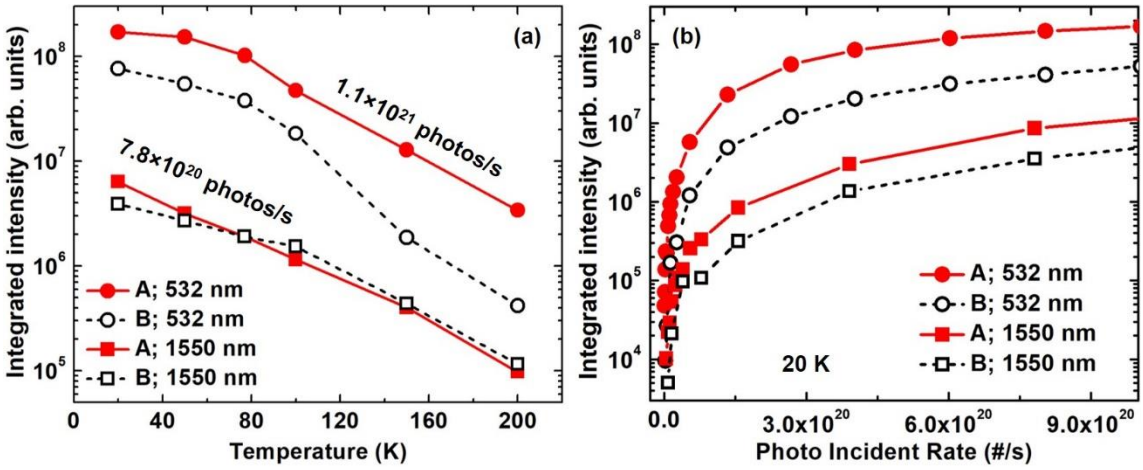

Figure 3.8. (a) Temperature-dependent integrated PL intensities (b) Integrated PL intensities with respect to a power-dependent photon incidence under 532-nm and 1550-nm pumping lasers. Sample B is presented here for comparison.

To further investigate the optical property of the QW, integrated intensities of the samples were extracted at each temperature under different pumping laser influence. As pointed out in the figure caption above, sample B is included to aid further analysis. Figure 3.8 (a) shows the dependence of the extracted integrated PL intensities on temperature. Starting with the 532-nm pumping laser, the integrated intensity for sample A (22-nm well) is approximately two times stronger than sample B (9-nm well). The reason for this comparatively high integrated intensity is due to: i) the ability of the thicker QW sample (sample A) to significantly enhance absorption; and ii) the influence of the increased well thickness in lowering the Γ valley's first energy level whilst improving the electron confinement in the GeSn QW. Under 1550-nm laser, Figure 3.8 (a) also shows similar trends as well as a slightly different integrated intensities for the two samples. Due to the penetration depth of 1550-nm laser, multiple transitions from overlying layers show up in the overall PL spectra, especially strong emissions from the GeSn buffer at lower temperatures, which can influence or dilute the QW emission.

Figure 3.8 (b) shows the integrated PL intensities at different photon incident rates (plotted in log-scale) at 20K. For both pumping lasers, the integrated PL intensity of the thicker well sample A is more than two times stronger than the reference sample B (Thinner QW sample). Integrated PL intensities are also seen to increase rapidly to gradually tend towards saturation as photon rate injection increases. Figure 3.9 below also compares the band structures of the SCH QW samples and reference B. As seen in sample A, the first energy level in the T valley is lower than for sample B. This is due to the induced compressive strain introduced by the increased well thickness.

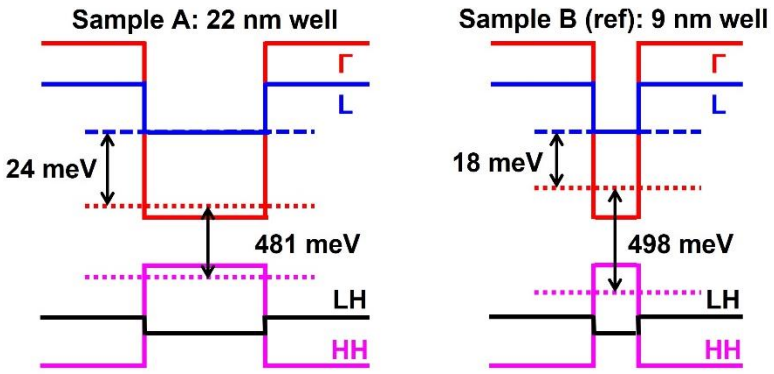

Figure 3.9. Energy band structure schematics of sample A (right) and B (left).

3.3 Quantum Efficiency Investigations

3.3.1 Introduction

A power-dependent PL measurement was carried out at 20K to study the spontaneous emission quantum efficiency (SQE) of the QW structure (Sample A) using methods discussed in [100–102]. External quantum efficiency (EQE) was estimated through an optimized off-axis experimental PL configuration that compares the measured signal from the QW sample to the collected signal from a Lambertian reflector. Analytical calculations of the photon extraction and

recycling radiative recombination parameters are based on an optical model that mimics absorption, transmission and reflection events under guided assumptions as idealized in Reference [101]. Absorption coefficient and index of refraction parameters are inferred from spectroscopic ellipsometry and transmission measurements, or obtained from literature [103].

3.4 Experimental Details

To measure the external quantum efficiency, we adopt a unique experimental setup [101] that compares the measured signal from the quantum well sample (Figure 3.10 (b)) to the collected signal from a Lambertian reflector (Figure 3.10 (a)). Since the Lambertian reflector is idealized to reflect the entire light signal, it directly accounts for possible losses and other measurement inaccuracies that otherwise may have been introduced had the quantum efficiency been estimated from the sample independently (Figure 3.10 (b)).

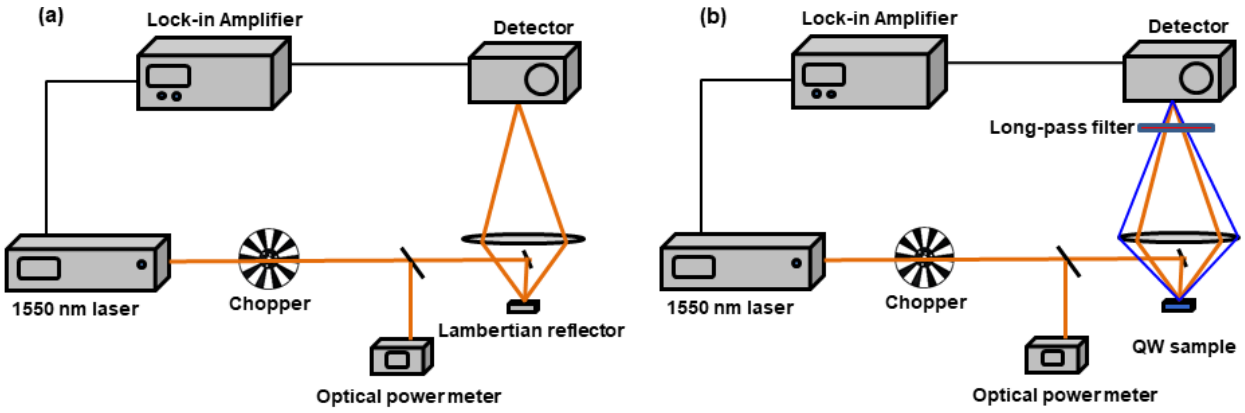

Figure 3.10 (a) PL Quantum Efficiency (PLQE) Measurement Set up. The quantum efficiency of the QW sample is measured by comparing the signal from the QW sample, and the (b) signal from the Lambertian reflector.

The optical set up takes into account the reflectance of the Lambertian reflector, photon flux of the excitation laser, the throughput of the optical set up at the laser wavelength,

contributions from the lens, the long pass filter as well as the responsivity of the photodetector. In Figure 3.10 (a), laser light incident on the reflector forms a characteristic Lambertian distribution with a part of the scattered beam collimated by a lens. The collimated beam, also regarded as the reference signal (S_{ref}) is measured by a detector and is mathematically represented below as:

$$S_{ref} = R_{ref}\varphi_{laser}M_{laser} \quad \text{(Equation 3.1)}$$

where R_{ref} is the Lambertian's reflectance, ϕ_{laser} is the photon flux of the 1550 nm excitation laser. M_{laser} refers to the overall throughput of the optical system at the wavelength of the laser as defined by the respective contributions from the detector's responsivity and the lens. In Figure 3.10 (b), light illumed on the GeSn QW sample emits at a distinct peak wavelength of 2900 nm, and as in the first case but this time with an additional optical component along its path, a portion of the scattered beam is collected by the lens and an additional long pass filter before measurement by the photodetector.

$$S_{PL} = \varphi_{PL}M_{PL} \quad \text{(Equation 3.2)}$$

where ϕ_{PL} refers to the overall photon-flux of the PL emission from the QW sample and M_{PL} is the throughput of the optical system/configuration which includes direct contributions from the lens, long-pass filter as well as the responsivity of the detector. It is noteworthy to mention that the role of the additional long-pass filter is to ward-off scattered laser beams from entering the detector. In this experiment, accurate values of the throughput parameters do not need to need to be known exactly but their ratios (M_{laser}/M_{PL}) can be directly inferred from the transmission characteristics (curves) of both the lens and the long-pass filter as well as the responsivity of the

detector at respective wavelengths. Rearranging equations 3.1 and 3.2, the cumulative photon-flux of the PL emission from the sample is represented below as:

$$\varphi_{PL} = R_{ref}\varphi_{laser}\frac{S_{PL}}{S_{ref}}\frac{M_{laser}}{M_{PL}} \qquad \text{(Equation 3.3)}$$

Considering the above factors, the external quantum efficiency (EQE), η_{ext}, is expressed as the ratio of the number of luminescent photons to the number of absorbed photons:

$$\eta_{ext} = \frac{\varphi_{PL}}{A_{str}\varphi_{laser}} \qquad \text{(Equation 3.4)}$$

where the A_{str} is the absorptance of the quantum well structure at the laser wavelength, while φ_{PL} and φ_{laser} are the respective photon fluxes of the PL and the excitation laser. The absorptance of the sample at the laser wavelength is 60% according to wave-optics calculations. Values obtained from the EQE are directly related to the Spontaneous Quantum Efficiency (η_{sp}) through [104]:

$$\eta_{sp} = \frac{\eta_{ext}}{\gamma_e^f - \eta_{ext}\gamma_r} \qquad \text{(Equation 3.5)}$$

γ_e^f is the photon extraction factor from the front surface, the probability of a luminescent photon to escape front surface to free space. γ_r is the photon recycling factor, the probability of a luminescent photon to be reabsorbed in the active well region of the sample. These factors are obtained through an optical modeling approach that mimics the absorption, emission, transmission and reflection occurrences. The details are presented in the next section.

3.5 Optical Model

We idealize a comprehensive model that simulates optical behaviors of a GeSn single QW structure under a set of guided assumptions [102] [100]. This model strictly accounts for multiple reflection events within the active quantum well region, with the reflectance (R) and transmittance (T) of the front and back surfaces assumed to be between zero and unity; with zero depicting a totally absorbing substrate and unity, a mirror-like reflective substrate. Although, under strict circumstances, the specular reflectance coefficients along the interlayers are modeled by transfer matrix method [105], we idealize a rough mirror-like back surface with a reflectance (R_b) of unity (given that our substrate is a silicon wafer that both exhibit reflective mirror capabilities while casting a Lambertian distribution upon light incidence) with its front surface also assumed to be a smooth isotropic layer allowing light to penetrate through to the active region of the QW structure. Figure 3.11 (a) describes the photon extraction and recycling factors schematics for sets of ideal optical events in a quantum well structure.

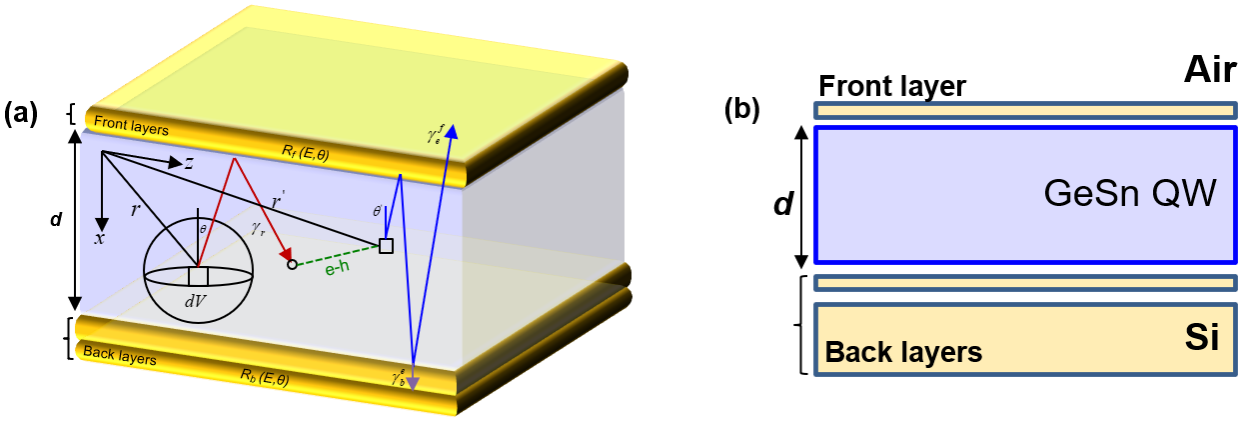

Figure 3.11. (a) 3-D Schematic for modeling photon extraction and recycling factors (Modified from [102]) and (b) shows the idealized structure of the GeSn QW sample with the front and back scattering interlayers.

The red, green and blue lines represent possible reflection events permissible within the quantum well structure. The red directional lineation shows an emitted photon at ***r*** which is later

re-absorbed back into the active layer after a single reflection event at the front; the successive green lineation represents an electron diffusion process; the blue line refers emitted photon (at r') departures after two successive internal reflections while the purple projection represents the probability of photon emission to the back surface (substrate). R_f and R_b are the front and back surface reflection coefficients dependent on the energy and angle of emission.

The following assumptions are strictly considered: i) Although, our quantum well sample is a six-layered structure, our central focus is within the GeSn QW layer (active QW layer) for simplification. Subsequent estimation would include a more complicated structure that directly simulates our sample. ii) The indices of refraction and absorption coefficients for each layers are spatially invariant iii) Isotropic photon emission iv) Ray optics behavior in the active well region with the photon intensity being the only predominating factor v) Photon re-emission from intervening buffer and barriered layers are ignored vi) Substrate is assumed to represent a textured mirror (Figure 3.11 (b)) similar to silicon substrate (R_b = 1.0) and scattering reflected light to Lambertian distribution, while the front surfaces (before the well region) are assumed to be smooth (Air – R_f = 1.0), allowing light to pass through unhindered. Assuming strong absorption limits and neglecting parasitic absorption, the extraction and recycling factors are approximated as [102] [106] :

$$\gamma_e^f \to \left\{ \frac{\varepsilon_f}{4n^2\alpha_o d} : R_b = 1 \right. \qquad \text{(Equation 3.6)}$$

$$\gamma_b^e \to \left\{ \frac{\varepsilon_b}{4\alpha_0 d} : R_b = 1 \right. \qquad \text{(Equation 3.7)}$$

$$\gamma_r = 1 - \gamma_f^e \qquad \text{(Equation 3.8)}$$

ε_b and ε_f are back the front surface emittance, while γ_f^e represents the photon extraction factor from the front surface; a probability metric for quantifying the possibility of photon emission to the substrate. This parameter is strictly considered in the calculation of the photon recycling factor as depicted in Equation 3.8. The refractive index and absorption coefficient of GeSn (13.5% Sn) sample are extracted from ellipsometry measurements and reported as 4.2 and 60362.22cm^{-1} [103]. Using ray optics, the calculated emittance of the idealized structure is derived as [100] [107]:

$$\varepsilon_f = n_r^2 \int_0^{\theta_c} 2\sin\theta\cos\theta\left[1-\exp\left(-\alpha d/\cos\theta\right)+\exp\left(-\alpha d/\cos\theta\right)R_b x\frac{1}{1-R_b y}\right]d\theta \quad \text{(Equation 3.9)}$$

$$\varepsilon_b = (1-R_b)x\frac{1}{1-R_b y} \quad \text{(Equation 3.10)}$$

$$x = \int_0^{\theta_c} 2\sin\theta\cos\theta\left[1-\exp 2\alpha d/\cos\theta\right]d\theta + \int_{\theta_c}^{\pi/2} 2\sin\theta\cos\theta\left[1-\exp 2\alpha d/\cos\theta\right]d\theta \quad \text{(Equation 3.11)}$$

$$y = \int_{\theta_c}^{\pi/2} 2\sin\theta\cos\theta\left[1-\exp 2\alpha d/\cos\theta\right]d\theta \quad \text{(Equation 3.12)}$$

The analysis of the estimated quantum efficiencies based on the above theoretical formulations are presented in the next section.

3.6 Quantum Efficiency Analysis – Result and Discussions

The quantum efficiency of the QW sample (sample A) is presented in Figure 3.12 below. The estimated values of the external and spontaneous quantum efficiencies as a function of the photon incidence rate are reported accordingly. Based on the experimental and theoretical formulations above, the estimated peak EQE at the photon incidence rate of 4.0 x 10^{20}

photon/secs is 1.45%, while the calculated photon recycling (γ_r) and extraction (γ_e^f) factors (from the front surface) are 97.79% and 2.41% respectively.

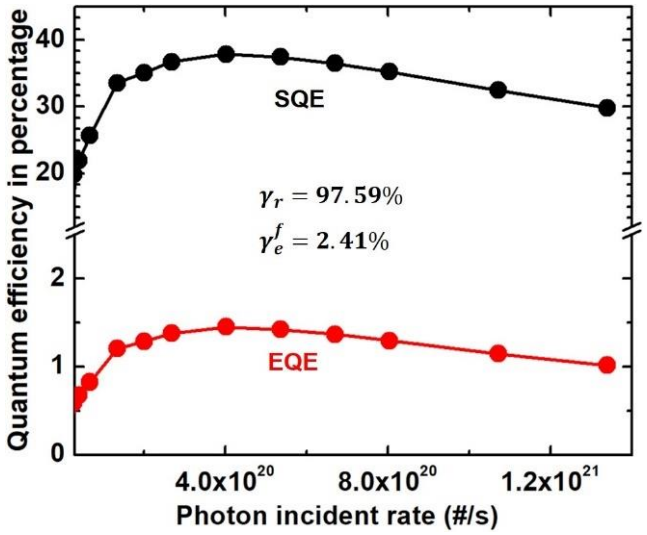

Figure 3.12: External and spontaneous quantum efficiency as a function of the photon incidence at 20 K. The photon recycling (γ_r) and extraction (γ_e^f) factors from the front surface are 97.79% and 2.41% respectively.

Based on these values, the peak SQE was estimated as 37.90%. It is worth noting that the estimated SQE of InGaAs/GaAs Multi-Quantum wells (MQWs) at about the same material developmental stage in the 1990s was between 50% to 60% [108,109]. Comparatively, the estimated SQE for a single GeSn QW is about 10-20% less than those estimated for III-IV material at about the same material development which goes further to attest the promise of this alloy system for its targeted applications.

Although the reported EQE and SQE for this QW sample looks promising, their weak dependence on the photon incidence rate is of great concern.

This weak dependence is hypothesized to be due to the p-type background doping (~10^{17} cm^{-3}) in the GeSn well (unintentionally-doped) which had it been controlled, could have resulted in a much

higher carrier densities whilst strengthening the dependence of the QEs on the photon incidence rate. Previous reports also show the effect of doping concentration on a material's estimated QE [105], which can be improved systematically by optimizing the background doping concentration in the active region of the well.

3.7 Conclusion

This work systematically explores the optical characteristics of two SiGeSn/GeSn quantum wells with differing well widths/thicknesses. The quantum well structures; one with thicker well-width (22-nm), the other relatively thinner width (9-nm) were grown via a reduced-pressure chemical vapor deposition system with adherence to growth precision controls. Temperature and power dependent photoluminescence measurements were obtained and analyzed with the thicker well sample showing a significantly improved PL emission as evidenced by a lowered first quantized energy level in the T-valley. Emission wavelength was also seen to extended to nearly 2500-nm due to the ease in compressive strain. External and peak spontaneous quantum efficiencies were calculated and found to be 1.45% and 37.90% respectively. Reports show that the QE can be improved significantly by optimizing the background doping concentration in the active region of the well.

Chapter 4: SiGeSn/GeSn/SiGeSn Separate Confinement Heterostructure

4.1 Introduction

Optoelectronics integrated devices have recently been favored by cutting-edge innovative and incremental developments of Group IV alloy material systems. From growth technological advancements [110–112] to functional device fabrication [73,80], the realization of a truly monolithic integration of photonic circuits on Si platform has come to stay, breaking beyond its decades-old prophecy. Today's GeSn-based emitters are a reality following the achievement of a truly direct bandgap material that leans favorably to the strategies of increased Sn incorporation, lattice and bandgap tunability. These unique characteristics have given rise to early developments in GeSn material designs which became the foundation of current bulk [113–116] and QW heterostructures [24,44,53,58,79,90,117,118]. The evolved designs of these QW structures were progressively applied to LEDs and lasers devices with the aim to achieve improved optical emissions and carrier confinements (Figure 4.1 (a)–(c)). These device performance goals promptly became the motivation for designing the first Ge/GeSn/Ge QW heterostructure which bases off its active design construct on Ge-bounded GeSn QW layer (Figure 4.1 (a)). The adoption of Ge as barrier in a Ge/GeSn QW system has been vastly reported in previous studies [42,52–58]. Summarized versions of these body of work revealed that a direct bandgap material cannot be realized due to the large compressive strain in the QW well. The authors also proposed the use of GeSn as barriers to mitigate this challenge (Figure 4.1 (b)) [59]. Interestingly, this strategy worked as it eased the compressive strain while also achieving a direct bandgap QW with Type I band-alignment. However, beyond a compositional alloy range the material fails giving rise to the suggestion of SiGeSn barrier (Figure 4.1 (c)).

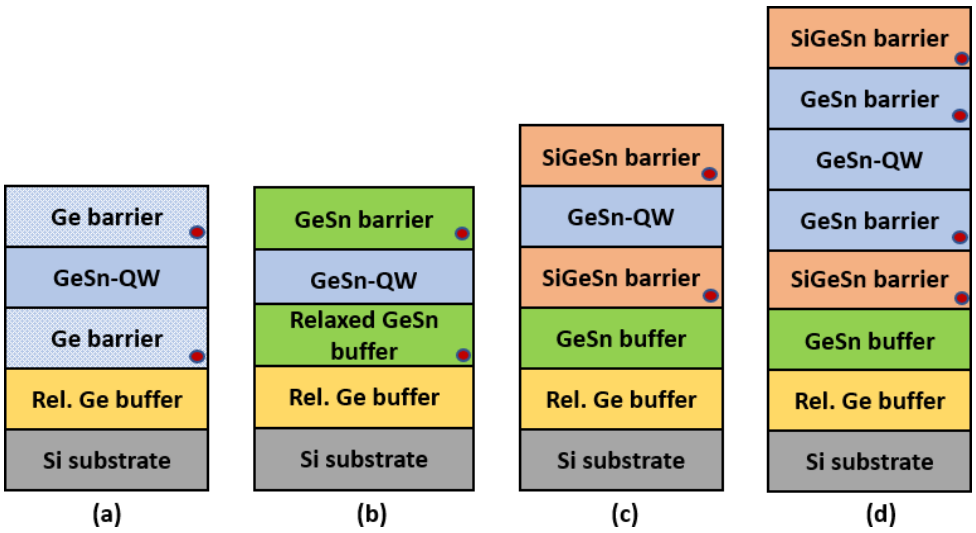

Figure 4.1. Schematic evolution of GeSn QW structures showing (a) Ge-barrier/GeSn QW (b) GeSn barrier/GeSn QW (c) SiGeSn barrier/GeSn QW and, (d) SiGeSn barrier/GeSn barrier/GeSn SCH QW. The blue-cladded red dots indicate the respective barriers of each structure.

For instance, in 2018, Grant et al. [112], designed and grew GeSn/GeSn/GeSn QW structure comprising of $Ge_{0.86}Sn_{0.14}$ well (14% Sn) and $Ge_{0.92}Sn_{0.08}$ (8% Sn) buffer layers. The growth resulted in a direct bandgap QW of 22 meV L-T separation ($\Delta E_{L\text{-}\Gamma}$) and a 20 meV Γ valley barrier height (ΔE_{Γ}). Based on their initial findings, an incremental investigation employed the logical strategy of increasing the Sn compositions in the well (15.3%) and buffer (9.4%) layers [119]. This approach gave rise to a more direct bandgap QW featuring a comparatively improved $\Delta E_{L\text{-}\Gamma}$ (52 meV) and ΔE_{Γ} (35 meV) values. Unfortunately, this strategy is only possible when the difference between the Sn compositions between the GeSn barrier and the well is less than ~ 6%. Beyond this difference, the built-up compressive strain within the well will neither result in direct bandgap material or favorable Γ valley barrier height as expected. However, beyond a compositional alloy range the material fails giving rise to the suggestion of SiGeSn barrier.

The introduction of the SiGeSn barrier opens up a wide range of possibilities since their lattice parameters and bandgaps can be engineered by tuning the Si and Sn compositions. Although, the SiGeSn/GeSn are slightly more stable than the previous design adoptions they still suffer from carrier leakage inefficiencies. To solve this challenge, an incremental design strategy was suggested to increase the thickness of the GeSn QW which significantly improved the PL emission [60]. To further improve PL emission and carrier confinement with reduced leakage, a separate confined heterostructure was suggested (Figure 4.1 (d)).

In this work, a SiGeSn/GeSn/GeSn/GeSn/SiGeSn single separate confinement heterostructure (SCH) quantum well was grown, characterized and compared to previously reported 9-nm and 22-nm non-SCH conventional single quantum wells. The significantly enhanced emission from SCH quantum well was obtained as a result of separately confined quantum well active region, which is mainly due to a much lowered first quantized energy level in Γ valley and a significantly higher energy level in the L-valley. The significance of the band structure evolution is demonstrated in the stronger carrier confinement, improved QW emission and reduced carrier leakage.

4.2 Experimental Details

4.2.1 Growth and Characterizations

The separate confinement heterostructure was grown in a state-of-the-art ASM 2000-Plus reduced vapor deposition machine (RPCVD) using appropriate Si, Ge, and Sn precursor gases as those used in the previous chapters. As shown in Figure 4.1 (a), the entire structure features a nominal 600-nm grown Ge buffer, a 600-nm thick $Ge_{0.85}Sn_{0.11}$ buffer, a 50-nm thick $Si_{0.047}Ge_{0.890}Sn_{0.063}$ bottom barrier followed by separately-confined layers of consecutively

grown GeSn layers that consists of a $Ge_{0.85}Sn_{0.15}$ QW layer bounded on opposite sides by $Ge_{0.89}Sn_{0.11}$ barriers of same compositions. The SCH structure is finally completed by adding a capped layer of 8-nm-thick $Si_{0.03}Ge_{0.89}Sn_{0.08}$ top barrier. To affirm the enhanced optical characteristics of this SCH structures, two single quantum well (SQW) structures of similar Sn compositions, $Ge_{0.865}Sn_{0.135}$ (Reference A) and $Ge_{0.87}Sn_{0.13}$ (Reference B) were chosen and characterized in similar fashion. Figure 4.1 shows the structural schematics of SCH QW structure, Reference Sample A and Reference sample B.

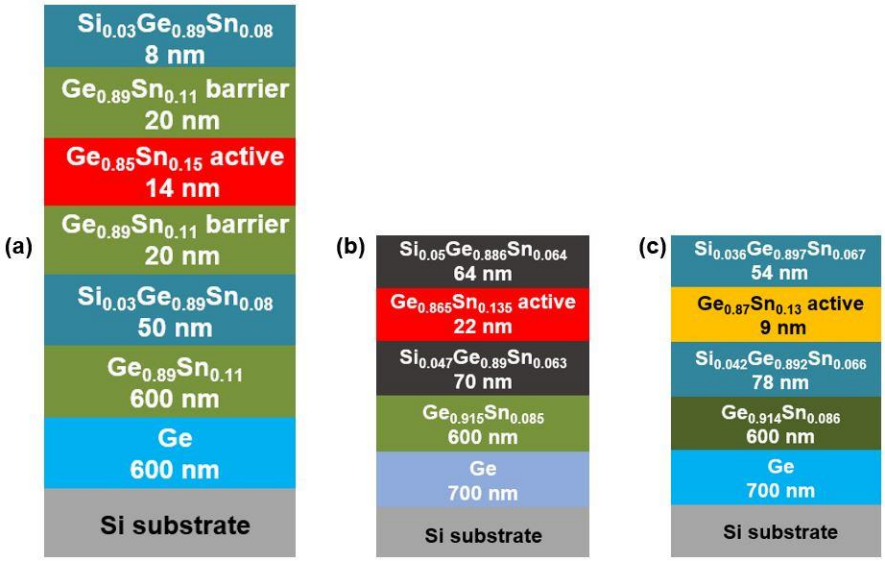

Figure 4.1. Cross-sectional schematics of the SCH QW sample, (b) Reference sample A and (c) sample B.

4.2.2 SCH Structure Design Rationale

The alloy composition of $Ge_{0.85}Sn_{0.15}$ QW layer was selected to ensure pseudomorphic growth with the Ge buffer. This introduces a high enough compressive strain that is later compensated by the growth of a $Ge_{0.89}Sn_{0.11}$ buffer layer. The possibility of which is based on the condition that the GeSn buffer layer is closely lattice-matched to the $Ge_{0.85}Sn_{0.15}$ QW layer. The

result of this approach is a direct bandgap QW layer with a sufficiently-reduced compressive strain. To improve carrier confinement within the well, cladding layers of appropriate SiGeSn compositions are introduced. The compositions of these layers ($Si_{0.03}Ge_{0.89}Sn_{0.08}$ top and bottom cladding/barrier) are carefully selected to also lattice-match the GeSn buffer layer while creating sufficient barrier height to ensure confinement. Note that the available SiGeSn alloy material is based on our current growth capability. To further strengthen the carrier confinement, GeSn barrier layers that are lattice matched to the GeSn buffer layers are grown before and after the growth of the GeSn QW layers. It is important to note that all the layered material compositions are selected to favor a tightly-confined direct bandgap GeSn QW.

Photoluminescence spectra and band diagrams of the QW structures were obtained and analyzed with the aim to compare their emission and transmission characteristics. It should be mentioned that the significant difference between Reference sample A (22 nm) and Reference sample B (9 nm) is their QW layer thicknesses. The growth and optical characteristics of the samples are detailed in Chapter 3 and in reference [24]. The completion of the SCH RPCVD growth (Sample A) is followed by a number of structural and optical characterization techniques such as high-resolution x-ray diffraction (HRXRD) 2theta-omega scan, XRD reciprocal space map (RSMs), cross-sectional transmission electron microcopy (TEM) and photoluminescence measurements. The XRD measurements provide strain and Sn compositions of each layer, while the TEM probes the quality of the growth as well as provides a more accurate measure of the layer thicknesses. Figure 4.2 shows the HRXRD 2theta-omega scan and the RSM of the SCH QW structure.

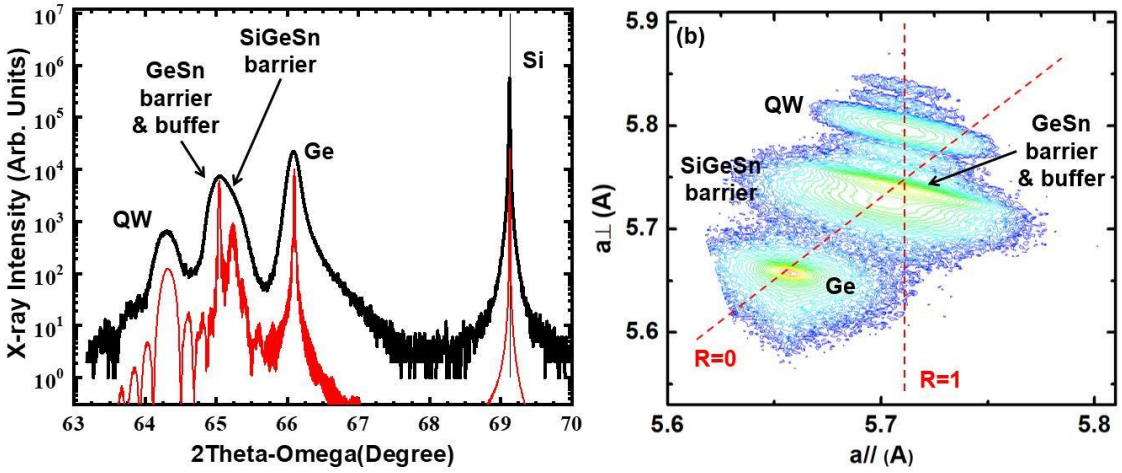

Figure 4.2. (a) HRXRD 2θ-ω scan of SCH QW sample showing each resolved peak. Black and red curves represent the experimental and simulated results. (b) Reciprocal space map showing the respective layer peaks.

Black and red delineations on the plot represents experimental and simulated scans, respectively. Lattice constant and thickness of the respective layers were extracted from the simulated curve. The experimental and simulated curves show distinct and well-resolved peaks assigned to the Ge buffer, GeSn buffer, SiGeSn barrier, GeSn barriers and the GeSn QW respectively. In same order, these peaks correspond to the elemental and alloy presence are 66.08°, 64.30°, 65.07°, 64.30° and 63.76° respectively. As mentioned above, the extracted thicknesses of the respective layers from the from the simulated data are matched with the TEM results to ensure accuracy. To quantify the structural parameters, theoretical derivations of Vegard's law was employed to infer the lattice constant of the respective layers. The strain within each layer was also obtained from the RSM data as shown in Table 4.1.

Based on the strain extractions, Ge and GeSn buffers exhibit tensile (0.25%) and compressive (-0.17%) character, respectively. The SiGeSn cladding layers, GeSn well and GeSn barriers are subjected to tensile (0.13%), compressive (-0.63%) and compressive (-0.63%) strains respectively. The strain character adopted by these layers are the result of their pseudomorphic

growth to the GeSn buffer layer. A summary of the material characterization extracts for SCH QW sample, Reference sample A and Reference sample B are reported in Table 4.1.

Table 4.1. Structural information of the QW study samples

Sample ID	**Layer**	**Thickness (nm)**	**Si (%)**	**Sn (%)**	**Strain (%)**	**2θ-ω Peak**
SCH QW	Ge Buffer	600	0	0	0.25	66.08
	GeSn Buffer	600	0	11	-0.17	64.3
	SiGeSn Bottom Barrier	50	3	8	0.13	65.07
	GeSn Barrier-1	20	0	11	-0.63	64.3
	GeSn Quantum Well	14	0	15	-0.63	63.76
	GeSn Barrier-2	50	0	11	-0.63	64.3
	SiGeSn Top Barrier	50	3	8	0.13	65.07
Reference A	Ge Buffer	700	0	0	0.2	66.07
	GeSn Buffer	600	0	8.6	-0.2	64.97
	SiGeSn Bottom Barrier	78	4.2	6.6	0.25	65.43
	GeSn Quantum Well	9	0	13	-0.92	64.02
	SiGeSn Top Barrier	54	3.6	6.7	0.25	65.54
Reference B	Ge Buffer	700	0	0	0.2	66.09
	GeSn Buffer	600	0	8.5	-0.2	64.96
	SiGeSn Bottom Barrier	70	4.7	6.3	0.28	65.52
	GeSn Quantum Well	22	0	13.5	-0.94	63.85
	SiGeSn Top Barrier	64	5.0	6.4	0.28	65.52

Figure 4.3 shows the cross-sectional TEM image of the SCH QW structure. All buffer, barrier and QW well layers are clearly resolved with no threading dislocation protruding through the GeSn QW layer. Extracted thickness values from the simulated 2theta-omega scans match the TEM thicknesses indicating a well-controlled growth.

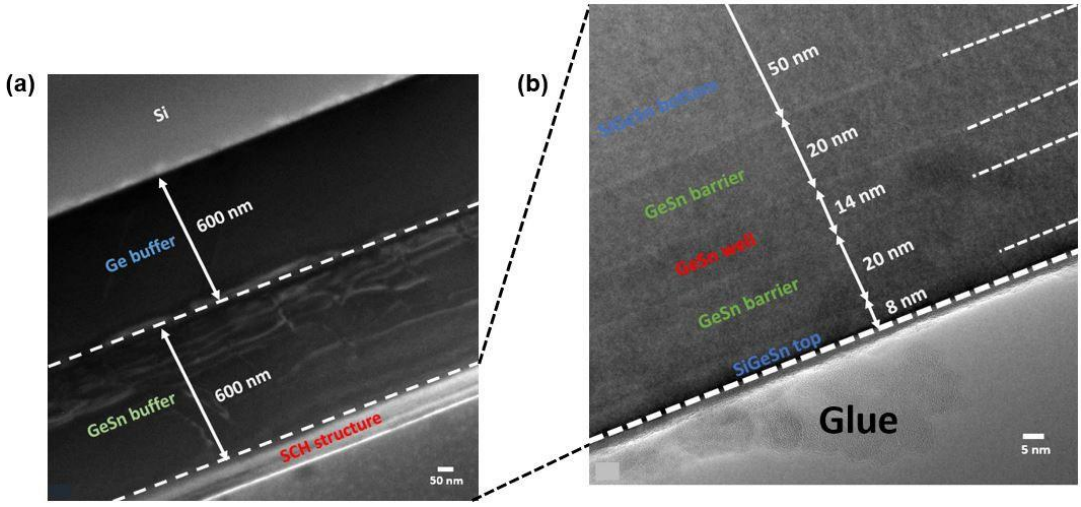

Figure 4.3. (a) TEM image of the sample showing the entire structure (c) Magnified TEM image of the QW active region.

4.3 Band Structure Calculation

Using experimental data from these QW samples, band structure diagrams were calculated and analyzed for a fuller picture of the optical transitions. These constructions are prepared based on the their behaviors at 300 K with relevant band structure parameters such as the bowing parameters set to achieve direct and indirect energy characteristics that base strictly on the application of Vegard's law. Propagation matrix and effective mass propagation methods were applied to generate respective electronic band structures. Conduction and valence band offset approximations are based on methods described in refs. [33,86,120].

4.4 Optical Characterization & Analysis

Temperature and power-dependent PL measurements were collected using a standardized off-axis PL arrangement enabled by a lock-in technique (chopper applied at 400 Hz). The characteristic PL emissions were measured using a spectrometer connected to an InSb detector with a cut-off response of 3.0 μm. To ascertain the optical transition information, two excitation

laser beams with disparate penetration depth and energies were used: a 532 nm continuous wave (CW) and a 1550 nm CW laser.

A pumping power-dependent PL spectra was measured at 20K, followed by PL peak analysis using Gaussian fitting to investigate the integrated PL intensities. Preferentially, a low power range of between 0.5 mW-20mW was applied to mitigate excessive carrier leakage potentialities. Emission characteristics were then compared to two similar QW non-SCH reference samples; one with a thick well region (22 nm, Reference sample A) and the other a thin well (9 nm, Reference sample B). The detailed reports of the reference samples can be found in our most recent quantum well papers[24]. Figure 4.4 (a) –(c) shows the PL outcomes of the three structures under 532 nm laser.

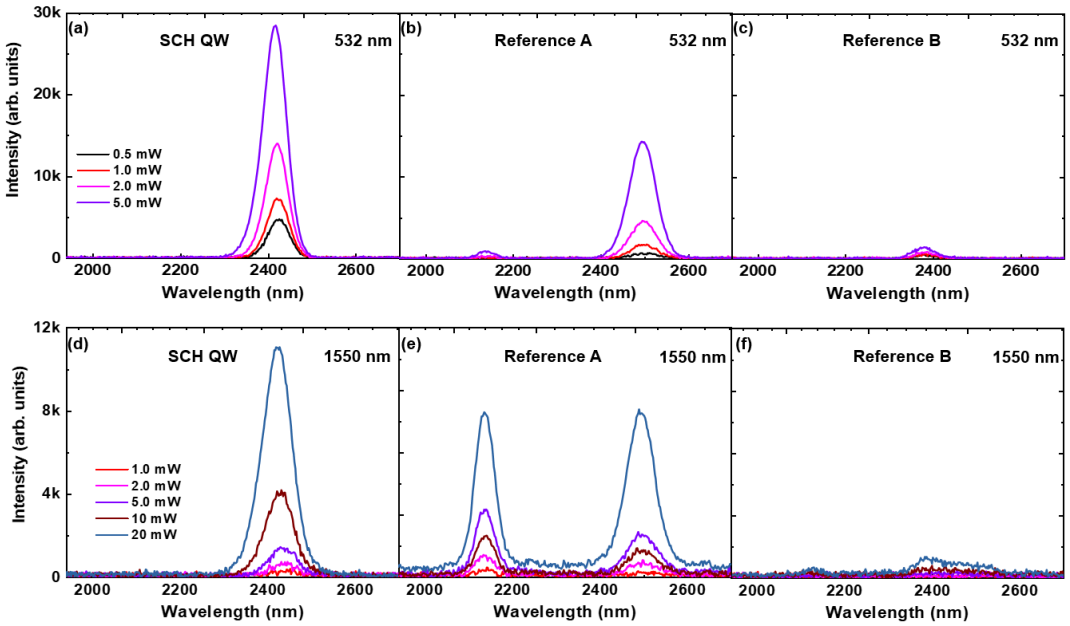

Figure 4.4. Linear-scale power-dependent PL spectra at 20 K under (a-c) 532 nm and, (e-f) 1550 nm pumping lasers. The PL intensity of the SCH sample is nearly 2x stronger than Ref. sample A and approximately 3x stronger than Ref. sample B.

As observed, the PL characteristics of the SCH structures bodes significantly stronger than the intensities reported for the reference samples. Quantitatively, we see an approximately 2x intensity improvement when compared to the thicker well sample and nearly 3x the comparison against the thinner well (9-nm) reference sample.

The power-dependent PL spectrum shown above are re-plotted in log-scale to identify the dominant peaks and optical transitions. Figure 88 below shows the PL spectra plots under 532 nm excitation lasers for the SCH QW sample and reference samples A & B. Each column shows the PL spectra and the band structure representing the dominant optical transition events for each sample. Based on the plot, Figure 4.4 (a) shows the PL spectra from the SCH QW sample under the 532 nm laser at different excitation pumping power. As seen, the peaks grow as the injection power increases and emanates predominantly from the GeSn QW emissions. The origins of the peaks are confirmed by the obvious blue shift that occurs as the injection power increases. These blue shift events are driven by typical band filling events that exists in quantum wells upon gradual carrier injection increments [92].

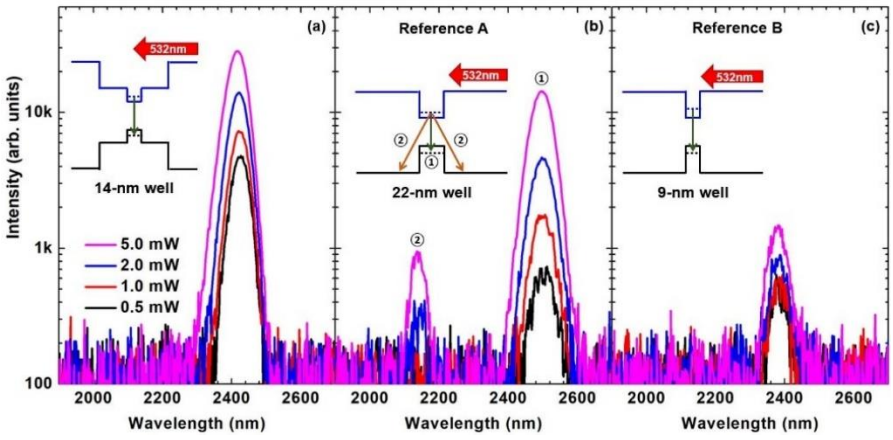

Figure 4. 5. Log-scale power-dependent PL spectra under 532-nm pumping laser at 20 K for the SCH QW sample (b) Reference sample A and, (c) Reference sample B. The insets in each panel represents the dominant optical transitions for each sample.

According the band diagram in the inset, these power-dependent QW emissions originate from the first energy level of the Γ valley to the HH band in the GeSn QW. This is due to the fact that at low temperatures, the electrons are strongly confined in the Γ valley of the QW while the holes are also as strongly confined in the HH band; resulting in an improved overall carrier confinement. Compared to Figures 4.5 (a), reference samples A (Figures 4.5 (b)) exhibit two predominant peaks emanating from optical transitions between the: i) first energy level of the Γ valley and the HH band in the GeSn QW (Peaks ①) and, ii) QW Γ valley's first energy level and the LH band in the SiGeSn top barrier. the GeSn buffer layers (Peaks ③). As with the SCH QW sample, the longer wavelength peaks, Peaks ①, are attributed to the QW emissions and exhibit same blue-shift observed in quantum wells. On the other hand, the shorter wavelength peaks, peaks ③, shows non-obvious peak shifts and originate from optical transitions between the QW Γ valley's first energy level and the LH band in the SiGeSn top barrier. The emergence of these peaks is due to the improved carrier confinement at lower temperatures. At these low temperatures, electrons are better confined within the Γ valley of QW layer while holes are also as much confined to the LH band of the SiGeSn top barrier layer due to a significantly high hole population. As a result, transitions of these types are further enhanced.

As is the case for the SCH QW sample, the peaks from reference sample B (Figure 4.5 (c)) are attributed to the QW emission indicating optical transitions from the first energy level of the Γ valley to the HH band in the GeSn QW. The peaks also exhibit the characteristic blue-shift as the injection power increases and confirms their origin to be from the QW emission.
Figure 4.5 below shows the PL spectra plots under 1550 nm excitation lasers for the SCH QW sample and reference samples A & B. While the optical penetration depths for the 532 nm pumping lasers are shallower (~ 21 nm), the penetration power of the 1550 nm lasers are deeper (~ 1000

nm) and are more likely to activate optical events below the GeSn QW layer. Based on the plot, Figure 88 (a) shows the PL spectra from the SCH QW sample (14 nm well) under the 1550 nm laser under different excitation pumping power and measured at 20 K.

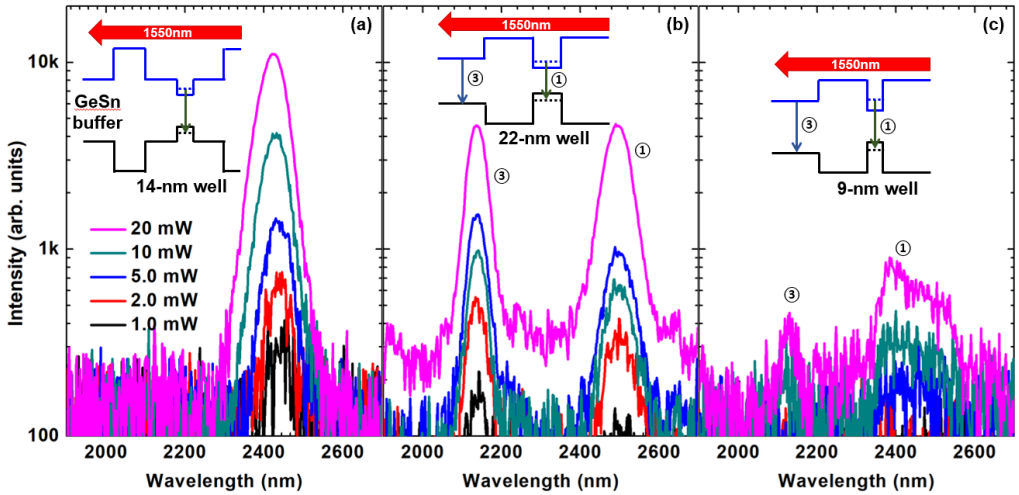

Figure 4.5. Log-scale power-dependent PL spectra under 1550-nm pumping laser at 20 K for the SCH QW sample (b) Reference sample A and, (c) Reference sample B. The insets in each panel represents the dominant optical transitions for each sample.

In similar fashion as in previous analysis, these peaks are also observed to increase as a function of increasing injection power. Notice the blue shift as the carrier injection increases – a clear evidence of the earlier mentioned band filling effect. In this case, these peaks also assign dominantly to the QW emissions as a result of the optical transition between the first energy level of the Γ valley and the HH band in the GeSn QW (see inset). As previously mentioned, the emissions from the SCH QW samples are stronger than those observed from reference samples A (22 nm well) and B (9 nm well). Compared to the SCH QW sample (Figures 4.5 (a)), reference samples A and B (Figures 99 (b) and (c)) exhibit two predominant peaks emanating from the optical transitions between the i) first energy level of the Γ valley and the HH band in the GeSn QW (Peaks ①) and, ii) GeSn buffer's Γ valley in the conduction band and the HH band in the

valence band (Peaks ③). The longer wavelength peaks, Peaks ①, are attributed to the QW emissions and exhibit same blue-shift observed in quantum wells. On the other hand, the shorter wavelength peaks, peaks ③, show non-obvious peak shifts and originate from optical transitions between the GeSn buffer's Γ valley in the conduction band and the HH band in the valence band (Peaks ③). Figure 4.6 compares the band structures of the SCH QW samples and reference samples A and B. Table 4.2 also shows the calculated band diagram information.

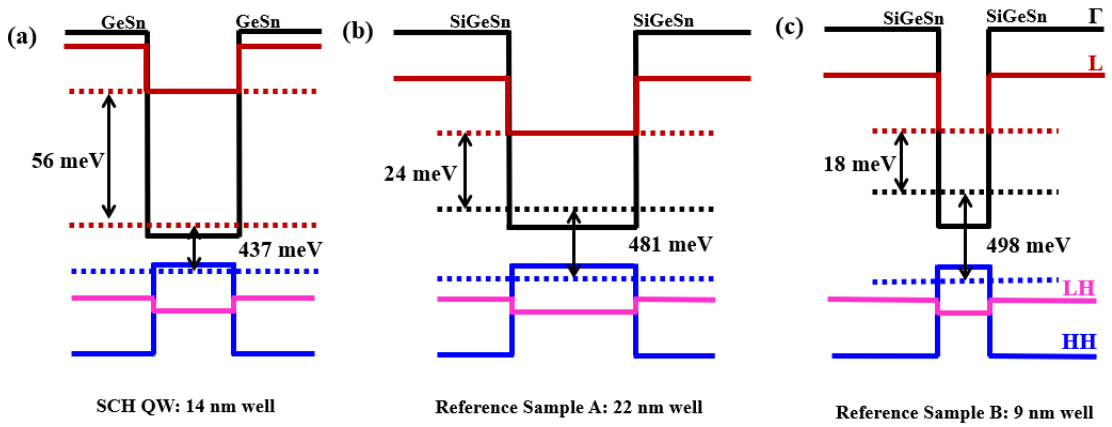

Figure 4.6. Band structures of the (a) SCH QW samples, (b) Reference sample A and, (C) Reference sample B.

Table 4.2. Summary of relevant band diagram information

Sample	Buffer	Barrier	QW Sn%	L-Γ Sep. (meV)	Γ Sep. (meV)	Ground energy confinement (meV)	Γ-HH Sep. (Ground level) (meV)
SCH QW	$Ge_{0.915}Sn_{0.085}$	$Si_{0.047}Ge_{0.89}Sn_{0.063}$	15	68	94	24	437
Ref. A	$Ge_{0.914}Sn_{0.086}$	$Si_{0.047}Ge_{0.890}Sn_{0.063}$	14	52	90	24	481
Ref. B	$Ge_{0.914}Sn_{0.086}$	$Si_{0.042}Ge_{0.892}Sn_{0.066}$	13	50	88	18	498

* Sep. is denoted as Separation

The band diagram brings to focus the quantum well regions of the sample with the SCH QW presenting the presenting the highest ground energy level confinement in the conduction band (56 meV) followed by reference sample A (24 meV), then reference sample B (18 meV).

The energy difference between the ground state energy levels of the electrons in the CB and the HH also decrease from left (SCH sample – 437 meV) to right (Reference sample B – 498 meV). Other information such as the L-Γ and Γ valley separations of the respective samples are shown in Table 4.2. Based on the optical transition analysis, SCH QW shows a significantly higher carrier confinement and optical emission characteristics compared to reference samples A and B. The detailed band diagrams and optical transition information of all the samples are shown in Appendix B. Following the optical analysis, the integrated PL peak intensities of QW peak were extracted to further investigate QW optical property. PL data of Reference Sample A and B were also presented to facilitate the analysis. Pumping power-dependent PL peak intensities at 20 K for 532 nm and 1550 nm lasers were plotted in Fig. 3(a) & (b).

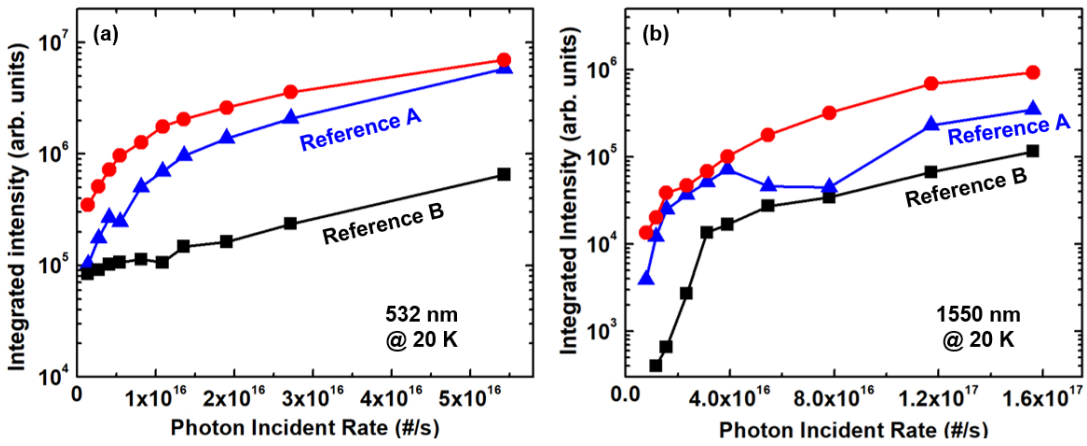

Figure 4.7. Pumping power-dependent PL integrated intensities at 20K for (a) 532-nm and (b) 1550-nm lasers. Data of reference samples A & B were also plotted for comparison. Both figures show comparatively stronger PL emissions from the SCH QW structure (Sample A).

Under each excitation laser, the intensity of the SCH structure exhibits stronger emission compared to the reference samples owing to a better confined carrier in the well – mainly advantaged by the initiative to optimize the structure around the active region. Evidently, all three samples display an emission saturation at high carrier injection densities, which is due to the filling of the CB and VB[24].

4.5 Conclusion

In this work, a SiGeSn/GeSn/GeSn/GeSn/SiGeSn single separate confinement heterostructure (SCH) quantum well was grown, characterized and compared to previously reported 9-nm (ref. B) and 22-nm non-SCH (ref. A) conventional single quantum wells. The significantly enhanced emission from SCH quantum well was obtained as a result of separately confined quantum well active region. Based on the optical transition analysis, SCH QW also shows a significantly higher carrier confinement compared to reference samples A and B. The significance of the band structure evolution from the thinner QW to the SCH QW is demonstrated in the stronger carrier confinement, improved QW emissions and reduced carrier leakage.

Chapter 5: Stability investigations of GeSn/Ge heterostructures under thermal annealing

5.1 Introduction

Recent advances in Group IV semiconductor research has continued to promote their practicalities for a wide-range of cutting-edge optoelectronic and photonic applications [4,17]. An exceptional characteristic of this alloy system, is retained in the ability to tune their bandgap and/or lattice constants through an intentional compositional variation. For instance, by tuning the Sn composition in Ge_xSn_{1-x} alloy, it is possible to achieve an optimized optical character that favors specific photonic needs, as demonstrated in these authors: laser diodes[11], light emitters [78] and photodetectors [121]. An even more unique outlook on the GeSn bi-alloy devices is hinged on its facility to be monolithically integrated on silicon (Si) platform. This is perhaps applicable through a specialized complementary metal oxide (CMOS) technique [122,123]. This makes it possible to create monolithically integrated GeSn-on Si platform optoelectronics and photonic devices that operate in the near-to-mid-infrared spectrum range [124–126]. These rare applicational features thrive on the fundamental optical character of the GeSn semiconductor through the addition of α-Sn in Ge matrix which makes it possible to transform an indirect bandgap form of the GeSn material to a direct bandgap form. This direct to indirect bandgap transition is achieved by increasing the Sn composition until the near-to-mid-infrared objective is realized. For instance, theoretical predictions have favored the addition of about 7-12% Sn composition to the alloy mix [76,127,128] to transform Ge indirect bandgap to a direct GeSn bandgap material. In reality, the gradual addition of Sn lowers the bandgap separation between the indirect L-valley and direct Γ-valley until there is an absolute match (zero), and then, upon further Sn addition, the position of the direct and the indirect band reverses (sign changes). It is noteworthy to mention that near the indirect-to-direct transition point, the sensitivity of the GeSn

optical properties is especially high to both strain and Sn compositions. In fact, on the experimental end, the growth of high Sn composition under compressive strain has been demonstrated by researchers, despite the limited 1% low-solubility challenge of Sn in Ge matrix[129]. This breakthrough continues to enable the possibility of indirect-to-direct transitions [116,130,131] while also ushering the fabrication of cutting-edge GeSn devices with high emission characteristics. However, the challenge of increasing/maximizing the amounts of Sn in GeSn alloys as well as the improving the stability of high-Sn GeSn devices operating above room temperatures (RT) should be thoroughly investigated.

For instance, a study by Wei Du et al.[8] explored the connection and competition between direct and indirect bandgap GeSn materials with sufficient Sn compositions. Their findings reveal that a continual increase in Sn content tend to favor indirect to direct optical shifts thereby resulting in a rapid enhancement of direct transition over the indirect transition. In another study, Harris et al.[132] uncovered the indirect-to-direct transition points of unstrained Ge_xSn_{1-x} (6.7% Sn) GeSn sample through a set of PL measurements taken at different temperatures. A separate investigation also detailed the role of strain in optical transitions in $Ge_{0.875}Sn_{0.125}$ by studying the PL dependence on excitation pumping power, compressive strain and temperatures[133]. A complementary study from Stanchu et al.[134] recently examined the relationship between misfit dislocation, strain relief, Sn out-diffusion, and strain relief in 300^{o}C annealed GeSn samples. This study reveals strong correlation between composition, defect density, strain and optical performance of GeSn devices operating at and above RT.

In this work, we will investigate, using GeSn samples with Sn compositions of 8 to 10%, the competition between direct and indirect optical transitions, at temperatures above RT. The aim of this study is to determine: i) the correlation between composition, defect density, strain and PL

observed before and after thermal annealing, and ii) and analyze the impact of strain on the device performance of as-grown GeSn samples as well as its annealed variants especially at temperatures above room temperatures (300^{o}C).

5.2 Materials Characterization

In this work, GeSn samples with specific Sn compositional range (8% to 10%) were selected to indicate samples with Sn contents that fall within the predicted theoretical indirect-to-direct transition point (additional reasons are identified in preceding sections). These samples were grown using the standard ASM Epsilon reduced pressure chemical vapor deposition (RPCVD) system. Before the growth of the GeSn sample, an epi-growth is initiated with the deposition of a 700-nm thick Ge (001) buffer layer on a hydrogen-passivated Si (001) substrate that tends to a complementary metal oxide (CMOS) compatibility process. The level of strain in each sample was achieved by a number of growth-dependent variables, such as, temperature, thickness and the growth rate. To investigate the relationship between composition, defect density, strain and PL at temperatures above RT, the impact of thermal annealing on the optical transition of four GeSn samples (S14, S15, S29, and S32) of different Sn contents (Figure 5.4) were studied.

Prior to the annealing procedures, these samples were cleaved from the center position of an as-grown 4-inch diameter wafer where the probability of uniform deposition is relatively highest. Four separate pieces were diced from each sample, with one kept as the 'as-grown' piece while the other 3 samples were annealed in vacuum at 300^{o}C for 2, 4 and 8 hours, respectively. Sn compositions, lattice constants, strain parameters and defect density information of the as-grown and annealed samples were extracted from rocking-curve XRD and reciprocal

space maps (RSMs) (Figure 5.2) measurements through a standard Panalytical X'pert Pro MRD diffractometer, coupled with modeling[134].

The optical characteristics of the GeSn samples were investigated using a standard off-axis PL set up comprised of an assembly of lens and mirrors, lock-in amplifier and a spectrometer attached to an InSb detector with a cut-off wavelength of approximately 3.0 μm. Successive PL measurements were studied to analyze the competition between the direct and indirect optical transitions. To aid such analysis, the spectral peaks were also extracted using the Gaussian-fitting procedure. Either a 532-nm continuous wavelet (CW) or a 1064-nm pulsed (pulse width of 5ns and repetition rate of 45kHz) excitation lasers were employed to probe the samples as the choice of use depends strictly on the thicknesses and/or the optical penetration depths of each laser [88]. Temperature-dependent PL measurements of were obtained by placing the samples in an enclosed helium cryostat with temperatures varied from 10 k to 300 K. The peaks and integrated intensities of the temperature-dependent spectra were extracted, analyzed and matched to their corresponding optical transitions. Table 5.1 shows the summarized lasing parameters used in this study.

Table 5.1. Excitation laser pumping parameters

Laser Wavelength (nm)	Spot Diameter (μm)	Average Power (mW)	Average Power Density (kW/cm^2)	Excitation Carrier Density ($Photon/s/cm^2$)	Penetration Depth (nm)
532	64	500	15	4.1×10^{19}	~ 100
1064	51	300	6	3.5×10^{22}	~ 900

In addition to the reason stated in the introductory statement of the material characterization section, the samples used in this study were selected to fulfil certain criteria as stated below:

i) To select samples that possess the same level of strain as well as similar Sn composition. This way it is easier to compare the impact of thermal annealing on unannealed samples with same strain and similar Sn content. For instance, samples S14 and S15 possess the same strain at -10×10^{-3} while also having similar Sn compositions of 8% and 9% respectively. The same goes for samples S29 and S32 with same strain at -5×10^{-3} as well as similar Sn compositions of 9% and 10% respectively

ii) To select samples with the same Sn composition but different strain levels thus creating the possibility of comparing the structural and optical characteristics of samples of this nature. For example, samples S15 and S29 both have the same Sn compositions of 9% but different strain levels of -10×10^{-3} and -5×10^{-3} respectively. The difference in strain levels is determined by the samples thicknesses which also differs proportionately iii) It cannot be overstated that the primary reason for selecting these samples (S14, S15, S29 and S32) is based on the range of their measured Sn compositions (8% to 10%) which places them on the predicted indirect to direct transition point where the optical properties are highly sensitive to changes in strain and composition. With this level of sensitivity, it is possible to investigate the correlation between composition, defect density, strain and PL observed before and after thermal annealing.

5.3 Results and Discussion

To investigate these correlations as purported in the previous section, the experiments were organized into measurement classes and studied accordingly i) X-ray rocking

curve and reciprocal space maps of all samples ii) PL results of samples with different Sn compositions but same strain levels iii) PL results of samples with different strain levels but same Sn compositions. The results were analyzed for as-grown and annealed variants under 2,4 and 8-hour annealing treatments at 300^{o}C. Structural parameters like the composition, defect density and strain levels were extracted from the thoroughly analyzed results of the X-ray diffraction measurements while the optical information such as the PL intensities and peaks corresponding to the direct and indirect transitions were provided from the PL measurements. The behaviors of the extracted optical parameters are also analyzed against their corresponding annealing time.

Following proper analysis, it is observed that the i) energy separation between the indirect and the direct transitions is controlled predominantly by the composition and the strain states (level of strain) ii) both the threading/misfit dislocation defect densities and surface roughness are controlled by the level of strain. In addition to these revelations, it was also observed that all annealing-induced changes in energy separation between indirect and direct transition can result in an increased/enhanced PL emission while reductions/decrease in PL emission can attribute to changes in threading/misfit dislocation defect densities and surface roughness. Therefore, the impact of annealing on the optical properties (PL emission) is determined by the competition between factors identified above.

5.3.1 X-ray diffraction (XRD) measurements

XRD Rocking curves (RC) and reciprocal space maps (RSMs) measurements of the as-grown and annealed 'variants' of the select samples (S14, S15, S29 and S32) were taken to extract the Sn compositions, strain and the defect densities in the GeSn layers pre- and post-

annealing treatments. Figure 5.1 shows the XRD rocking curves (also known as the ω/2θ scans) of the samples showing the X-ray diffraction peaks of the Si, Ge, and GeSn (all symmetric 004 planes) in the order on their diminishing Bragg's angle, θ.

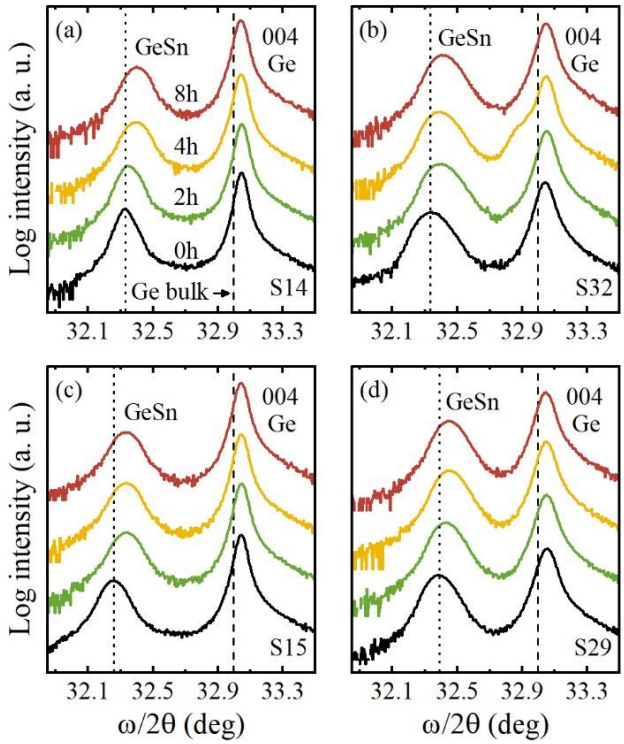

Figure 5.1. X-ray diffraction rocking curve (ω/2θ scans) of samples S14, S15, S29, and S32 showing little to no compositional change. The diffraction peak positions of the bulk Ge and as-grown GeSn layers are represented by the dashed and dotted lines respectively.

For all samples, the Ge peak is seen to shift to the right relative to the vertical dashed line representing the bulk position. This shift is indicative of a tensile strain of ~0.2% in the Ge buffer and corresponds to the residual strain value observed in typical Ge-on-Si epi-growths. This value is typically due to the difference in thermal expansion coefficient between Ge and Si [135]. The impact of the annealing treatment is seen in the peak position of the GeSn epilayer where they show a slight shift to the left indicating a diminished vertical lattice parameter, c.

This parameter is extracted from the diffraction peak position of the ω/2θ scan using the Bragg's relation below,

$$2d_{004} \sin\theta = n\lambda \qquad \text{(Equation 5.1)}$$

where $d_{004} = c/4$ is the separation between the (004) planes, $\lambda \approx 0.15406$ nm is the X-ray incident beam's wavelength, and n is the reflection order. The rocking curve images of all four samples show slight changes in the composition upon thermal subjections at 300°C, even after 8 hours. Figure 5.2 below shows the XRD scans of the samples S14 (a), S15 (b), S29 (c), and S32 (d). The respective FWHM extractions are also shown in Table 5.2.

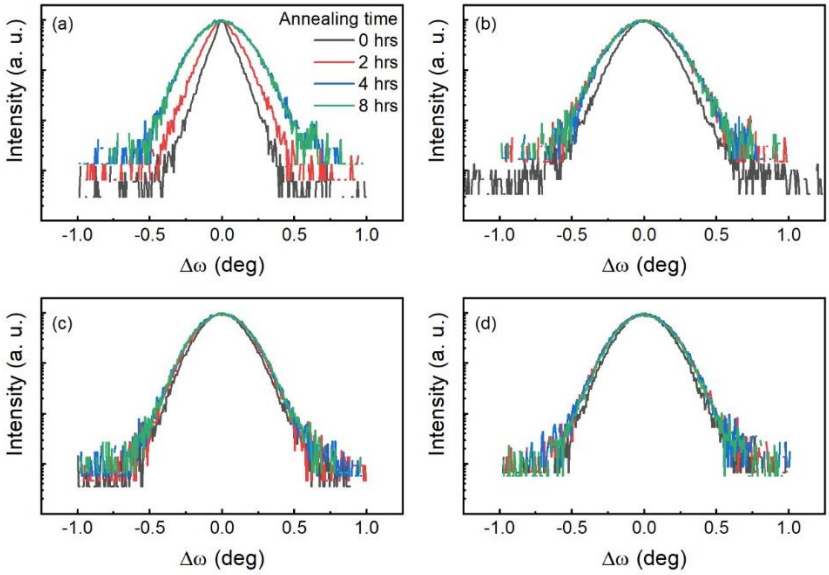

Figure 5.2. XRD ω scans of the samples (a) S14 (b) S15 (c) S29 and (d) S32.

Table 5.2. FWHM of the 004 ω scans for the GeSn layers of all four samples

Sample	FWHM (deg)			
	as-grown	annealed 2 hrs	annealed 4 hrs	annealed 8 hrs
S14	0.107	0.175	0.328	0.334
S15	0.282	0.383	0.379	0.388
S29	0.302	0.338	0.353	0.35
S32	0.331	0.366	0.368	0.363

Additional information regarding the nature of the as-grown samples and their evolution after annealing treatments are shown in the asymmetrical $\bar{2}\bar{2}4$ reflection of XRD reciprocal space maps (RSMs). The RSMs are shown in Figure 5.3 below:

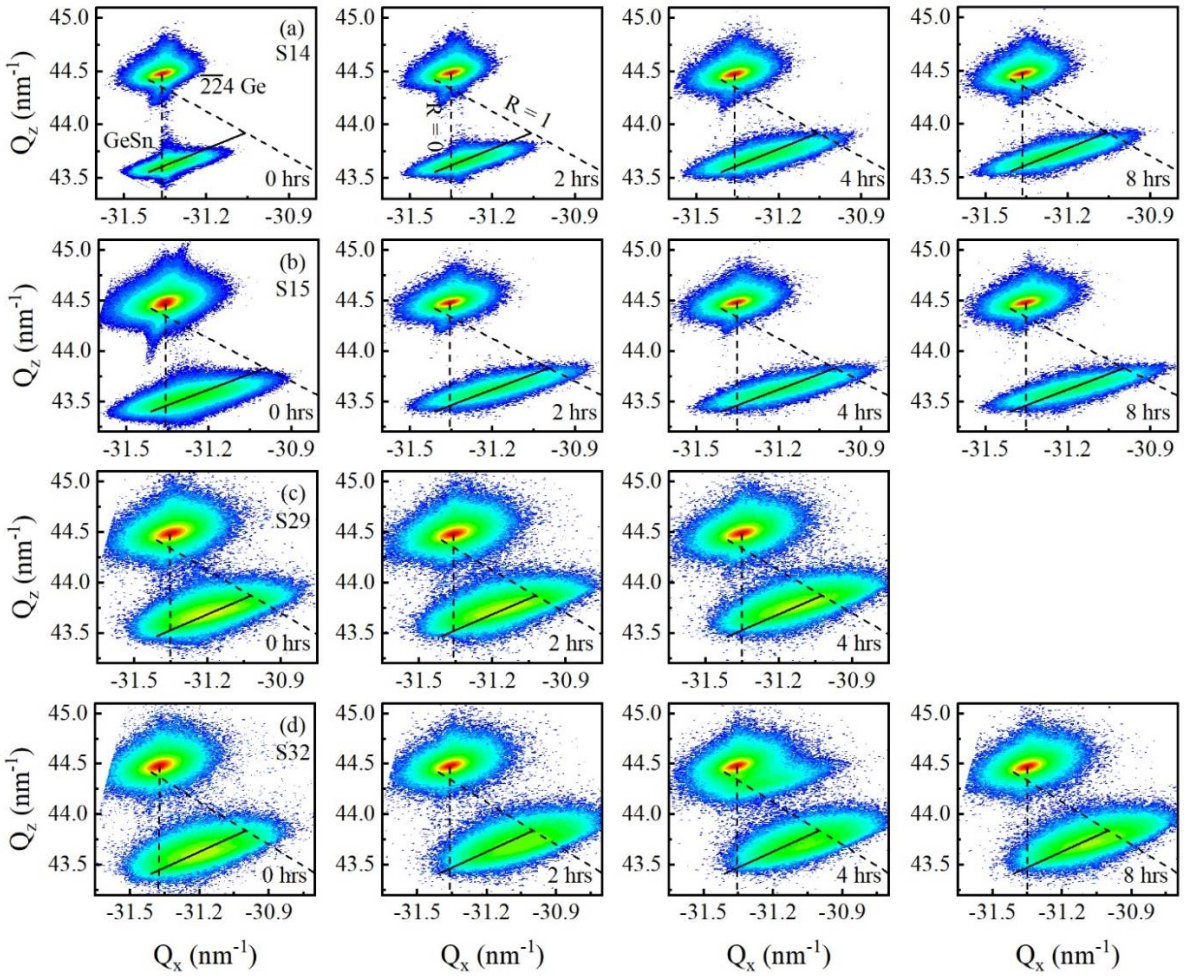

Figure 5.3. Reciprocal space maps (RSMs) of as-grown (0 hours) and annealed variants (2, 4 and 8 hours) of samples S14, S15, S29, and S32. Inclined and vertical dashed delineations on the contour plot represents fully relaxed and fully strained GeSn epilayer to the Ge buffer. The solid line also represents the GeSn layer's isocomposition line for each sample. [Copyright]

The measured reciprocal space map of the annealed samples shows a shift in the GeSn peak toward the R = 1 line indicating an increase in the strain relaxation which also represents a fully-strained relaxation.

This peak shift follows the solid line delineation (also known as the isocomposition line) implying that the GeSn epilayer shows little to no Sn compositional change upon annealing. This is an important point to note, since this same trend is observed in the RSMs of all the four samples. To calculate the Sn composition of all the samples, the lateral lattice parameter a, was first measured from the identified GeSn peak positions on the space maps in Figure 5.3 through the equation 5.2 below:

$$|Q| = \frac{2\pi}{d_{224}} = 2\pi\sqrt{\frac{8}{a^2} + \frac{16}{c^2}} \qquad \text{Equation 5.2}$$

Here, the diffraction vector is represented as Q, while the notation, d_{224} is the separation distance between the tetragonal lattice (224) planes. The strain level (or strain state) and the Sn composition of a biaxially strained GeSn epilayer is represented in equations 5.3 and 5.4 below:

$$\varepsilon_z = -2\frac{C_{12}}{C_{11}}\varepsilon_x \qquad \text{(Equation 5.3)}$$

$$a_0 = \frac{c + 2\dfrac{C_{12}}{C_{11}}}{1 - 2\dfrac{C_{12}}{C_{11}}} \qquad \text{(Equation 5.4)}$$

Here, C_{12} and C_{11} are the elastic constants while the notation a_0 represents the lattice parameter of GeSn material obtained by linearly interpolating the Sn and Ge parameters using the relation below, [136]

$$a_0 = xa_{sn} + (1-x)a_{Ge} \qquad \text{(Equation 5.5)}$$

To obtain the defect density and strain information, a combination of RSM information in Figure 5.4 coupled with some modelling efforts were computed for all as-grown and annealed variants of samples for S14, S15, S29, and S32 as shown below:

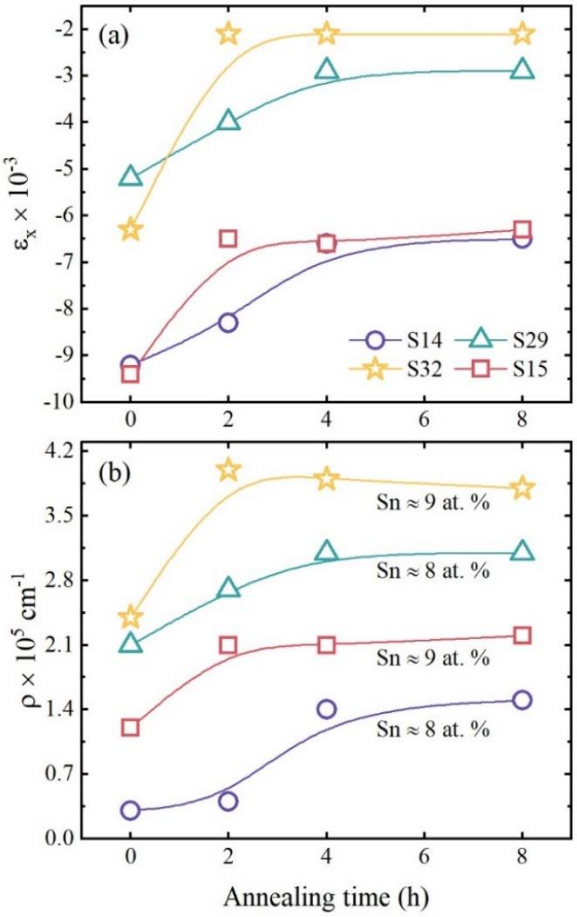

Figure 5. 4. (a) The strain, and (b) defect (misfit dislocation) density as a function of annealing times for all four samples

5.3.2 PL results of samples with different Sn compositions but similar strain levels

Photoluminescence spectra of samples S14, S15, S29 and S32 are shown in Figure 5.5 below. Although these samples are characterized by similar Sn composition in their as-grown states, their annealed PL behaviors after 2, 4 and 8 hours are significantly different. Based on

these, some factors must be taken into consideration when comparing the PL behaviors of these samples.

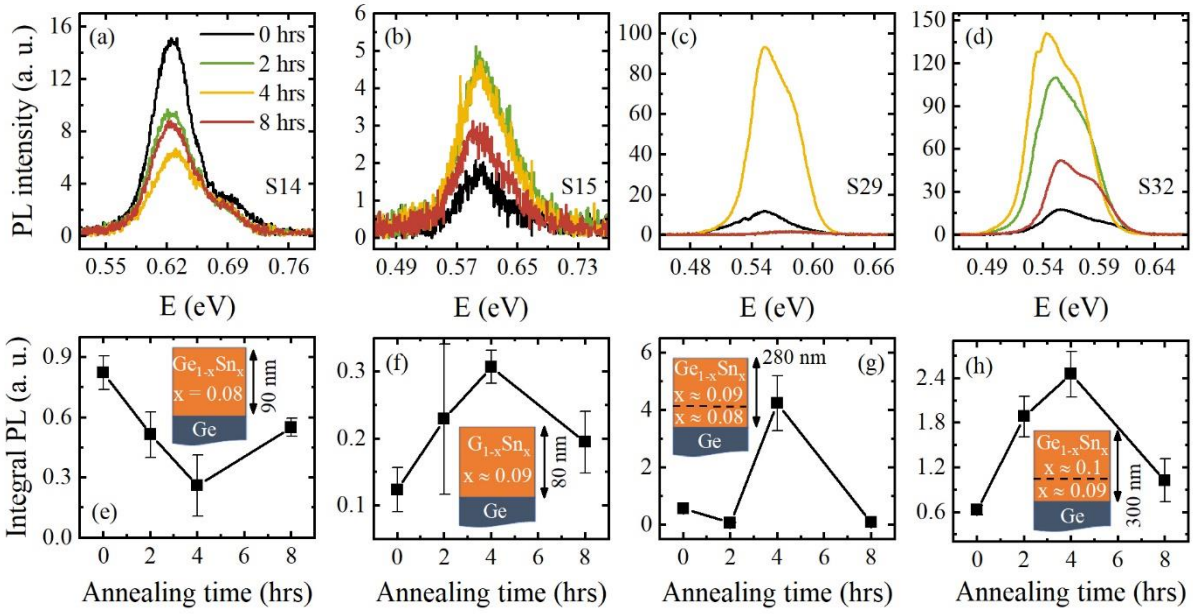

Figure 5.5. PL spectra of samples four samples as a function of their annealing times. Inset are the sample structures.

For instance, in their as-grown states, samples S14 (8% Sn) and S15 (9% Sn) are characterized by same levels of strain, however, during growth, their respective material evolutions are completely different. In fact, due its comparatively higher Sn content, sample S15 will possess a higher level of strain during growth and a relatively higher strain relaxation post-growth, at which point both samples (S14 and S15) now have matching levels of strain. Following this, it is it becomes easy to deduce that sample of S14 plays host to a higher dislocation density than sample S15 in their as-grown states as this deduction is consistent with the trend in Figure 5.3. Secondly, the competition between the energy separation (ΔE) of the two samples are different as it is expected that sample S15 has a smaller separation energy following its higher Sn composition compared to sample S14. The competition between the reduced energy

separation which increases PL intensity and a high dislocation density which decreases the PL stands to explain what happens to PL behavior during annealing. It is also noteworthy to mention that unlike changes in the dislocation density which are relatively linear, changes in the energy separation (ΔE) near the indirect to direct transition point is extremely non-linear. In addition to the separation energy and the defect density, another factor that must be taken into account are the optical losses due the sample's surface roughness. For instance, Figure 5.6 below shows the atomic force microscopy (AFM) images of all four samples.

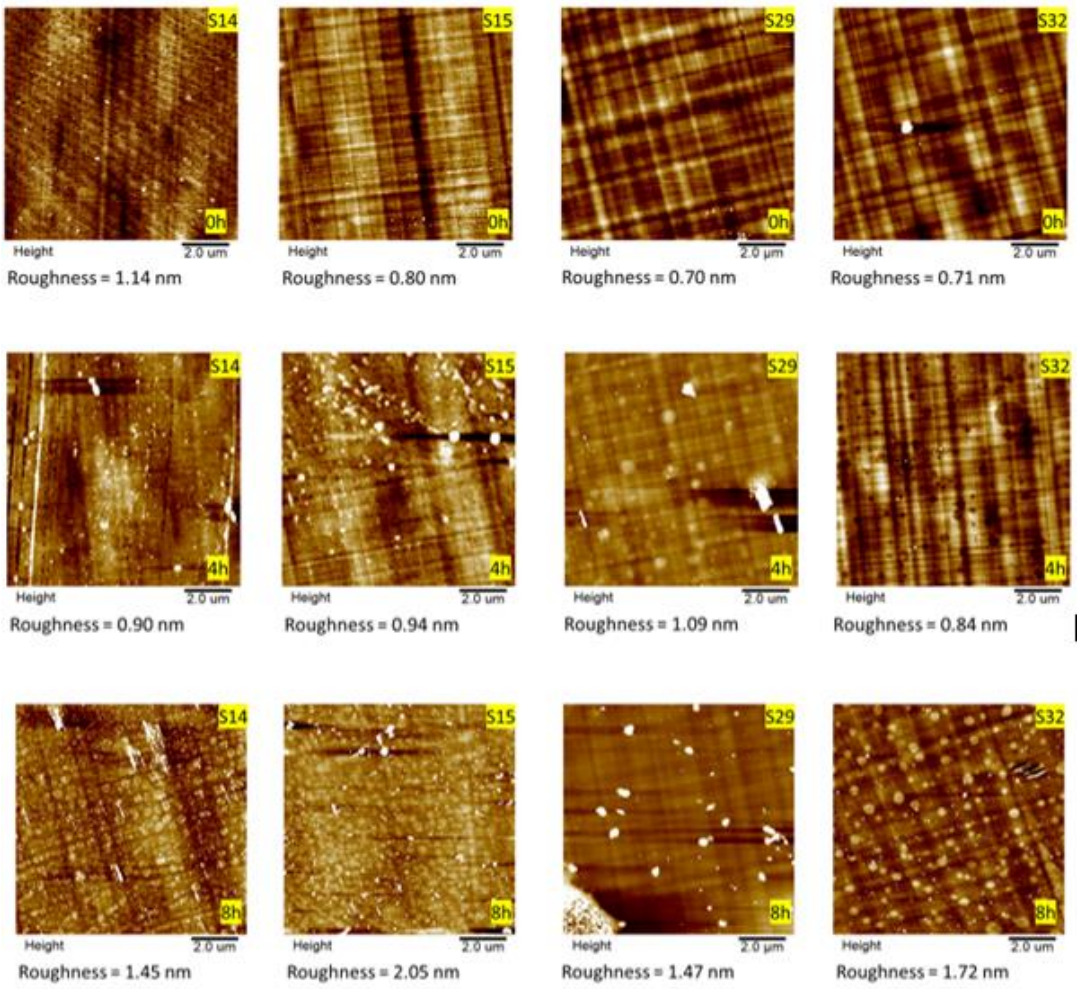

Figure 5.6. AFM images of all as-grown and annealed variants of samples S14, S15, S29, and S32

For all as-grown samples, the reported Root Mean Square (RMS) surface roughness is approximately 0.8 nm, and increases slightly to about 0.9 nm when samples are annealed to 4 hours. Furthermore, samples appear noticeably rougher after an annealing impact of 8 hours followed by an increased surface roughness of about 1.7 nm. As a consequence, the effect introduced by the optical scattering loss after 4 hours of annealing is smaller compared to an 8-hour annealed sample due to additional optical loss contributions from the more aggravated sample surface. As a result, a third factor, notably the surface roughness must be considered when comparing the impact of thermal annealing on the PL behavior of different samples. As a point of emphasis, the three factors are: i) the defect density ii) energy of separation (ΔE) and now, iii) the surface roughness.

The impact of annealing is further emphasized by looking at the PL results at different annealing times. Due to the linear increase in defect density in as-grown and annealed variants of S14 (specifically after 2 hours and 4 hours), the integrated PL intensity decreases sharply while impacting ΔE unfavorably. The defect density then levels-off after 4-hours of annealing as evidenced by the X-ray diffraction result. Conversely, the optical effect takes a positive turn after 8 hours of annealing to result in a slight increase in the PL that benefits significantly from the non-linear behavior of ΔE. As for as-grown sample S15, the defect density is comparatively higher than observed for as-grown sample S14 thus resulting in lower integrated PL intensity. In contrast, due to S15's higher Sn composition, the value of ΔE is much smaller. This makes the integrated PL far more sensitive to changes in ΔE than for as-grown sample S14 thereby resulting in an increase in the PL intensity upon annealing. After 2 hours of annealing, there appears to be an increase in strain which later levels off at 4 hours of annealing to result in a drop in integrated PL intensity after 4 hours; a phenomenon that can be explained by the increased

scattering loss originating from the surface roughness which increases from 0.9 nm at 4 hours to 2.1 nm after 4 hours or more specifically at 8 hours. These revelations are supported by the fact that, information extracted from the XRD and AFM data can provide leading information on the composition, defect density, strain changes and the surface roughness which certainly plays significant roles in explaining the effect of annealing at 300^{o}C on PL emission. Perhaps, these revelations can be less hypothetical and more quantifiable if the behavior of ΔE investigated and understood thoroughly. An attempt is made to balance these revelations.

For instance, samples S29 and S32, both have the same strain levels but dissimilar Sn compositions. Nonetheless, their outcomes differ in that samples S14 and S15 have relatively lesser compositions compared to S29 and S32. This evidence is strongly supported by the value of ΔE which is comparatively lesser for sample S29 and even much lesser for sample S32. Consequently, the PL for both samples linearly increase till about 4 hours when there is no further strain relaxation, after which the PL reduces following an increase in optical scattering that results from an exacerbated surface roughness.

5.3.3 PL results of samples with different strain levels but same Sn compositions

Analysis of the XRD data (Figure 5.4) shows increasing Sn composition and defect density for all four samples from S14 to S32. Nonetheless, as the transition point is being reached, the effect of small changes to ΔE, as well as the sensitivity of the PL to ΔE becomes increasingly much stronger. As mentioned earlier, to investigate this observation more closely, a thorough examination of ΔE for all four samples is required. This is accomplished by deconvolving the PL spectra into two separate Gaussian peaks to denote the indirect and direct optical transitions respectively. This would certainly help to: i) estimate the value of ΔE for

samples S14 and S32 and ii) to identify the direct optical peak transition by comparing the ratio of the PL intensity of the energy peak to the lower energy peak across the temperatures of investigation. For instance, if the higher energy peak is attributed to the direct transition, the ratio of the PL intensity will increase as a function of temperature, suggesting a transfer of carriers from the indirect L-valley to the direct Γ valley as the system reaches new equilibrium.

Based on this premise, the PL measurements of samples S14 and S32 were taken using both 532 nm continuous wave (CW) and 1064-nm pulsed lasers. Figure 5.7 shows the PL measurement of sample S14 using the 1064-nm pulsed laser to examine the entire GeSn epilayer while the 532 nm laser's penetration depth was limited to the top layer of sample S32.

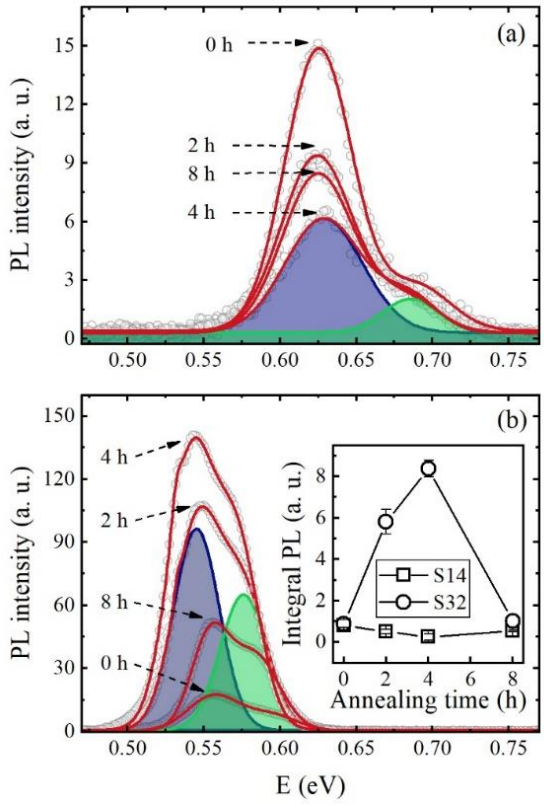

Figure 5.7. Pre- and post-annealing PL measurements of samples (a) S14 and (b) S15. Inset shows the integrated PL at different annealing times.

Note that the absorption co-efficient of the 532 nm excitation laser in Ge is about 5.58×10^5 cm^{-1} so that it reduces the intensity of the light penetration to about 36% which falls to about 18 nm below the surface of the sample [88]. For sample S32, this limits the PL contribution to just the top GeSn layer and neglects additional contribution from the bottom GeSn layer. Regardless, the same PL trend was realized using both excitation lasers, the only difference is that a higher integrated PL intensity is observed for the 532 nm laser. For the two samples, PL spectra were deconvolved and Gaussian-fitted into two separate but distinct peak that represents high and low energy peaks. The peaks were initially assumed to be respective indirect (E_{L-HH}) and indirect ($E_{\Gamma-HH}$) optical transitions, and later verified upon further analysis.

According to the XRD data, the change in the positions of the indirect and direct peaks for the two samples with annealing is predominantly caused by variations in the level of strain in the annealed GeSn layers, rather than changes in the Sn composition, which remained rather constant.

The behavior of the integrated PL intensity at different annealing times is shown for samples S14 and S32 in the inset image of Figure 5.7 (b). This trend needs to be understood in that it provides fundamental information about the sample's evolution as well as the identification of the appropriate optical transitions. For instance, sample S32 shows an interesting dramatic trend which can only be explained in terms of the separation energies (ΔE) of the direct and the indirect optical transitions, where $\Delta E = E_{L-HH} - E_{\Gamma-HH}$. Owing to a relaxed compressive strain in the GeSn epilayers of samples S14 and S15[137], ΔE will decrease as a function of increasing annealing time as clearly shown in Figure 5.8 (a). Since sample S32 contains more Sn than S14, ΔE is comparatively much smaller than S14 by 27 ± 2 meV and also has a larger direct bandgap. This is expectedly favored by the non-linear dependence of the PL

on ΔE which then leads to an efficient PL emission [138]. As evidence for an increase in carrier population in the Γ valley, Figure 6.6b shows a decreasing separation energy (ΔE) with a dramatic increase in the peak intensity ratio Γ^{HH}/L^{HH}. For example, for sample S14, the result of the enhanced integral PL in Figure 5.7 (b) corroborates the increased emission observed in the Γ-HH valley in Figure 5.8 (b).

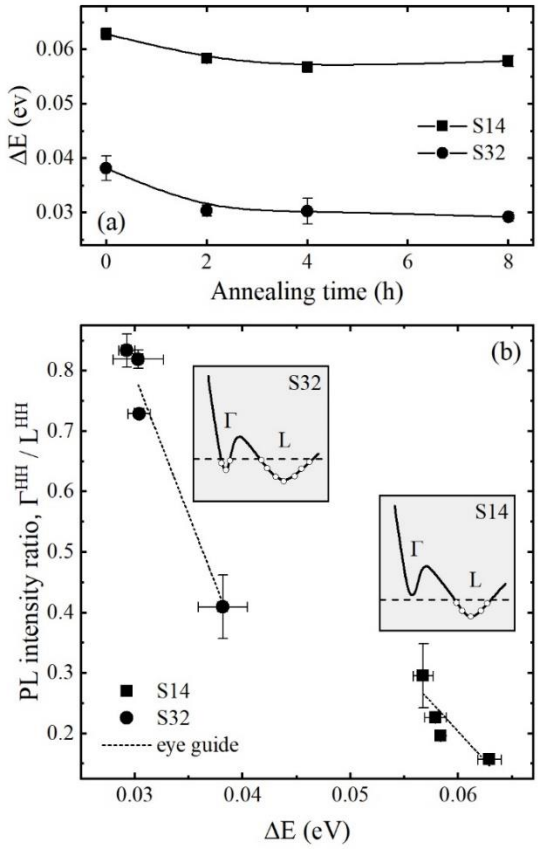

Figure 5.8. The energy separation (ΔE) and the PL peak intensity ratio Γ^{HH}/L^{HH} of samples S14 and S32.

To solidify our understanding, the peak PL intensities of the direct (Γ-HH) and indirect (L-HH) optical transitions were extracted from the temperature dependent PL measurements as shown in Figure 5.9. Both the direct and indirect peaks are red-shifted as the temperature

increases. This is a testament to the previously reported bandgap shrinkage in literatures [139,140]. Recall that these peak energies and intensities were extracted from deconvolved and Gaussian-fitted temperature-dependent PL spectra. It also noteworthy to mention that the Γ-HH and L-HH peaks were not resolved for temperatures higher than 200 K due to the PL plummeting PL intensities above this temperature.

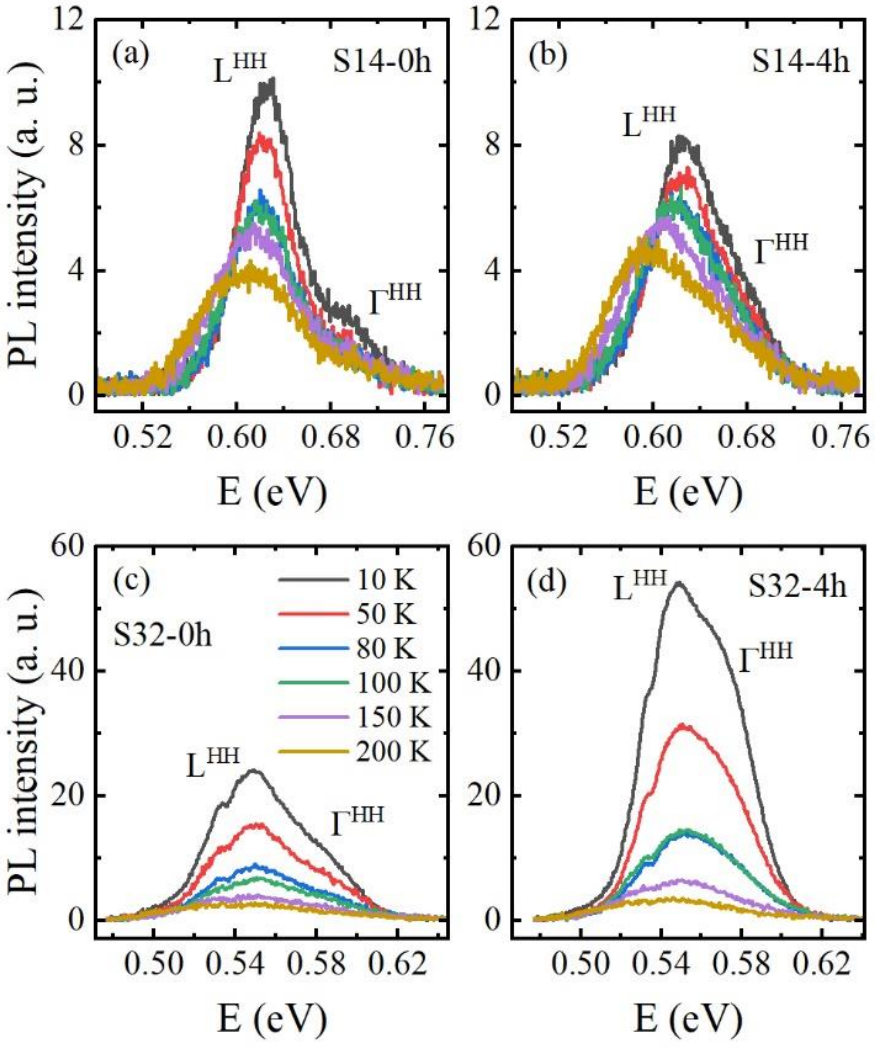

Figure 5.9. Temperature-dependent PL spectra of samples S14 and S32 [Copyright]

Figure 5.10 shows an increase in the PL intensity ratio with respect to temperatures for samples (S14 and S32) annealed for 4 hours. This supports the earlier assumption that higher energy peaks should correspond to direct optical transitions while the lower energy peak should also attribute directly to indirect transitions. This is true in this case even though irrespective of the fact that ΔE follows a decreasing trend for all four samples from S14 to S32.

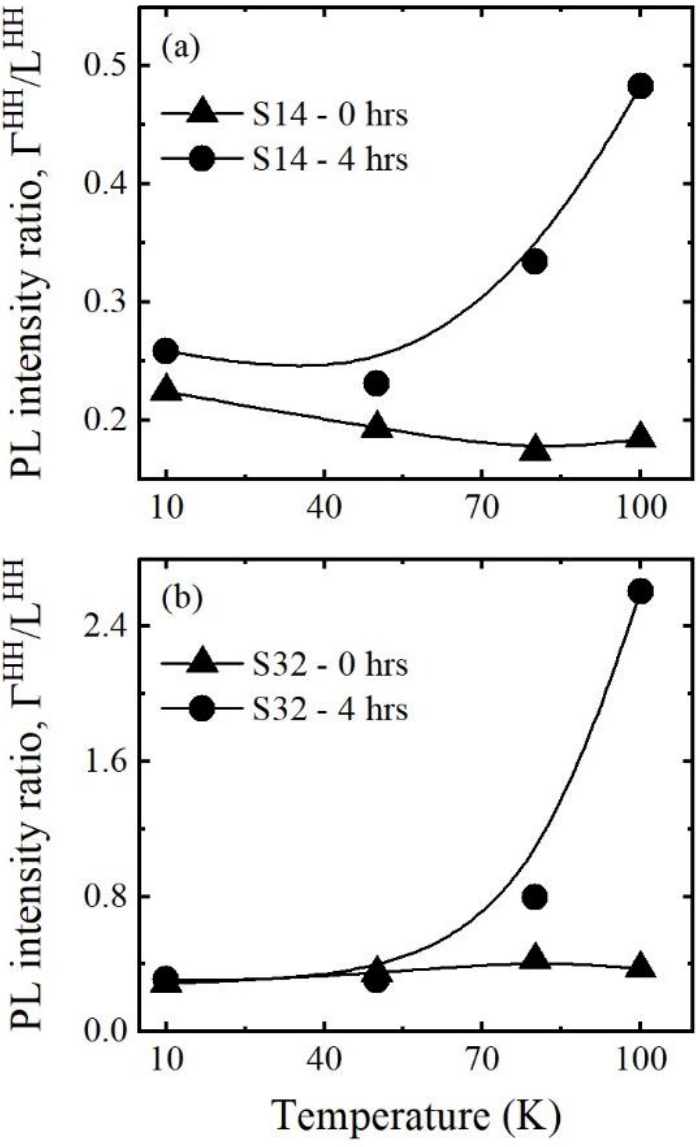

Figure 5.10. Ratio of the PL peak intensity as a function of temperature.

For a fuller grasp of the extracted parameters used in this study, a summary of the structural and optical characteristics is presented in table 5.3 below:

Table 5.3. Summarized GeSn parameters for as-grown and annealed samples.

Sample	Anneal time (hrs)	GeSn thickness (nm)	$\varepsilon_x \times 10^{-3}$	Sn content (at. %)	$\rho \times 10^5$ (cm^{-1})	Surface roughness (nm)	ΔE (eV)
S14	0	90	-9.2	8	0.3	1.14	62.92
	2		-8.3		0.4		58.37
	4		-6.6		1.4	0.90	56.77
	8		-6.5		1.5	1.45	57.92
S15	0	80	-9.4	9	1.2	0.80	-
	2		-6.5		2.1		-
	4		-6.6		2.1	94.00	-
	8		-6.3		2.2	2.05	-
S29	0	280	-5.2	8 for bottom GeSn region	2.1	0.70	-
	2		-4.0		2.7		-
	4		-2.9		3.1	1.09	-
	8		-2.9	9 for top GeSn region	3.1	1.47	-
S32	0	300	-6.3	9 for bottom GeSn region	2.4	0.71	38.16
	2		-2.1		4.0		30.40
	4		-2.1		3.9	0.84	30.30
	8		-2.1	10 for top GeSn region	3.8	1.72	29.24

Following deductive revelations from the study of both the structural and optical characteristics of samples S14 to S32, an additional sample, S45 (12% Sn), was added to further translate and/or extend our understanding to higher Sn composition and fully strained GeSn sample. Figure 5.11 below shows the pre- and post-annealing X-ray diffraction $\bar{2}\bar{2}4$ RSMs and ω/2θ scans of sample S45. Sample S45's fully strained structural expression is the outcome of its GeSn layer being at least 45 nm below the theoretical critical thickness to attain strain relaxation [39,141,142]. Due to this, this sample manifests as a lower defect density and higher strain level GeSn material compared to samples S14 and S32.

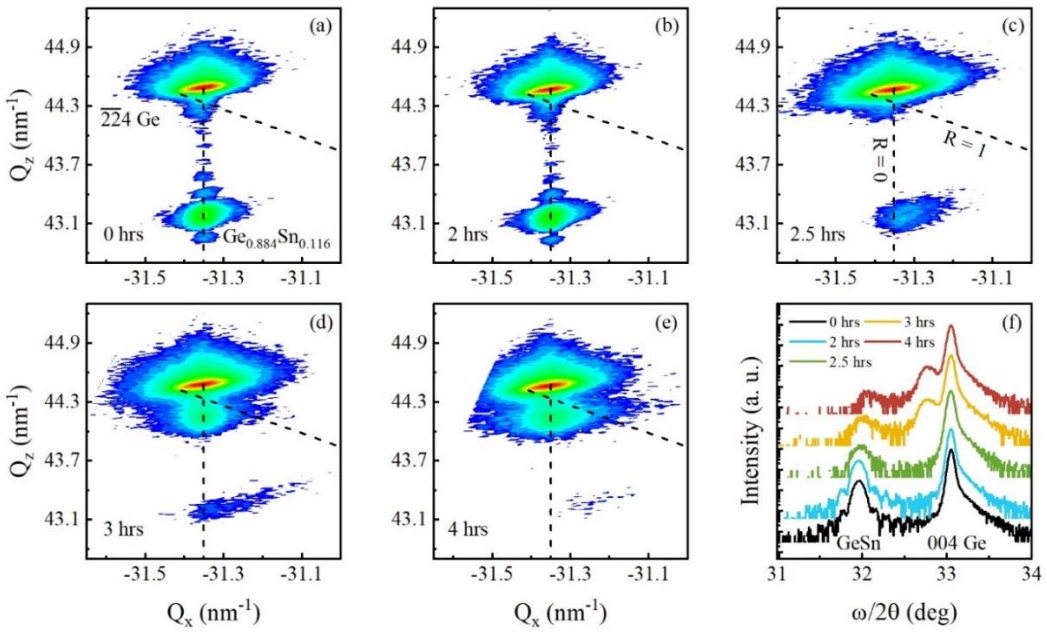

Figure 5.11. Pre- and post-annealing X-ray diffraction $\bar{2}\bar{2}4$ RSMs and ω/2θ scans of sample S45.

In fact, the sample is nearly void of defects (zero) in its as-grown state, and remains in same form (zero defect density) even after 2 hours of annealing treatment at 300°C. However, after about 2.5 hours of annealing, this value increases to nearly 0.5×10^5 cm^{-1} and later to strain relaxation effect, the defect density population doubles to about 1.0×10^5 cm^{-1} after 4 hours of curing (annealing). From a structural point of view, the sample maintains a strain of nearly -15×10^{-3} in its as-grown form while retaining its relaxed state even after 2 hours and 4 hours of annealing. This strain trend/nature also corresponds with a previous report on the investigation of direct bandgap optical transition of similar alloy composition ($Ge_{0.875}Sn_{0.125}$)[133]. From result of that study, the strain level observed for sample S45 manifests as an indirect bandgap material despite its high Sn composition. Meanwhile, the temperature-dependent PL spectra of sample S45 shows identifiable peaks corresponding to two pronounced optical transitions with a ΔE of approximately 120 meV (See Figure 5.12 (a) and (b)). Here, the peak emissions are assigned to L-HH and L-LH instead of the L-HH and Γ-LH transitions. Based on Figure 1 of our reference

literature [133], a strain level of about -15×10^{-3} should coincide with a ΔE of nearly 120 meV. Detailed analysis of sample S45 shows a higher possibility of relaxation occurring during growth for highly stressed GeSn.

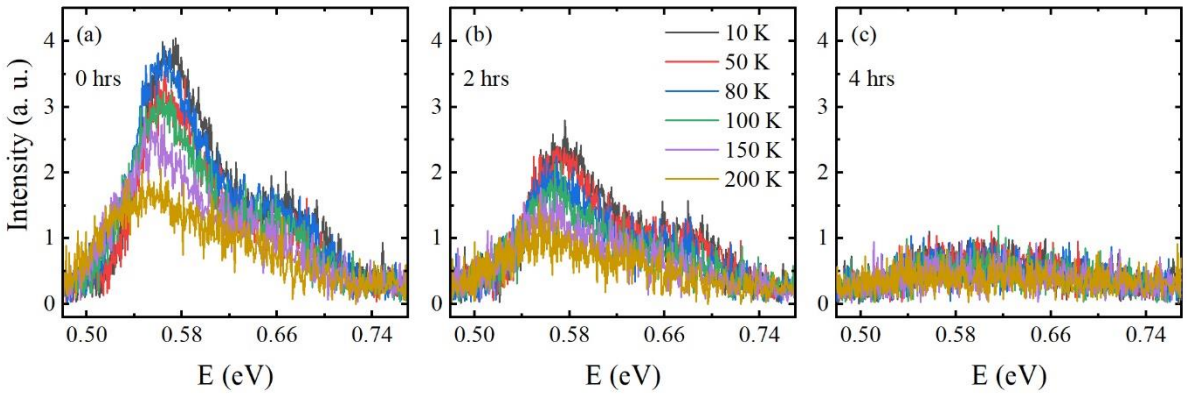

Figure 5.12. Temperature-dependent PL spectra of samples S45

5.4 Summary

In summary, connections have been established for the composition, defect density, strain and PL observed for the pre-and post-annealed GeSn alloys of Sn compositions near the indirect to direct optical transition points. The as-grown GeSn samples range between an Sn composition of 8% to 10%, and were annealed at a specific temperature of 300°C. The results reveal that for GeSn samples that fall near the indirect-to-direct transition point, the value of ΔE is strongly influenced by the strain level and the Sn composition while changes in strain level are controlled by the defect density populations (misfit/threading dislocations) as well as the observed surface roughness. While the role of annealing was to reduce the strain level, it's impact also decrease ΔE appreciably, which in turn increases the PL emission following pronounced competition between direct and indirect transitions.

Although annealing reduces the strain levels as previously emphasized, it also invasively affects the sample's quality by increasing the defect densities and the surface roughness– factors known to also reduce PL emissions. As a result, the impact of annealing on PL emission is determined by the competition between these parameters: i) change in defect density, ii) surface roughness and, iii) the separation energy between the direct and indirect transition, ΔE.

The effect of annealing on PL emission can either reduce or enhance the PL emission depending on the proximity of the alloy's Sn composition to the transition point where ΔE has been discovered to be extremely non-linear. This will mean that, depending on the sample's relative position to the transition point, an equal change in ΔE can have completely different effects, which can be large for one and small for the other. Of course, a different rule of thumb exists for GeSn samples with Sn compositions above the transition points where the PL emission manifests as a direct bandgap material.

Deductions from this study suggests that by growing an additional Ge capping layer on thee GeSn surface it is possible to curtail the impact of the surface roughness towards improved on the optical performance above room temperature.

Chapter 6: Investigation of Sn out-diffusion in GeSn/SiGeSn multiple quantum wells

6.1 Background

GeSn/SiGeSn alloys have sparked a great deal of interest in a variety of photonic and optoelectronics applications. Much of these realizations are piqued by a series of progressive research that led to the development of direct bandgap GeSn binary alloy materials for Sn compositions greater than 6% [11,85]. In fact, despite the solubility limitation of Sn in Ge, advances in material growth strategies and technologies have made it possible to develop GeSn materials with Sn contents that favor the transition of indirect to direct bandgap optical emissions [131,143–145]. While much research progress has been made to pioneer an array of device characteristics for bulk GeSn alloys [9,19,20,22,23,81,85], commensurate efforts towards advanced and improved applications are currently being pursued for GeSn quantum wells (QWs) [86–88,92,146]. A supplementary advantage of GeSn/SiGeSn QWs over bulk GeSn heterostructures is in their extensive viability at providing added structural material design and bandgap engineering options for a wide range of projected device applications. As a matter of fact, Type-I band alignment for GeSn/SiGeSn QWs has been made possible to favor a broad range of Sn compositions for improved carrier confinements[11] and enhanced radiative recombination in the QWs.

The past few years has ushered in novel growth strategies for multi-quantum wells (MQWs) architectures[11,51,88,89,91]; most of which have engendered an array of device applications as previously mentioned. For instance, Homewood et al.[11] used a multi-quantum well structure consisting of a combination of $Ge_{0.9}Sn_{0.1}$ well and $Si_{0.1}Ge_{0.75}Sn_{0.15}$ barrier to fabricate Si-based laser diode that operates in the mid-infrared. Higher modal gains were predicted for GeSn/SiGeSn QW lasers while a linear increase in optical confinement was

observed for increasing number of QWs. In similar fashion, Von den Driesch et al.[91] also reported improved lasing characteristics and enhanced optical and carrier confinements for GeSn/SiGeSn MQWs. In addition to the aforementioned works, a comparative study of SiGeSn/GeSn/SiGeSn MQWs was carried out by Margetis et al. [89] where a lower lasing threshold and increased operating temperature was reported for QWs with higher Sn composition and larger QW thicknesses. Despite these notable advancements, some issues regarding the material's thermal stability, Sn diffusion and intermixing, strain, strain relaxation, as well as their respective and/or collective effects of these on the optical emission characteristics of GeSn QWs remain particularly daunting from a material implementation perspective[134,147,148].

Additionally, while MQWs are projected to have superior optical emissions to single quantum wells (SQWs), the amount of light emitted rely invariably on a number of factors, such as the interface quality, degree of elemental diffusion and the material strain. As a matter of fact, thermal stability studies on high-Sn bulk GeSn materials[147,149,150] have suggested the possibility of high-Sn diffusion in GeSn MQW layers during growth, thereby resulting in the elemental fluctuations of alloy compositions, affectedly lower optical emissions and QW intermixing effect. Consequently, an experiment-based investigation that explores the effect of strain, strain relaxation and Sn diffusion on the optical properties of GeSn QWs is required.

In this study, we investigate the photoluminescence and structural properties of controlled sequence of SiGeSn/GeSn QWs with varying numbers of periods. Our findings show that the examined MQWs samples are coherently-strained with comparable defect densities. Further analysis revealed that elemental diffusion is more prominent during growth and is more predominant in MQW samples. This effect of this realization is made evident by demonstrated

blue-shift in the PL as the number of QW increases, followed by an increased line-width as well as a decrease in the absolute integrated PL.

6.2 Experimental Approach

Single and multi-quantum well samples are grown using an industry-standard reduced pressure chemical vapor deposition (RPCVD) machine. Si, Ge, GeSn and SiGeSn epilayer growths are realized using available commercial reactor gases such as SiH_4 for Si, GeH_4 for Ge, $SnCl_4$ for Sn and of course, a combination of the appropriate elemental mix of these to achieve specific binary (GeSn) or ternary (SiGeSn) alloy variants. Each sample consists of a 700 nm thick Ge buffer and a relaxed 600 nm thick $Ge_{0.918}Sn_{0.082}$ layer both grown sequentially to a Si (004) substrate. Above the Si-Ge-GeSn layers, are the QW layers which have different GeSn well and SiGeSn barrier alloy compositions for each investigated sample. The QW active regions comprise of a sequential period of SiGeSn bottom, GeSn well and SiGeSn top for SQWs and repeated periods of the same depending on the number of QWs ascribed to the sample under investigation. The schematic configurations of the samples are shown in Figure 6.1 below.

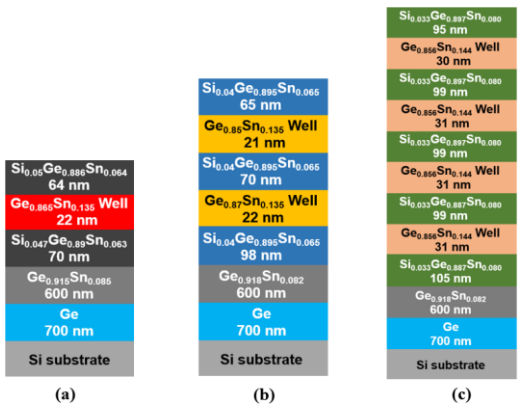

Figure 6.1. Schematic representation of all samples showing (a) 1-QW sample, S1 (Single QW) (b) 2-QW sample, S2 (Double QW) (c) 4-QW sample, S3 (Four QW)

Experimental-based structural analysis was carried out using a combination of X-ray diffraction (XRD) and Secondary Ion Mass Spectrometry (SIMS) methods. An integrated assembly of Philips X'pert MRD machine consisting of a 1.6 kW Cu Kα1 X-ray tube and a standardized Ge-bounce monochromator were utilized for measurements. The surface roughness of the samples was also examined using a Nanoscope IIIa Dimension 3000 atomic force microscope machine. The QW optical characteristics were investigated using an in-house standard off-axis PL multifunctional set up that integrates two (2) different excitation pumping lasers of wavelengths 532 nm (CW) and 1550 nm (CW). The setup also consists of the Horiba grating-based spectrometer (iHR320) that is easily attached to a PbS detector of 3 μm cut-off wavelength. The entire laser-detector arrangements are connected to a series of lens, mirrors lock-in amplifiers and choppers to enhance signal detection. The choice of the 1550 nm usage is motivated by the intention to explore the optical emission characteristics of at depths that penetrates the Ge and GeSn buffer layers at low loss (~10%). PL measurements were taken at considerably low excitation power of 10 mW and at low temperature of 10 K to optimize the PL signal.

6.3 Results and discussions

The quality of the GeSn/SiGeSn QW samples and strain levels were estimated using extracted data from the X-ray diffraction reciprocal space maps. All RSMs contours originate strictly from the $(\bar{2}\bar{2}4)$ asymmetric crystal planes as shown in Figure 6.2. All diffraction peaks for the Ge buffer, GeSn buffer, SiGeSn barriers and the GeSn wells are identified on the RSM plots and labelled accordingly. RSMs contour plots of samples S3 and S4 also show associated satellite fringes that originates from and around the GeSn/SiGeSn periods (Figure 6.2 (c)).

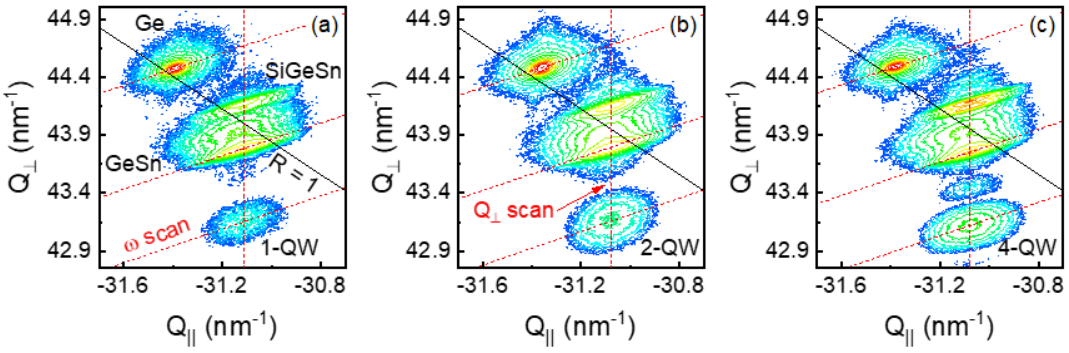

Figure 6.2. Reciprocal space maps (RSMs) of samples (a) S1, (b) S2, and (c) S3. Inclined and vertical dashed delineations represent the directions of ω and $Q_{\perp}$ scans in reciprocal space. The inclined solid line shows the estimated direction of relaxation.

The relation between the in-plane component of the diffraction vector, $Q_{||} = 2\pi\sqrt{8}/a_{||}$ and the in-plane lattice constant is used to calculate the strain, $\varepsilon_{||} = \left(a_{||} - a_0\right)/a_0$ associated with each layer. Here, a_0 is lattice parameter of unstrained bulk GeSn alloy material and is typically function of the Sn content. Both of which are estimated using the method explained in Ref [149]. The summarized structural parameters are shown in Table 6.1 below:

Table 6.1. XRD Parameters of the GeSn buffer, GeSn QW, and SiGeSn barrier layers

	Strain, $\times 10^{-2}$			Sn composition (at. %)	
	GeSn buffer	GeSn QW	SiGeSn	GeSn buffer	GeSn QW
S1	-0.27 ± 1.1	-1.13	0.22	7.7 ± 1.4	14.2
S2	-0.14 ± 1.0	-1.04	0.25	7.9 ± 1.1	14.4
S3	-0.18 ± 1.3	-1.08	0.20	8.2 ± 1.4	14.9

The calculated Ge buffer residual strain is the same for all the QW samples at (1.1 ± 0.5) $\times 10^{-3}$ and characteristic of typical Ge epitaxial growth on Si (100)[151,152]. On the other hand, strain relaxation in the GeSn buffer layer manifests during growth as regions of differing Sn compositions [43,153]. The GeSn buffer Sn composition varies from 6.8 ± 0.2 to 8.8 ± 0.2 at. %

for all samples leading to a ~1% Ge buffer-GeSn buffer lattice mismatch. As observed on the RSM contour plots, the positions of the GeSn peak are proximal to the R=1 relaxation line corresponding to a GeSn buffer residual strain of (- 8.8 ± 0.5) $\times 10^{-3}$ as well as a strain relaxation of 86 ± 4%. Additionally, the alignment of the GeSn/SiGeSn active layer and the GeSn buffer peaks through the vertical dashed lines indicates that the structures are coherently-strained to one other. The estimated strain in the SiGeSn barriers and the QW layers are 1.9 ± 0.5) $\times 10^{-3}$ and (- 1.1 ± 0.1) $\times 10^{-2}$, respectively. Figure 6.3 shows the XRD ω scans were measured along the $\bar{2}\bar{2}4$ reflection of the GeSn QW, GeSn buffer and the Ge buffer layers.

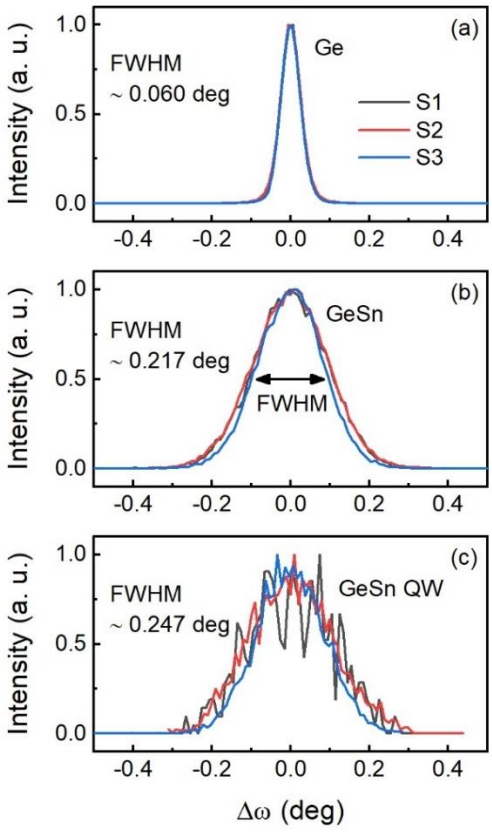

Figure 6.3. XRD ω scan of all samples measured along the $\bar{2}\bar{2}4$ reflection of the RSM contour plots for (a) Ge buffer, (b) GeSn buffer and, (c) GeSn well.

The line broadening information extracted from this data are then analyzed to study the quality of the layers in each sample. These are depicted as inclined dashed delineations on

the RSM contour plots shown in Figure 6.2. The quality of the respective layers are inferred from the full width at half maximum (FWHM) of the ω scan data. Extracted values of the FWHM are typical quantitative metrics for estimating the defect densities in lattice mismatched and strain-relaxed epitaxial systems. Although, the RSM contour plots in Figure 6.2 shows coherently strained GeSn/SiGeSn well-barriers heterostructure, defects propagating through the overlying layers above the Si substrates are characterized as threading dislocations[154]. Since non-radiative carrier recombination are bound to occur within the propagating threading dislocation (TDs), comparing and quantifying the TDs of each sample is necessary prior to examining their optical characteristics. Figure 6.3 (a) shows the extracted FWHM for the Ge buffer layer of each sample.

As seen in the figure, the maximum FWHM appear characteristically narrow at ≤ 0.060 degrees for each sample with comparative values showing little to no standard deviation that can be easily explained by the similar defect densities (TDs) and thicknesses of the Ge buffer layer in each sample. The plot of the XRD ω scans is also shown for the GeSn layers of all the samples in Figure 6.3 (b) where the FWHM is 0.517 degrees (at ~0.217 degrees) higher than the values extracted from the spectra of the Ge buffer layer. This dramatic increase in line-broadening ($\Delta\omega$) is due to the increase in misfit/TD defect populations that occurs during GeSn layer deposition, especially when the growth reaches the critical thickness needed for strain relaxation to occur [142]. It worth noting that the result of the non-varying FWHM peak values obtained for all the GeSn buffer spectra of all the samples is the similar GeSn buffer/Ge buffer lattice mismatch and Sn compositions in the GeSn buffer layers.

Figure 6.3 (c) also shows the fitted FWHM of the GeSn QW spectra at ~0.247 degrees and compares to the value obtained for the GeSn buffer. This implies that additional misfit/threading

defects were not formed during or after the deposition of the GeSn well/SiGeSn barrier growth. The collective significance of this observation is that the number of QW additions to a structure does not affect (increase or lower) the dislocation densities in the GeSn well. Figure 6.4 shows the X-ray diffraction $Q_{\perp}$ scans with GeSn QW line-broadening information which are extracted using the Gaussian fitting function. The $Q_{\perp}$ datapoints are scanned across the diffraction spots of the GeSn/SiGeSn active layers as delineated by the vertically dashed line through the RSMs contour patterns in Figure 6.2. The measured line-widths of the respective layers in Figure 6.4 are compared and analyzed accordingly.

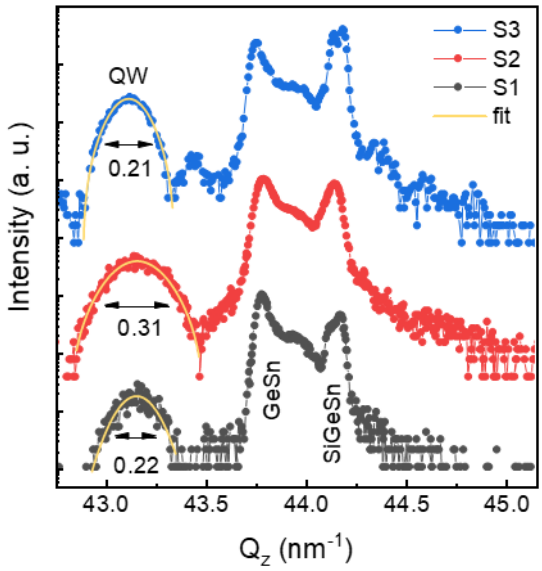

Figure 6.4. XRD Q_z scan of all samples measured along the $\bar{2}\bar{2}4$ reflection of the RSM contour plots of the GeSn/SiGeSn structure. The yellow line represents the Gaussian fit of GeSn QW peak.

In contrast with the ω scan measurements, the peak width values of the $Q_{\perp}$ are particularly influenced by a number of structural factors such as the strain/composition fluctuations, high dislocation densities, and limited coherent vertical thickness ($L_{\perp} = 2\pi/\Delta Q_{\perp}$). As observed in Figure 6.4, the two (S2) and the four (S4) QW samples show comparatively

higher QW peak widths compared to the single QW sample (S1). Since there are no additional dislocations/defects in the overlying coherently strained GeSn/SiGeSn active layers, the variations in the extracted $\Delta Q_{\perp}$ is hypothesized to be due to possible local strain or compositional limitations in the QW layers, and could be the first proof of possible QW intermixing within the layers. To validate the above hypothesis, secondary ion mass spectrometry (SIMS) measurements of each sample were performed to verify the elemental compositions of the respective layers. The resulting SIMS summaries of the all the samples are presented in Figure 6.5. From the plots, it is possible to deduce that the Sn compositions in the QW layers are decreasing with increasing sample depth below the top surface of the crystal structure.

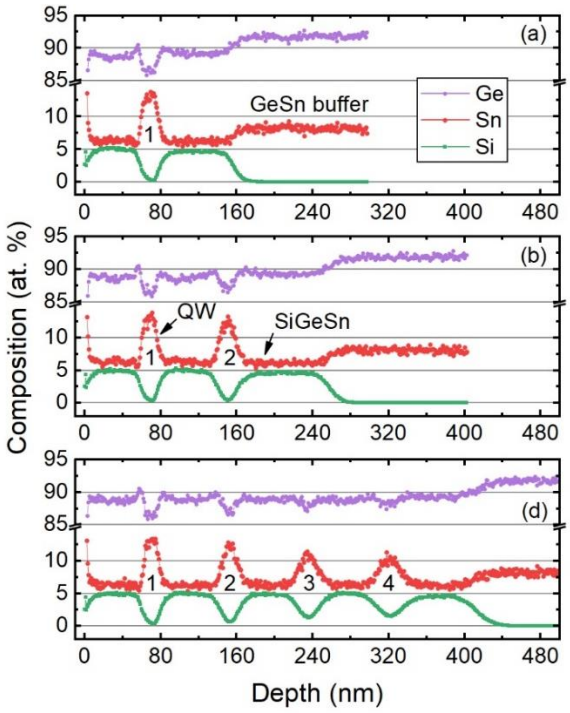

Figure 6.5. GeSn/SiGeSn QW SIMS profiles of samples (a) S1, (b) S2 and, (c) S3

For instance, while the single QW structure (S1) and the first QW in the double QW structure (S2) shows similar Sn composition of ~13.8 ± 0.1 at. %, the second QW in the double QW (S2) Sn composition shows a reduced/decreased Sn composition at ~13.1± 0.1 at. %. In the same vein, the Sn compositions of the third QWs in sample S3 also follows the same trend manifesting a reduction in Sn composition as a function of depth (by ~2.0 ± 0.2 at. %). As for the SiGeSn barrier observations, the Si composition in double QW (S1) is seen to increase by up to 0.7 ± 0.1 at. %, and also increasing by the same value in the third and fourth QWs of sample S3. In addition to the Si and Sn compositional variations, the GeSn/SiGeSn interface sharpness drops with increasing QW sample depth. The above identified observations both point to the possibility of interdiffusion events occurring in the deeper QW interfaces.

As a matter of fact, a visual evidence based on the shape of the Sn compositional profiles shows a noticeable geometrical transition from a compositionally graded Λ-shaped profile (from the first QW) to a nearly-blocked shape Sn profile (last QW). The layer configurations of the well-barrier crests and troughs in the SIMS profile are determined by the lattice strain in the GeSn/SiGeSn heterostructures [155]. The increased interdiffusion event at lower interfaces/depths is arguably due to extended longer term growth temperature at which these lowers layers were subjected. The key takeaways from this study are that intermixing are more prominent in deeper QW layers and are have been found to play a significant factor in MQWs growth strategies. Based on the trend observed on the SIMS profile, it is proper to consider the occurrence and role of intermixing for objectives that involve the growth of MQWs. For a fuller description of the Sn compositional behavior, $\widetilde{w}_{Sn}(z)$, within the respective QW layers, the SIMS profiles are fitted using the model described in reference [156]. The Sn compositional profile is described as follows:

$$\tilde{w}_{sn}(z) = \frac{w_{in}}{2}\left[erf\left(\frac{L_z + 2z}{4L_d}\right) + erf\left(\frac{L_z - 2z}{4L_d}\right)\right] \qquad \text{(Equation 7.1)}$$

where L_z is the thickness of the well, L_D is the Sn atom's diffusion length, and w_{in} is the initial molar fraction of Sn atoms in the QW. Figure 6.6 below shows the estimated Sn diffusion length as a function of QW depth for all the samples. Extractions from other MQWs are included to validate the results. From the plot, the Sn diffusion length (L_D) is observed to increase as a function of QW depth. This implies that less Sn contents are observed away from the surface, resulting in less sharp GeSn/ SiGeSn interface.

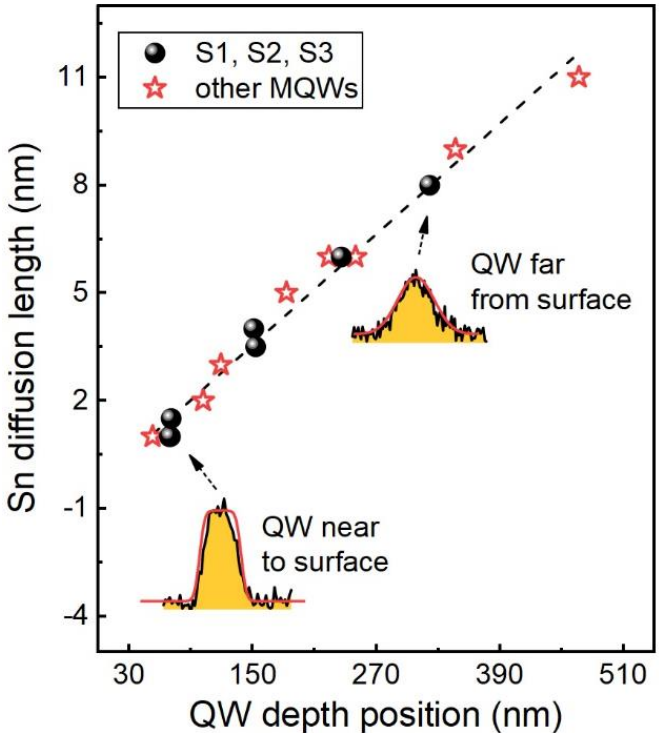

Figure 6.6. Estimated Sn diffusion length as a function of QW depth. Quantitative measure of the diffusion length is extracted from the fitted SIMS profile.

Before examining the impact of these diffusion events on the PL, specific attention is channeled towards exploring the effect of changes in surface roughness on the integrated PL

intensities of these QWs. Figure 6.7 below shows the AFM images of the QWs where the surface roughness of the quantum wells are compared accordingly.

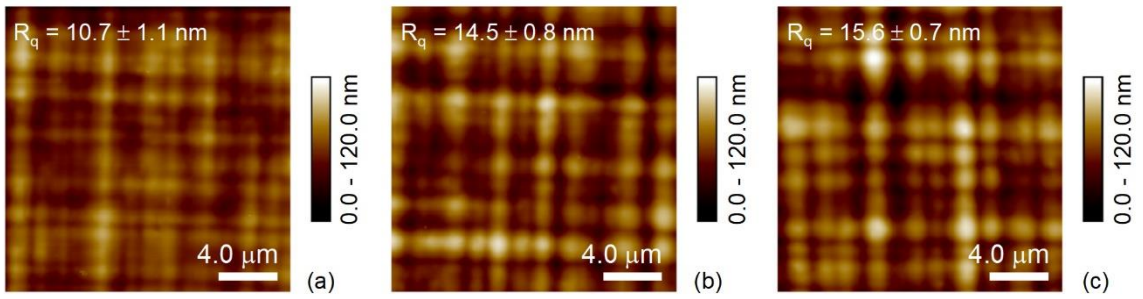

Figure 6.7. AFM images of samples (a) S1 (b) S2 and, (C) S3 showing the respective surface roughness values

The overall surface morphologies of the structures are characterized by patterned arrangement of ridges and troughs that occur as a result of the heteroepitaxial strain effects [155].

These patterns are somewhat responsible for root-mean-square surface roughness (R_q) value which increases from 10.7 ± 1.1 to 15.6 ± 0.7 nm as the total MQW depth increases through the structures. This linearly increasing surface roughness trend could potentially affect the overall collected PL of the QW samples and should be considered in further analysis.

In addition to these findings, this study also explores the effects of surface roughness, intermixing processes and Sn diffusion on the overall optical emission of the QW samples using 532 nm and 1550 excitation lasers. Figure 6.8 (a) – (d) shows the PL analysis based on the three samples.

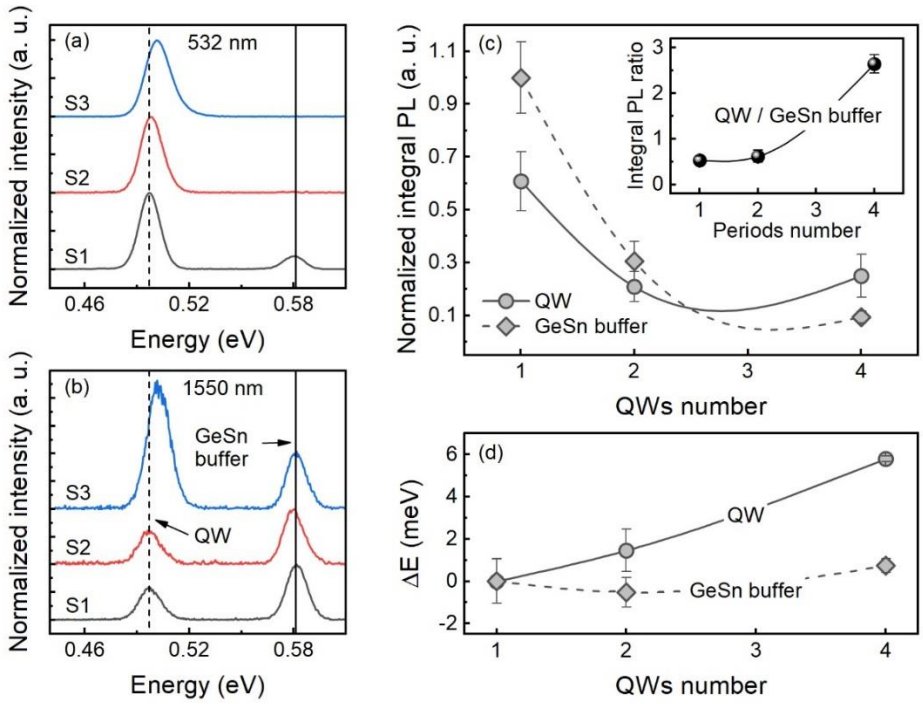

Figure 6.8. Measured PL spectra of samples S1, S2 and S3 at 10K using (a) 532 nm (b) 1550 nm excitation lasers. (c) Normalized PL from GeSn QWs and GeSn buffers versus QWs periods. Inset shows the integral QW/GeSn buffer PL ratios. (d) Energy difference of the QW ($E = E_{QW}$) and buffer ($E = E_b$) relative to sample S1 where $\Delta E = E - E_{S1}$.

Due to the non-uniform surface variabilities and differences in system calibrations through the experiment, PL measurements were taken at different spatial positions of the samples to account for possible incongruities. In Figure 6.8 (b), notice the appearance of distinct peaks at 0.55 eV and 0.58 eV when the 1550 nm wavelength laser is used.

Although, the occurrence of these two peaks are evident for the 1550 nm laser, the higher energy peak is absent in samples S2 and S3 when the 532 nm laser is used Figure 6.8 (a). This is due to its low penetration depth, compared to the 1550 nm laser which has a higher penetration power and can probe deeper into the QW structure. Based on the understanding of the QW structures and laser penetration depths, these low and high energy peaks are assigned to the GeSn QWs and GeSn buffer, respectively. In fact, due to the higher penetration depth of the 1550 nm

excitation laser, it is possible to observe PL from the GeSn QWs and GeSn buffer, especially the GeSn buffer which situates deeper below the overlying QW active regions. Using the PL from the GeSn buffer layer as a reference point for the single, double and four QW structures, it is possible to compare the PL behaviors of the samples accordingly. This idea is justified by the fact that the absorption coefficient is small ($\alpha \approx 10^4$ cm^{-1}) for bulk GeSn growths of similar Sn composition of ~ 14% [103,157,158], and absorption is also weaker for SiGeSn barriers with low Sn content. Considering that both the penetration depth of the 1550 nm laser and the ensuing PL intensity from the GeSn buffer may not be significantly altered, the PL from the GeSn buffer is considered a reliable reference parameter of choice for further comparative PL analysis.

Figure 6.8 (c) shows the normalized integral PL versus samples with different QW periods. The PL bevahior of both the QW and buffer shows quite an interesting trend in that, the integral PL decreases as the the number of QW increases. To provide a simpler interpretation of this behavior, the inset compares the integral QW/GeSn buffer ratio as a function of the QW samples. The result shows a higher PL ratio as a function of the increasing QW numbers which is somewhat a contradiction of what is known of the normalized integral PL as a function of QWs with different periods. In addition to these analysis, clear blueshift emissions based on relative comparison to sample S1, are observed for samples S2 and S3. This is shown is Figure 6.8 (d). Futhermore, the extracted spectral line-widths of the GeSn QW peaks is also observed to increase from 14.9 to 15.5 meV as the number of QW increases from one (S1) to four (S3) QWs. These PL blueshift occurrence as well as the spectral width broadening can be explained in terms of the intermixing events observed on the elemental depth profiles in Figures 6.5.

To provide an explanation for the decrease in integral PL as a function of increasing QW numbers, a mathematical connection is drawn between the surface morphology and the ensuing

optical character of the of the QW structures. This is realized by estimating the ratio of the secular light reflection to the total light reflection (which is also known as the total integrated scatter, TIS) as expressed in reference [159]. This is shown in the expression below,

$$TIS = \exp\left(-\left(\frac{4\pi R_q}{\lambda}\right)^2\right) \qquad \text{(Equation 7.2)}$$

where λ is the QW emission wavelength (2480 nm), R_q has earlier been established as the root-mean-square surface roughness. Based on the value of R_q value increasing from 10.7 ± 1.1 to 15.6 ± 0.7 nm, the calculated TIS will vary from 99.7 to 99.3%. Additionally, high resolution microscope images of the QW samples were taken (not shown) and indications of Sn segregation were not observed for all sample surfaces. This attests to the fact that the effect of the surface morphology of the samples on the PL is minor, if at all it has any bearing on the optical properties.

Based on these realizations, it becomes straightforward to hypothesize that the reason for the PL blueshift, spectral width broadening as well as the decreasing absolute PL intensity may of course be connected to Si/Sn intermixing events occurring at depths below the QW's surface. The occurrence of these intermixing events may give rise to the formation of localized defects masquerading as non-radiative centers within the structure. Of course, the advent of the localized features may not necessarily increase the overall defect density of the sample. These non-radiative centers may explain the observed spectral broadening, PL reduction as well as the spatial variations of measured PL across the sample surface. Further structural and optical characterization in the expressions of transmission and micro-Raman spectroscopy may provide insights into these occurrences.

6.4 Conclusions

This work provides an experimental account of the impact of QW intermixing on the PL emission of GeSn/SiGeSn multi-quantum well samples of different periods. While the measured PL increases as a function of increasing number of QW periods, a decline in the interface sharpness at larger depths is observed for higher period QWs. This decline is attributed to the effect of Si/Sn intermixing observed when the samples are subjected to longer-term growth temperatures. The effect of the Si/Sn diffusion also manifests optically as evidences of blueshift, spectral broadening and decreasing absolute intensity in the PL spectra. Expectedly, these intermixing and diffusion events can be pronounced for situations where higher growth temperatures are applied or for objectives with post-growth annealing requirements. Therefore, more attention should be devoted to the possibility of intermixing events during the growth of GeSn QWs.

Chapter 7: Si and GeSn Epitaxy

7.1 Background

7.1.1. Low Temperature Si Growth

The creation of abrupt doping profiles in MOSFETs [160] and thin film solar devices have been enabled by the epitaxial growth of Si at low temperatures [161]. On a grand scale, the possibility of these growths has served the strategy of eliminating autodoping tendencies of bare Si substrates and have ushered the use of seeded glass substrates as potential alternatives for a few notable applications [162]. In fact, the realization of low temperature growth is essential for MOSFETs applications in that higher than 400^{o}C growth temperatures are more likely to alter the doping profile of the device. The advantage of this pursuit also favors the affordability of current and future solar cell systems embracing the fuller actualization of a clean, affordable and green energy future. It is noteworthy to mention that growing at higher temperature result in a higher Si deposition growth rate while also affecting the quality of the films. The development of a working strategy that reduces the growth temperature while exploring a better understanding of Si growth mechanism is needed to circumvent these challenges. The low temperature objective is achieved by pursuing low-plasma density approach through a plasma-assisted UHCVD growth methodology while the high growth rate practicality will be explored by varying the hydrogen-silane dilution ratios [162].

Pioneering Si deposition techniques pursued this objective by pyrolytically decomposing Si precursors in a highly-hydrogenated sub-atmospheric pressure environment and at a high growth temperature (800 – 1200^{o}C) [163]. The idea to heavily hydrogenate the system stemmed from a preventive strategy to protect the wafer surface from oxidation. From an application point of view, these high temperature growth alternatives give rise to affected nanoscale thicknesses,

indistinct doping profiles as well as a high thermal budget; all of which are undesirable for CMOS processes since they affect device performance. Conversely, the growth of Si under low temperature conditions are affectedly trammeled by a reduced growth quality and low deposition rates that spur from two major factors. The first being the reduced Si adatom diffusivities about a hydrogen-terminated Si substrate while the second relates directly to the slow dissociation of precursor gases during deposition. Additionally, since oxidized silicon surfaces are hardly desorbed during low temperature interventions, the growth products result in defectively low quality films [164].

The oxygen desorption challenge is circumvented by introducing a specialized pre-deposition procedure that rids-off the oxidized patterns on the silicon surface and replaces it with hydrogen atoms to result in a hydrogen-terminated wafer surface. To create optimal conditions for high quality growths, the requirement of an advanced deposition technology that sponsor significantly lower water and oxygen partial pressures is needed. This objective has led to the development of a highly-functional ultra-high CVD system that can accommodate lower temperature epitaxial growths at ~ 600^{o}C. Due to the significantly low-pressure functionality of the system, low in-situ partial pressure objectives are possible since they give rise to an appreciably lower contaminants measure in the order of parts-per-billions. This creates an ideal environment for higher quality growths. Defined by their respective operating pressures, there exists three major deposition systems; these range from the UHVCVD system (less than 10^{-8} torr) to the atmospheric and sub-atmospheric types that operates within pressure ratings of several torrs. While the low temperature objectives hold promise especially within the framework of the plasma-assisted technology, the call to increase the growth rate of Si depositions perhaps needs to be critically explored. Previous attempts to address this issue

proposed the intervention of low-plasma density growths, in addition to increasing the hydrogen-silane ratio. These suggestions will be explored using the works of Mosleh et. al., as a reference point [162].

More recent growth advances have utilized plasma-assisted technologies to deposit amorphous, microcrystalline and crystalline growth samples[165,166]. Plasma-activation under admixed silane and hydrogen gases typically give rise to growth-favorable combinations of reactive radicals and atomic hydrogen that increases both the Si adatoms/hydrogen surface mobilities and diffusivities[167,168]. Increasing the Si adatom's diffusion lengths and hydrogen mobilities are the dominant factors responsible for the suitable transport of Si adatoms to their energetically-favorable crystalline sites. Achieving epitaxial crystalline growth is also favored to the application of low power plasma since higher plasma energies (15 -20 eV) have been proven to results in defected and or damaged growths[168].

7.1.2. Si-on-Si Growth Mechanism

The process schematics below shows the entire Si homoepitaxial deposition (Figure 7.1). Although, this work demonstrates the possibility of growing crystalline/amorphous Si-on-Ge using our in-house designed UHV-CVD system, a cursory overview of the Si-on-Si epitaxial process is presented for a clearer understanding of Si's growth dynamics in dissimilar lattice conditions where different elements or alloys are involved – Heteroepitaxial scenarios. ① The process starts with bare Si wafers that play host to Si-Si dangling bonds. Upon exposure to air, these unattended dangling bonds are promptly attached to oxygen atoms in air thus forming SiO_2 patterns across the entire wafer surfaces. ② Since the layered-formation of silicon dioxide (SiO_2) would be inimical to the growths, the wafers are treated to a hydrogen-passivation process that eliminates the native oxides and also initiate new bond associations with hydrogen to result

in hydrogen-terminated Si surfaces. The passivation procedure takes oxide-exposed Si wafers, subjects it to a standard RCA-1/RCA-2 cleaning procedure, then immerses same in a bath of hydrofluoric acid (HF) after which the wafers are dried-off by a typical in-lab nozzle-channeled nitrogen gas [169].

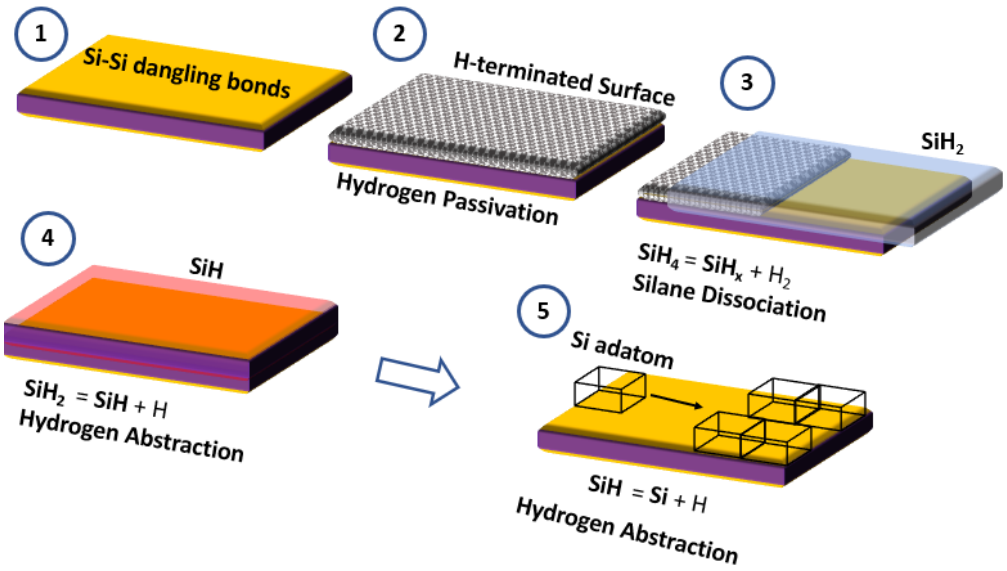

Figure 7.1. Si homoepitaxial growth mechanism

③ Following these pre-deposition steps, the hydrogen-terminated wafers are then transported to the UHVCVD's process chamber where appropriate growth parameters such as the temperature, pressure, gas flow rates, plasma power and the Si/H_2 dilution ratio are applied. The growth is initiated through a controlled supply of silane gas (the precursor gas of Si) which, when favored to the appropriate growth conditions, breaks down or dissociates into familial product forms of reactive radicals and atomic hydrogen as indicated in process ③. The dissociation reaction's release of the atomic hydrogen aids the deposition scheme in diverse ways. First, it triggers the cessation of the erstwhile surface hydrogen termination, then improves the mobility of the

hydrogen whilst enhancing Si-adatoms diffusivity on the wafer surface. ④ As the growth temperature becomes less than 407°C, the dissociation chemistry favors the formation of a dihydride product which in turn decelerates the motion of Si adatoms by shortening their diffusion lengths. The silane dissociation event is arguably the most important chemistry in the deposition process, in that it aids the reduction of the growth temperature – a notable objective in the low temperature epitaxy pursuit [170]. Additionally, this dissociation event is also responsible for inducing the hydrogen abstraction process – a hydrogen removal strategy that sponsored the transitory formation of a monohydride from an initially formed dihydride. ⑤ The hydrogen abstraction process continues to strip more hydrogen atoms away from intervening dihydrides and or trihydrides until free Si adatoms are completely divorced from their parent atoms to be appropriately situated in their respective crystalline sites. It should be clearly stated that the advent of the hydrogen atom served to improve the Si adatom's diffusivity while also acting as selective etchant stripping away Si-Si amorphous associations as well as possible defective growth features [162].

A team of researchers in the early 2000s investigated the abstraction process under low temperature trials and realized that for the silicon atoms to effectively move about the Si surface, the H_2/SiH_4 dilution ratio had to be greater than 10 [171]. Otherwise, the surface diffusion length turns out to be significantly lower thereby affecting the diffusion length as well as the surface motility of the Si ad-species. Variable dilution ratios are investigated in this chapter with the aim to realize low temperature growth and comparatively higher growth rate depositions.

7.2 Low temperature Si-on-Ge growth using the Plasma-enhanced UHVCVD

This section details the growth and characterization parts of this work. Although, the growth mechanism of a typical Si-on-Si homoepitaxial objective have been presented, a more interesting problem regarding the heteroepitaxial growth of same Si on Ge is explored. While the applications of Si-on-Si are vast and varied over the developments of MOSFETs and thin film solar cells, the application of Si heteroepitaxy to dissimilar systems such as Ge or transition metal oxides (TMOs), especially TMOs that have potential expressions for the creation electronic systems that carry semiconducting, magnetic, superconducting and ferroelectric properties. Since our in-house plasma has been utilized for low temperature growths under 300^{o}C, it becomes imperative to grow thin Si layers using Ge as an example, then carrying the lessons learnt to apply to TMOs for future research ambitions (Semiconductor-on-Insulator application). Growing thin film (3-40 nm) Si is important for TMOs since these thicknesses are below the critical thicknesses of TMOs. It is also believed that low temperature accounts may help prevent the formation of SiO_2 along the growth interface. The undesirable formation of this oxide layer could obtrusively hinder the realization of a sharp interface – a critical feature responsible for Si-TMO application potential. This work will not be discussed here. An overarching objective of this effort, especially as it pertains directly to Si-on-Ge growth is the question of whether it is possible to achieve crystalline growths at low temperatures (200-300^{o}C). The growth of amorphous Si at these temperatures have been achieved in the past, but the realization of crystalline phase growth of Si on Ge has been less researched. This work uses plasma-powered UHV-CVD technology and an understanding of the competition between plasma power, growth time and H2/SiH4 dilution ratio to achieve low temperature crystalline Si-on-Ge layered growths (Frank-Merwe growth mode) with little to no surface Si islands occurrences (Volmer-Weber or Stransky-Krastanov growth modes).

This preliminary heteroepitaxial account chronicles the experimental expression of demonstrated Si-on-Ge growth as well as an understanding of Si's growth mechanisms. Learnings from this exploration can be translated to other heteroepitaxial signatures where Si is the overlying depositional element.

7.2.1 Growth Approach

Four-inch Si wafers were cleaned using the standard piranha-etch and HF dip procedure before thin film deposition in a process chamber. As previously mentioned, these growths are achieved in a plasma-enhanced system UHV-CVD system using appropriate gas precursors. Where Si and Ge films are deposited, SiH_4 and GeH_4 are used as respective precursors both of which are enabled by hydrogen carrier gas. The plasma-enhanced UHVCD chamber is maintained at a base pressure of 10^{-9} torr throughout the growth. Figure 7.2 shows the representative heterostructure schematics for this experiment. The generalized growth conditions are also embedded for visual simplicity.

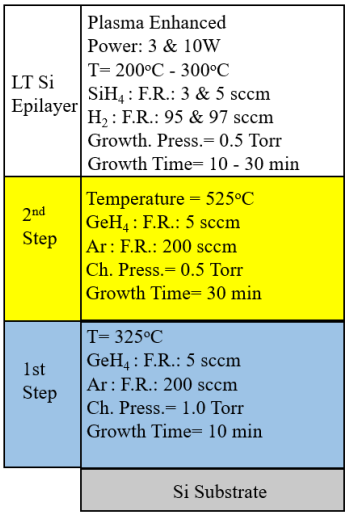

Figure 7.2. Representative heterostructure schematics of the Si-on-Ge growth. The generalized growth conditions are also presented.

The Si-on-Ge heteroepitaxial growth steps are presented accordingly. The growth starts with the deposition of a Ge buffer film that consists of an initial Ge film layer at low temperature (375^{o}C) followed by a high temperature growth (575 ^{o}C) of a second layer. The initial low temperature Ge growth was deposited to avoid possible island growth while the second layer prompted the deposition of a higher quality layer. Table 7.1 shows an extended detail of the Si-on-Ge growth conditions.

Table 7.1. Extended details of the Si-on-Ge growth conditions

	Temp.	Time	Flow rate		Dilution ratio (DR)	Plasma Power	Thickness
Sample	(°C)	(min.)	H_2 (sccm)	SiH_4 (sccm)	H_2/SiH_4	(W)	(nm)
A	250	30	97	3	32	3	193
B	300	15	95	5	19	10	37
C	200	10	95	5	19	3	10
D	250	10	95	5	19	10	97

7.3 Characterization Methods

The post-growth characterization analysis was carried out to explore the impact of the growth parameters on the sample's structural and optical quality. To inspect their respective film thicknesses, ellipsometry data was obtained at a constant angle of 70^{o} using the J.A. Woollam V-Vase ellipsometry system. Further optical investigations were performed where the use of the Raman spectroscopic set-up was used to investigate the degree of crystallinity of the grown samples. The Raman assembly employed a 632 nm He-Ne excitation laser to probe respective film's strain and bonding states. In addition to the optical evaluations, the structural characteristics of the films were also investigated to provide further information on the film's crystallinity. Atomic force microscopy (Nanoscope IIIa scanning probe microscope (Dimension

3000)) was also used to inspect the surface morphology, roughness and growth uniformities of the grown samples.

7.3.1 Raman Spectroscopy

Raman measurements were obtained to inspect the crystalline or micro-crystalline natures of the grown samples. Figure 7.3 (a) – (d) shows the Raman data (intensity vs. Raman shifts) obtained for samples A to D.

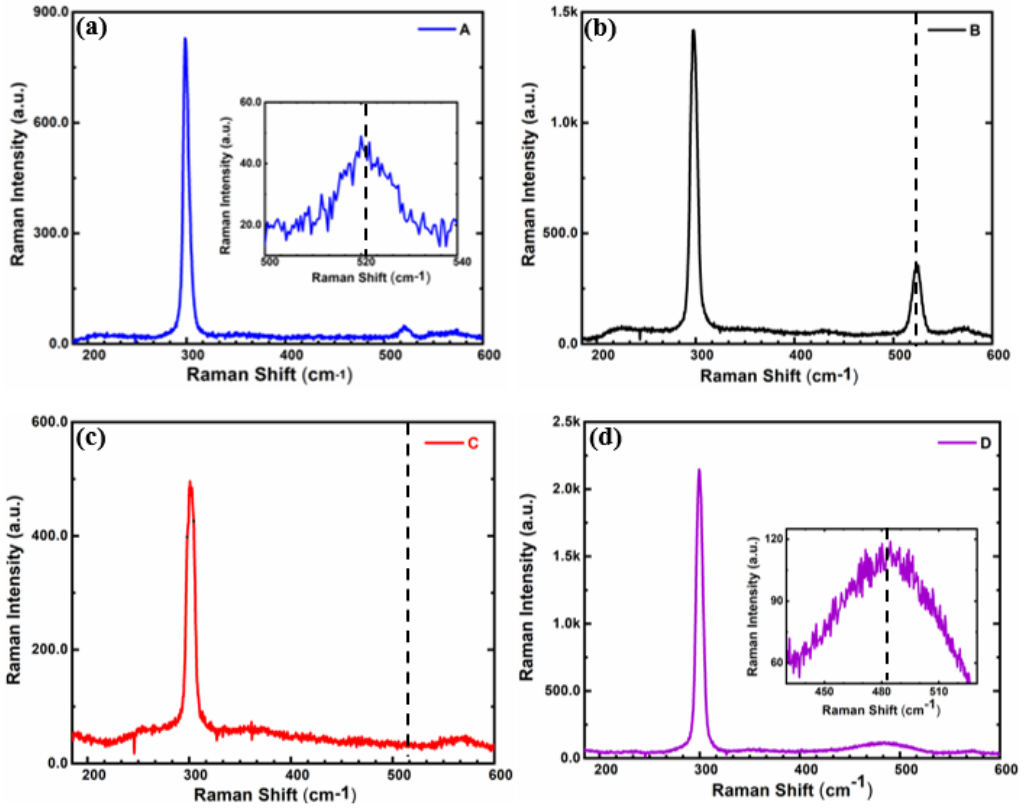

Figure 7.3. Raman spectra of Si-on-Ge heteroepitaxial growth of (a) Sample A (b) Sample B (c) Sample C and, (d) Sample D. The dashed line represents the characteristic Raman shift peak position of either crystalline (520 cm^{-1}) or microcrystalline/amorphous (480 cm^{-1}) Si growth.

The dashed line represents the characteristic Raman shift peak position of either crystalline (520 cm^{-1}) or microcrystalline/amorphous (480 cm^{-1}) Si growth. The Ge-Ge mode peaks of the

samples are also situated in the neighborhood of 300 cm^{-1}. In this work, the focus is on the Si-Si mode peaks.

With the exception of sample B which shows pronounced, narrow and distinct spectra characteristic of a typical Si peak in its crystalline state, other samples are characterized by either a (i) broadened, lower intensity Si peak indicating a comparatively lesser crystalline quality (Sample A), (ii) non-obvious peak with signs of no Si deposition due to lower thickness film (sample C) or (iii) lower wavenumber amorphous Si peak sample (sample D) at 480 cm^{-1}. In cases where the peaks are non-obvious such as sample C, micro-Raman measurements can be performed to provide information regarding the crystalline/amorphous natures of the Si peak. Since one of the overarching objectives of this work is to deposit thin (10 – 40 nm) crystalline Si on Ge at low growth temperatures ($\leq 300^{o}C$), the impact of the growth parameters on the Raman spectra is discussed accordingly. Of the four grown samples, A and B appears to produce c-Si films (crystalline silicon) or at least, the closest to being an indication of a crystalline Si film. An outcome favored by an informed interplay of the dilution ratio, the applied plasma power density and or the growth temperature.

Using Sample A as a comparative baseline, it appears that a slightly lower dilution ratio (19 against 32) and higher plasma power (10 W against 3 W) would result in a more crystalline silicon product when grown at a higher growth temperatures ($300^{o}C$ against $250^{o}C$). It is also possible that the temperature is the major driving factor since it can favor the surface energetics of the Si adatoms. While this is not a general rule of thumb, the result speaks to the validity of this statement. It is also noteworthy to mention that the Raman measurements were carried out at different spots of the samples for result reproducibility and repeatability and reliability.

7.3.2 Atomic Force Spectroscopy

To inspect the surface morphology and possibly infer the growth mechanism of the Si-on-Ge growth, the use of the AFM system is employed. Figure 7.4 shows the AFM images and corresponding surfaces roughness values of all the samples.

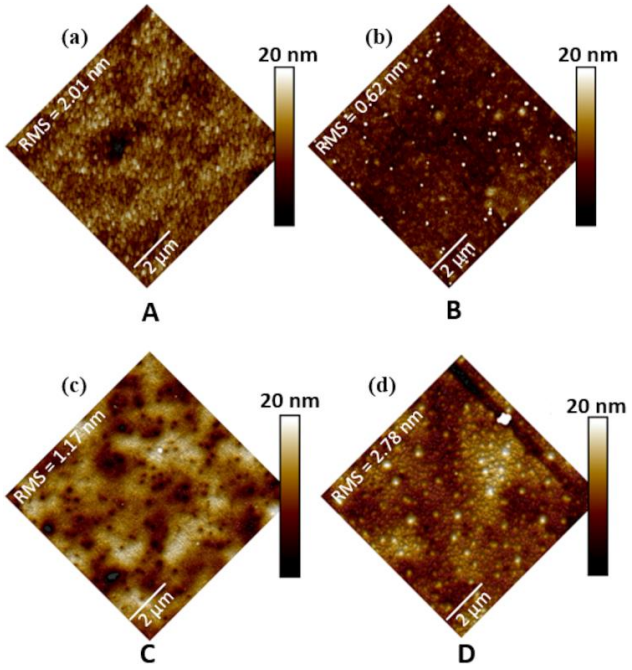

Figure 7.4. Comparisons of the surface roughness of the samples using Atomic Force Microscopy (AFM)

Measurements are taken and repeated for at least four times per samples within sample areal observations of 2 µm x 2 µm. This is done to provide an aggregated measure of the surface roughness. From sample A to D, the average surface roughness values are 2.01 nm, 0.624 nm, 1.17 nm to 2.78. Sample B has the lowest surface roughness at 0.624 nm, while sample D has the highest at 2.78 nm. Based on this evaluation, sample B proves a better film quality given its comparatively lower surface roughness. The surface roughness was also found to be the closest to the roughness of a bare Si wafer which was measured to be 0.128 nm. This realization points

to the fact that sample B possesses a more crystalline morphology compared to the other samples. The increase in surface roughness is inferred to be due to a number of factors relating to the bombardment of the sample surface by high energy radicals, etching of the surface by atomic hydrogen produced during the growth [162] and well as the growth of Si island features due to the large lattice mismatch between Si and Ge [172,173]. It also possible that the formation of the island growth may have been due to poor surface wetting of the Si film given its higher surface energy compared to the underlying Ge film – condition for the realization of the Franck de Merwe layer-by-layer growth mode [174].

Notice the presence of Si Island features on all the AFM images (Figure 7.4). These features are visually less prominent in sample B and clearly more pronounced in sample D featuring rounder and larger blobs. These island features appear to be one or the factors determining the degree of surface coarsening or smoothening of the sample surface. In fact, increasing surface roughness is an possible indicator of crystalline to amorphous growth transitions at low temperatures [175]. The formation of these multiple Si Island growth is an offshoot of Stransky-Krastanov growth mode (2D/3D island growth) and finds expressions given the reason mentioned above. Based on these AFM results, it is possible to deduce that the growth mechanism of Si on Ge heteroepitaxial structure is governed by the impact of the plasma radicals on the surface kinetics[162], islanding or possible intermixing at the Si/Ge interface leading to the formation incoherent SiGe feature at this interface [173].

7.4 Discussion and summary

Although, a prime objective of this work was to explore the favorability of increasing the deposition growth rate of Si on Ge. The aim was partly achieved for Samples A (2.47 nm/min)

and B (6.34 nm/min) since the ensuing growths rate enabled the formation of crystalline Si. Growth rates of other samples either gave rise to amorphous-type Si deposition (Sample D – 9.47 nm/min) or non-discernible Si deposition (Sample C – unsure if the epi-growth is amorphous or crystalline) (1.00 nm/min). Based on this result, there exists a range of growth rate target values that favor the crystalline Si growths, and for this case, it may possibly be within a subjective range of 2 – 4 nm/min. Higher growth rates may deliver amorphous outcomes since in this state, the time taken for Si adatoms to find an energetically favorable site to get locked-in before the deposition of an overlying Si layer is reduced. Other suggestions to attain an optimal growth rate would be to explore higher growth pressures. To also suppress the prevalence of island growths, a suitable surfactant should be applied accordingly. As far as this work, additional structural characterization steps such as XRD, TEM and SEM need to be conducted for a more accurate narrative of the growth mechanism.

This work demonstrates the possibility of growing heteroepitaxial thin crystalline films of Si on Ge films at low temperatures using plasma technology. The quality of the growth is dependent on the controlled application of H_2:SiH_4 dilution ratios, plasma power density and growth temperatures. Raman and AFM measurements show clear evidence of crystalline Si deposition. Further analysis of the characterization results infer that the Si-on-Ge growth mechanism is governed by a number of competing factors such as the impact of the plasma radicals on the surface kinetics[162], islanding or possible intermixing at the Si/Ge interface leading to the formation incoherent SiGe feature at this interface [173].

7.5 GeSn Epitaxy

7.5.1 GeSn on Ge buffered Si Growth

Advances in Group IV binary alloys have elevated their position as a competitive material system for applications involving the integration of photonics and optoelectronics devices on Si platforms [9,23,36,73,176]. With the realization of a truly direct bandgap GeSn, revolutionary progresses have been pioneered through development of optically pumped and electrically-injected lasers [23,85,92]. Based on these merits, the market adoption of a slew of Si-based optoelectronics devices that caters to the far and mid-infrared application is in the horizon [22,114,177]. While these are notable achievements, the epitaxial deposition of GeSn on Ge presents a challenge due to its solubility limitations coupled with alpha α-Sn's instability at 13^{o}C. To circumvent these challenges, low temperature non-equilibrium growth options involving the use of MBE [178–180] or CVD [99,110,176,181] technologies have been pursued meritoriously.

As far GeSn growth using the CVD growth route, several Ge and Sn precursor gases have been applied to achieve high quality and high Sn incorporation growths. Of the early adopted options, Deuterium stabilized stannane (SnD_4) and tin tetrachloride ($SnCl_4$) stood out substantively but due to the instability and cost-ineffective limitations of the former (Stannane), $SnCl_4$ easily becomes the preferred precursor gas of choice for Sn deposition [182]. On the other hand, precursor gases of various hydride chemistries have also been explored for Germanium (Ge) deposition [181], but the higher order hydrides possess the advantage of easier decomposition at low temperatures [99]. Although, single-order, low-cost Ge hydride (Germane, GeH_4) have also been employed to achieve GeSn growths via a custom UHCVD system. Although the possibility of GeSn growth has been demonstrated, the qualitative and quantitative assessment of the growth quality is determined by the amount of incorporated Sn in the Ge lattice. As such, Sn incorporation serves as a figure of merit for both growth and device development measures. The importance of a higher Sn incorporation cannot be overemphasized

in that, it improves the bandgap directness of a device while automatically enhancing its efficiency. In a separate but connected scale, a higher Sn incorporation increases the spectral cut-off wavelength of a detection device thereby making it suitable for long-wavelength detection capabilities.

To increase the chances for higher Sn incorporation, three growth ideals are currently pursued. The first applies higher order germane such as Ge_2H_6 or Ge_3H_8 and higher. Based on this, a relatively high Sn incorporation of > 10% has been achieved by Loo et. al [183]. The second option employs the additional machinery of a plasma technology to speed-up the reaction kinetics of GeSn in a UHVCD system while the third option is an attempt to increase the growth pressure. While this has been demonstrated for high growth pressure (120 Torr) [184], this experiment attempts to achieve substantial Sn incorporation at low pressures.

7.6 Growth Method

Five (5) GeSn samples were grown at different growth pressures using p-type Si (001) substrates via a customized ultrahigh vacuum chemical vapor deposition (UHVCVD) system. The resistivity of the Si wafer is ~ 10-20 Ω.cm while the maintained base pressure of the system's process chamber is kept 10^{-10} Torr. Prior to the growth, the substrate was subjected to a standard piranha etch procedure that consists of measured bath solution of sulfuric acid and hydrogen peroxide under a one-to-one mix ratio, i.e. (H_2SO_4: H_2O_2 = 1:1). Following this procedure, a hydrogen passivation process was applied for the removal and protection against surface oxidation.

Similar to our previous works [185], Germane (GeH_4) and Tin Tetrachloride ($SnCl_4$) reactor gases were utilized as dominant precursors of Ge and Sn with Ar used as the carrier gas. To initiate the growth process, a two-step Ge buffer was deposited where the first Ge layer was

deposited to produce relaxed film a low temperature of 375°C while preventing possible island formation. The second layer was then applied at a relatively higher temperature (600°C) to achieve higher quality growth, after which a GeSn epilayer was grown at 260°C. The rationale for growing epitaxial GeSn film at this temperature has been demonstrated in a prior experimental work where the goal was to identify an optimized growth regime that sponsors high Sn incorporation and low Sn precipitation. The details of the experimental motivations and results are also discussed in reference [185]. The generalized schematic of the GeSn-on-buffered Ge Si substrate as well as the applied growth parameters and conditions are shown in Figure 7.5 below.

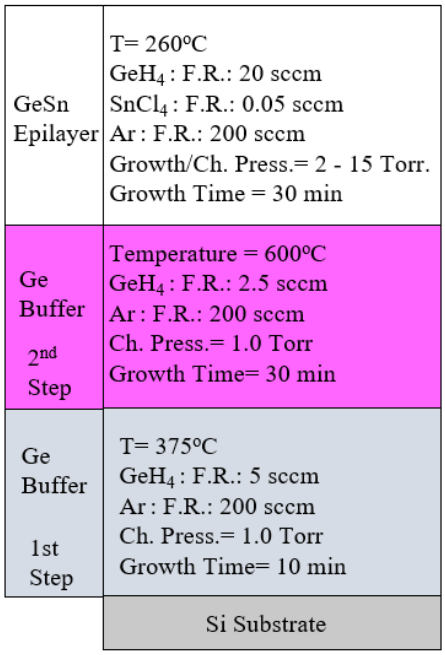

Figure 7.5. Representative heterostructure schematics of the GeSn on buffered Si growth. The generalized growth conditions are also presented.

GeSn-on-Ge buffered Si heterostructures identified as samples A, B, C, D and E were grown at different pressures of 2, 4, 8, 10 and 15 Torrs, respectively. All GeSn films were grown for 30 minutes, with the exception of Sample B which grown for 60 minutes.

This work also explores the low-temperature and pressure-dependent capability of our in-house ultra-high vacuum chemical vapor deposition machine. This experiment aims to identify a new growth window that favors the incorporation of high Sn while also studying the effect of pressure on the growth outcomes.

7.7 Material and Optical Characterization

Post-growth optical and structural properties exploration were conducted to investigate the quality of the grown pressure-dependent GeSn heterostructures. Firstly, XRD rocking curve 2θ-ω scans of the respective samples were collected using a high-resolution X'pert PRO diffractometer. This structural technique investigates the sample thickness and the overall quality. It is noteworthy to mention that, although the XRD reciprocal space map (RSM) could have provided further information such as the Sn incorporation and the strain, the measurement was not taken at the time of this experiment. In addition to the XRD 2θ-ω scans, additional optical characterization procedures were performed using Raman and ellipsometry measurement methods. The Raman set up comprises of an integrated system of grating-based spectrometer (Horiba iHR 550), a coupled charge coupled device detector and a 632 nm He-Ne excitation laser source. This measurement verifies the GeSn growth while inspecting the longitudinal optical Raman phonon peak shift. Ellipsometry measurements are performed using the variable-angle system (Wollam model VASE32). The measurement wavelength range of the machine is between 260 to 2500 nm with an incidence angle of 70^{o}. Absorption spectra of the respective samples were extracted and fitted using the models described in reference [103].

7.8 Results and discussions

Figure 7.6 shows the high resolution XRD rocking curves of the GeSn samples deposited at different growth pressures. Sample A, B, C, D and E are grown at 2, 4, 8, 10 and 15 Torrs respectively.

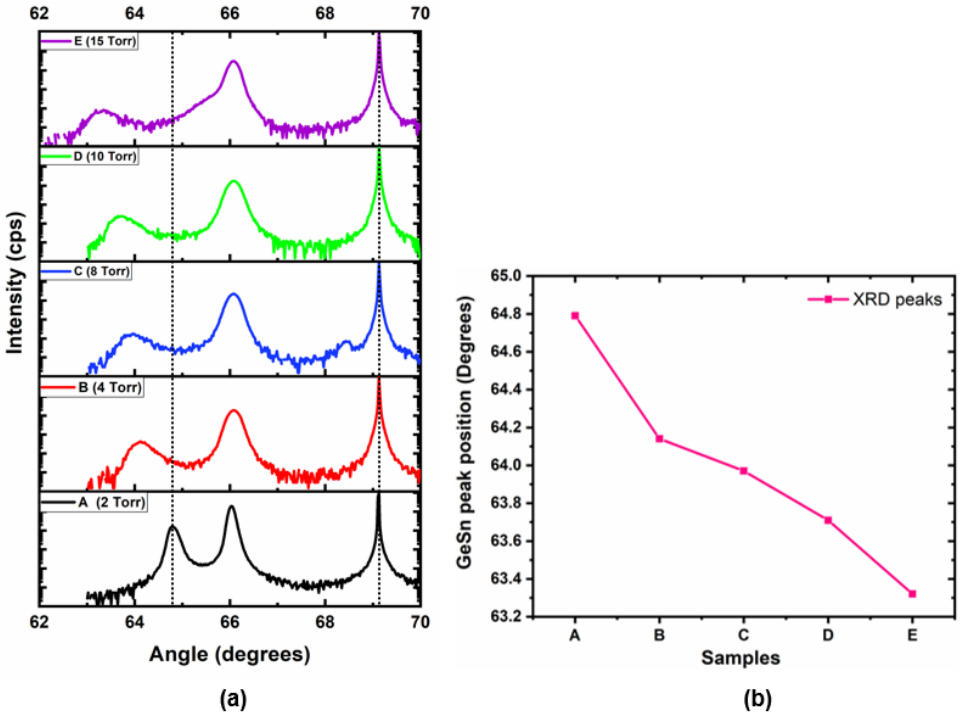

Figure 7.6. Stacked XRD rocking curves along plane (004) of (a) all samples at different growth pressures. Vertical dashed lines are added to observe GeSn peak shifts, and (b) extracted XRD peak position versus samples.

To investigate the effect of incremental growth pressures on the sample crystallization, the 2θ-ω scans of the rocking curves are stacked accordingly. Vertical dashed lines the left shows the resolved peak consistency of the Si substrate across all samples, while the right-most line is used to quantify the peak shift from lower to higher pressures. Distinctly resolved peaks at 66.1° and 69.2° are attributed to the Ge buffer and Si substrate, respectively, while the peaks closest to the right-most vertical dashed lines are associated with the GeSn layers.

Figure 7.6 (b) shows the Gaussian-fitted GeSn peak positions of the samples are observed to decrease with increasing growth pressures (A<B<C<D<E) indicating possible increase in Sn incorporation. In fact, previous XRD investigations attributes higher Sn incorporation to lower angle peak shifts [186]. To estimate the highest Sn incorporation based on this experiment, the peak angles of samples A, B, C, D and E are compared to results obtained from a previous study [186]. Since the lowest angle observed in this work is 63.32°/63.71° (samples D & E), and the reported lowest angle for the highest Sn samples is 65°, it is possible to infer that the Sn composition observed for the sample with the lowest diffraction angle will be > 7%. Of course, this would have been easier to estimate using reciprocal space map measurements, but this data was unavailable at the time of this experiment. Additional and available optical characterization techniques such as Raman and ellipsometry measurement may provide leading information to infer the Sn incorporation as well as the optical quality of these pressure-dependent samples. The results are discussed in subsequently. In addition to the above observations, it is worth noting that although sample A exhibits the lowest peak diffraction, its line-width is also lower than those obtained from other samples indicating a higher quality sample comparatively.

The next step in the optical characterization process involves using results from Raman technique to understand the degree of crystallization of each sample. This method also provides qualitative estimate of the Sn incorporation from the inferred strain information. Figure 7.7 (a -e) below shows the Raman spectra of the respective samples at different growth pressures. In addition to the measurements, a bulk Germanium (Ge) substrate of Ge-Ge LO standard phonon

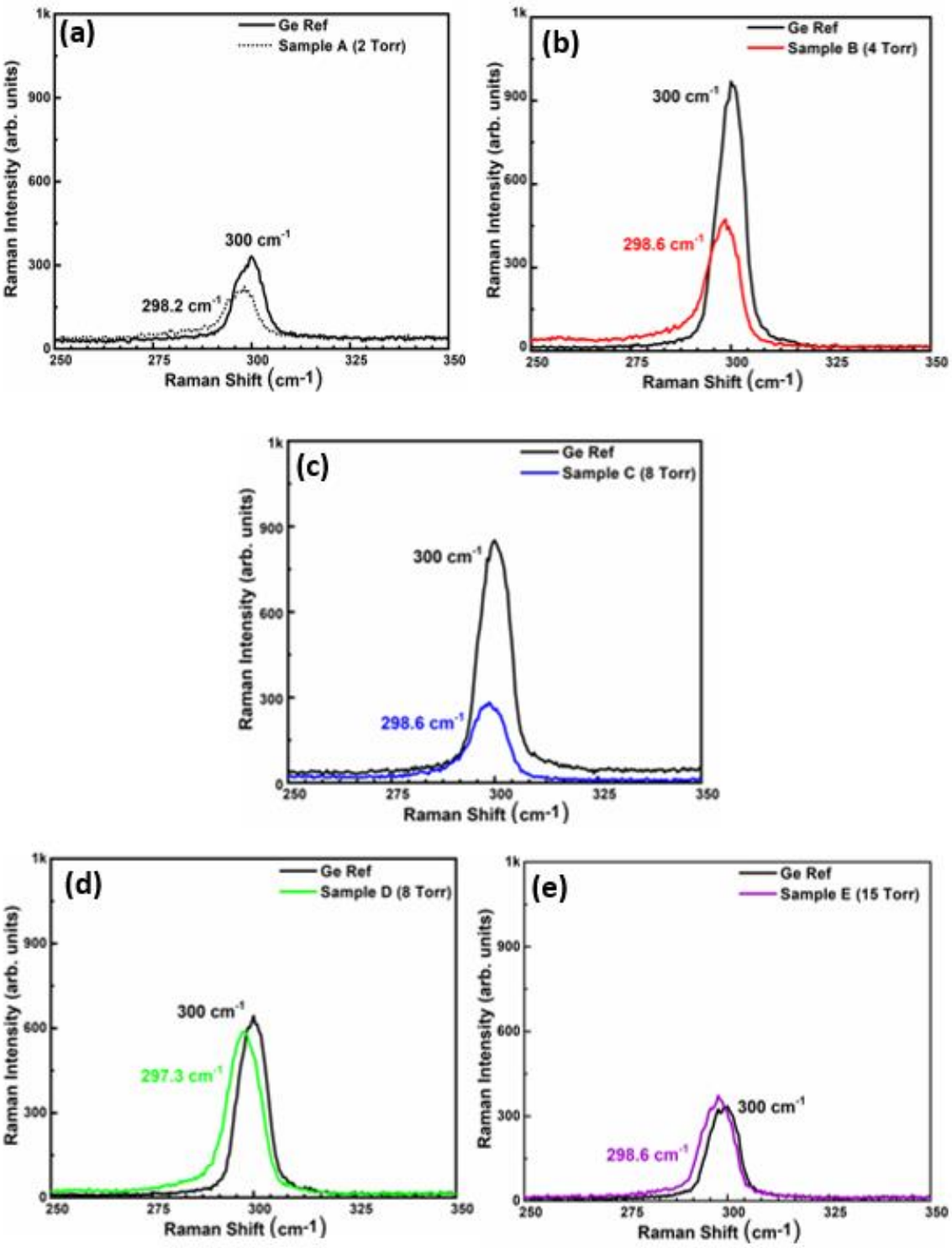

Figure 7.7. Raman spectra of (a) Sample A (B) Sample B (c) Sample C (d) Sample D and, (d) Sample E showing Ge-Ge LO Raman shifts.

peak (300 cm^{-1}) was used as reference sample to calibrate the Raman set-up before sample measurements were taken. The Raman peak shift of the epi-GeSn films of samples A, B, C, D and E are 298.2 cm^{-1}, 298.6 cm^{-1}, 298.6 cm^{-1}, 297.3 cm^{-1} and 297.7 cm^{-1} respectively.

For all the samples, the Raman peaks are shifted to the lower wavenumber which is indicative of induced strain as a result of the incorporation of Sn into Ge matrix. In fact, the more shifted a peak is to lower wavenumber, the higher the Sn incorporation. Based on the collected Raman information, Sample D features the lowest wavenumber of the five samples. This result matches the XRD rocking curve 2θ-ω scan, since at this wavenumber, the extracted GeSn XRD peak position is also relatively low. Based on these results, it is possible that Sample D (10 Torr) has the highest Sn incorporation of the grown sample suggesting a window for future GeSn growths. To confirm the above statement, additional optical characterization data was taken where the absorption spectra of all samples are obtained from ellipsometry measurements and are shown in Figure 7.8 (a) below.

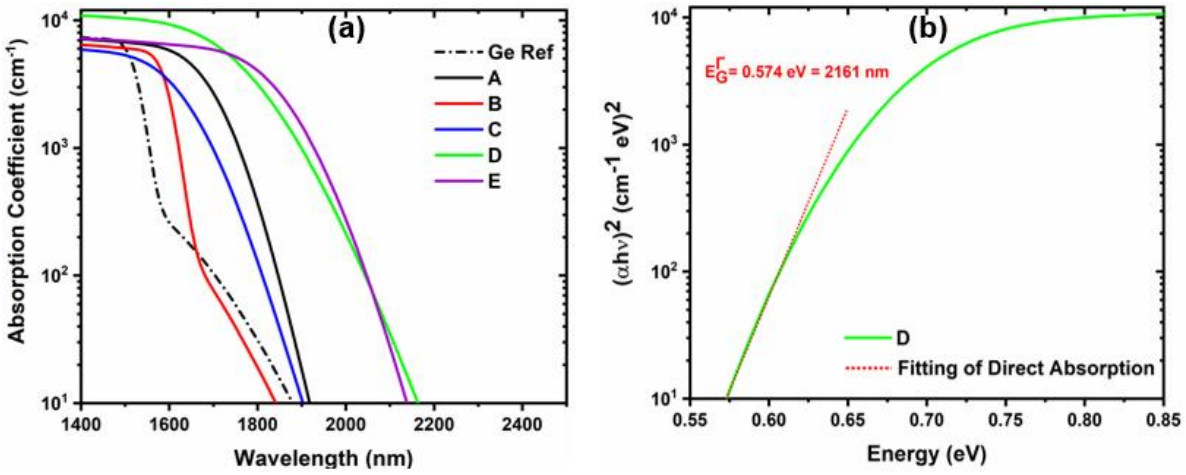

Figure 7.8. Absorption spectra of (a) samples A, B, C, D and E at different pressures and, (b) Fitted direct absorption curve of sample featuring the lowest bandgap energy at 0.574 eV.

Absorption coefficient data of Germanium (Ge) was added as reference to simplify analysis. In comparison to the Ge reference sample, absorption curves of samples A, C, D, E are significantly red-shifted suggesting that the origin of the absorption measurement emanated from the GeSn layer. This observed red-shift in the absorption edge also confirms the incorporation of Sn. On the curve, there appears a competition between the behaviors of samples D and E, with samples D indicating a higher cut-off wavelength comparatively (higher Sn incorporation). These results are also consistent with Raman and XRD measurements. Additionally, the absorption curves of sample B features both direct and indirect bandgap absorptions. On the other hand, a material (A, C, D and E) exhibits predominant direct bandgap transitions/natures when the incident photon energy surpasses the direct bandgap energy E_g^{Γ}. The absorption characteristics of the direct bandgap energy can be expressed using the method discussed in reference [103].

$$\alpha h\nu^{\ 2} = A\ h\nu - E_g^{\Gamma} \qquad \text{(Equation 7.1)}$$

where α represents the absorption coefficient of the direct bandgap, hν accounts for the photon energy, A is a constant and E_g^{Γ} is regarded as the associated energy of the direct bandgap. This energy is extracted by fitting the absorption curves in Figure 7.8 (a). Figure 7.8 (b) shows the fitting procedure of E_g^{Γ}, where the parameters $(\alpha h\nu)^2$ and $h\upsilon$ are dependently analyzed. The absorption curve of sample D is subjected to a linear fit process for the direct bandgap energy to be extracted (E_g^{Γ} = 0.5745 eV). This is equivalent to a spectral cut-off wavelength of 2161 nm indicated on the dotted line of Figure 7.8 (b). Recent reports have shown that pseudomorphic growth of GeSn on Ge buffered Si exhibit direct bandgap properties of Sn concentration between 8-10 %. While this is yet a record accomplishment, the results demonstrate to the potential of our

in-house UHVCVD machine in achieving far higher Sn incorporation. The summaries of the characterization results are shown in Table 7.2 below

Table 7.2. Summary of the characterization results

Sample ID	Pressure	Thickness	Ellip. Cut-off		Raman (cm-1)		XRD (2θ-ω)
	(Torr.)	(nm)	(nm)	(eV)	Peak	Shift	Deg. (°)
A	2	153	1917	0.6477	298.2	-1.8	64.79
B	4	27	1840	0.6748	298.6	-1.4	64.14
C	8	287	1902	0.6528	298.6	-1.4	63.97
D	10	89	2161	0.5745	297.3	-2.7	63.71
E	15	68	2138	0.5807	297.7	-2.3	63.32

7.9 Conclusion

This work also explores the low-temperature and pressure-dependent capability of our in-house ultra-high vacuum chemical vapor deposition system. This experiment aims to identify a new growth window that favors the incorporation of high Sn while also studying the effect of pressure on the growth outcomes. GeSn-on-Ge buffered Si heterostructures identified as samples A, B, C, D and E were grown at different pressures of 2, 4, 8, 10 and 15 Torrs, respectively.

Post-growth optical characterization measurements using Raman, and ellipsometry methods shows that Sample D (10 Torr) exhibits the lowest Ge-Ge LO phonon peak shift and the longest spectral cut-off at ~ 2161 nm. Based on previous reports, this cut-off wavelength is estimated to feature ~ 8 -10 % Sn incorporation, although additional characterizations such as XRD Reciprocal space map (RSM) and PL still needs to be carried out to confirm the exact Sn composition. While this is yet a record accomplishment, the results demonstrate to the potential of our in-house UHVCVD machine in achieving far higher Sn incorporations. Finally, this work suggests a new growth window for future GeSn deposition at pressures between 10 and 15 Torrs.

Chapter 8: Dissertation Summary, Conclusion, and Future Work

8.1 Summary and Conclusion

This work focuses on understanding the optical and structural properties of GeSn heterostructures. The first portion of this dissertation investigates the structural and optical properties of SiGeSn/GeSn/SiGeSn quantum wells using select excitation lasers, while the second portion delves deeply into bulk GeSn heterostructures with the aim to understand the impact of annealing on the structural and optical properties of bulk GeSn samples with Sn concentration close to the indirect-to-direct transition points. Investigations on bulk heterostructures is concluded by exploring the low temperature capability of our in-house plasma-enhanced UHVCVD machine through the growth of Si-on-Ge before transitioning into the pressure-dependent growth of GeSn bulk heterostructures. The growth part of this summarizes my experience growing these semiconductor bulk structures and aims to provide an quick outlook into our growth strategies, processes, and capabilities.

This dissertation begins by introducing the growth and characterization methods employed in major parts of this work. The functional capabilities of our in-house plasma-enhance UHVCD system as well as that of the RPCVD systems are discussed. Theoretical and operational workings of all characterization techniques are presented to provide the reader a reference point in the more advanced subsequent chapters.

This chapter segues into the major portion of the dissertation that investigates the optical properties of SiGeSn/GeSn/SiGeSn quantum wells where the PL behaviors of a thick (22 nm) and thin (9 nm) QW samples are compared. It is worth noting that prior to this comparative analysis, the structural, PL and optical analysis of the 9 nm QW sample has been studied as an incremental contribution to improving emission, carrier and optical confinements of GeSn QWs.

The results show that due to the relatively thin QW width, the impact of quantum-size effect is more pronounced in the well giving rise to a reduced barrier height. The evidence is observed in the well's ground energy level being higher than the Γ valley minimum of the bulk structure.

To increase the barrier height while simultaneously improving the carrier confinement, the GeSn growth structure is optimized by increasing the QW's thickness by more than 2x the width of the thinner sample. This serves the motivation for comparing the optical properties of a thicker QW sample (22 nm) to the thinner well sample (9 nm). Using PL results from two excitation lasers (532 nm and 1550 nm lasers) as well as studying their respective optical transitions, the results reveals that the thicker QW sample shows i) a more direct bandgap outcome in addition to a much lower ground energy Γ valley; ii) a higher carrier density within the well; and iii) an increased barrier height coupled with an improved carrier confinement. All of these resulted in a significantly enhanced emission which allows for the first-ever estimation of quantum efficiency (QE) calculated for GeSn QWs. The estimated spontaneous QE and external QE are 37.9% and 1.45% respectively.

To further improve the carrier confinement while also reducing the carrier leakage in this thicker well design, a SiGeSn/GeSn/GeSn/SiGeSn separate confinement heterostructure (SCH) is introduced. In the same manner as the previous sample, the SCH QW sample is also grown in a commercial RPCVD machine and are held to precisely-controlled growth standards as confirmed by XRD, SIMS and TEM results. The sample is characterized and the optical properties; the PL of a 532 nm and 1550 nm lasers are compared with the previously reported 9 nm and 22 nm non-SCH single QWs. The significantly enhanced emission from SCH quantum well was obtained as a result of separately confined quantum well active region. Based on the optical transition analysis, SCH QW also shows a significantly higher carrier confinement compared to reference samples.

In addition to these studies, an attempt is made to investigate advanced quantum well structures through an all-inclusive structural and optical study of SiGeSn/GeSn/SiGeSn multi quantum wells (MQWs). An experimental account of the impact of QW intermixing on the PL emission of MQWs samples are discussed. X-ray diffraction (XRD), Secondary Ion Spectrometry (SIMS) and modeled defect density data were thoroughly analyzed for connections. The resulting analysis show evidences of intermixing diffusion during growth, especially along the deeper GeSn/SiGeSn interfaces below the surface. Indications of these intermixing events are far more obvious at larger depth below the sample as observed on the SIMS record where the Sn concentration reduces (of up to 2.0 ± 0.2 at. %) with respect to the duration at which the interfaces are cumulatively subjected to the applied growth temperatures. Findings also reveal that despite their larger PL line-widths, these higher period structures possess better optical performance comparatively.

The second portion of this dissertation deals with bulk GeSn heterostructures and aims at understanding the impact of annealing on the structural and optical properties of bulk GeSn samples with Sn concentration close to the indirect-to-direct transition points. Connections have been established for the composition, defect density, strain and PL observed for the pre-and post-annealed GeSn alloys of Sn compositions near the indirect to direct optical transition points. The as-grown GeSn samples range between an Sn composition of 8% to 10%, and were annealed at a specific temperature of 300^{o}C. The result reveal that depending on the sample's relative position on the transition point, the impact of annealing on a sample may either i) lowers the strain giving rise to an increased PL by reducing the energy separation or ii) introduce misfit dislocation/ surface roughness with results in an affected or decreased PL. Deductions from this study suggests that by growing an additional Ge capping layer on the GeSn surface it is possible to

curtail the impact of the surface roughness towards improved on the optical performance above room temperature. Of course, a different rule of thumb exists for GeSn samples with Sn compositions above the transition points where the PL emission manifests as a direct bandgap material.

The last portion of this work explores the low temperature capability of our in-house plasma-enhanced UHVCVD machine through the growth of Si-on-Ge before transitioning into the pressure-dependent growth of GeSn bulk heterostructures. As for the Si-on-Ge heteroepitaxial aspect of this work, the quality of the growth is dependent on the controlled application of H_2:SiH_4 dilution ratios, plasma power density and growth temperatures. Although additional characterization steps such as XRD, TEM and SEM need to be conducted for a more accurate narrative of the growth mechanism. Further analysis of the characterization results infer that the Si-on-Ge growth mechanism is governed by a number of competing factors such as the impact of the plasma radicals on the surface kinetics[162], islanding or possible intermixing at the Si/Ge interface leading to the formation incoherent SiGe feature at this interface [173].

The pressure-dependent GeSn growth demonstrates the capability of our plasma-enhanced UHVCVD system in growing high Sn incorporation samples. This work hypothesizes that it is possible to increase the Sn incorporation of grown by optimizing the growth pressure. Since this is an on-going effort, only characterization results from the ellipsometry, Raman and rocking curve (2θ-ω) XRD measurements are presented and discussed. This part of the work also summarizes my experience growing these GeSn bulk structures and aims to provide a quick outlook into our growth strategies, processes, and capabilities.

8.2 Future Work

8.2.1 GeSn well design consideration

Although an increased carrier confinement/PL emission has been realized for thicker QW designs, these growths may result in lower quality QW samples. Careful control must be applied to achieve a balanced thickness suitable for enhanced device performance. Corresponding barrier thickness as well as strain relaxation should be considered in future designs. A step above the single SiGeSn/GeSn QWs are high quality MQWs. To achieve high-gain lasers for future optoelectronics applications, the growth of identical MQW is also suggested. Future MQW designs need consider a strain-balanced QW growth approach that comprise of a relaxed GeSn buffer, a tensile-strained SiGeSn and a compressively strained GeSn well. Overall, the MQW structure would feature zero average in-plane stress.

8.2.2 QW annealing investigation

Since a part of this dissertation explores the influence of annealing on bulk GeSn structures, an attempt should be made at investigating the impact of long-term or rapid thermal annealing on the structural and optical properties of SiGeSn/GeSn/SiGeSn single and MQWs. To better understand the structural and optical behaviour of quantum well samples under long-term thermal influence, four SiGeSn/GeSn QW materials with similar Sn compositions have been identified to used in a future study: (i) Single (13.5 Sn %), (ii) double (13 Sn %) and four QW (13.8 Sn %) – Not shown. Our study targets materials with similar Sn compositions and differing number of quantum well periods (one to four). Understanding the evolution of these samples under annealing room temperature impact is critical to understanding the device performance/reliabilities at this specific temperature. In addition to our annealing exercise, the projects aims to provide an in-depth physics outlook to the question of what happens to the

optical/structural character of an as-grown QW sample as it evolves from a being single QW to an N-number of quantum well. The result above show preliminary annealing study of a single QW sample (13.5% Sn).

The figures above show the XRD rocking curve, PL measurements at 10K, and the RSMs of the as-grown and annealed samples for comparisons. Sample was subjected to 4 hrs of annealing time at 300°C in vacuum condition. XRD ω/2θ scan (Fig. 8.1 (a)) reveals the direct impact of annealing on the sample pronounced by the appearance of an additional peak at the lower angle side of the Ge buffer.

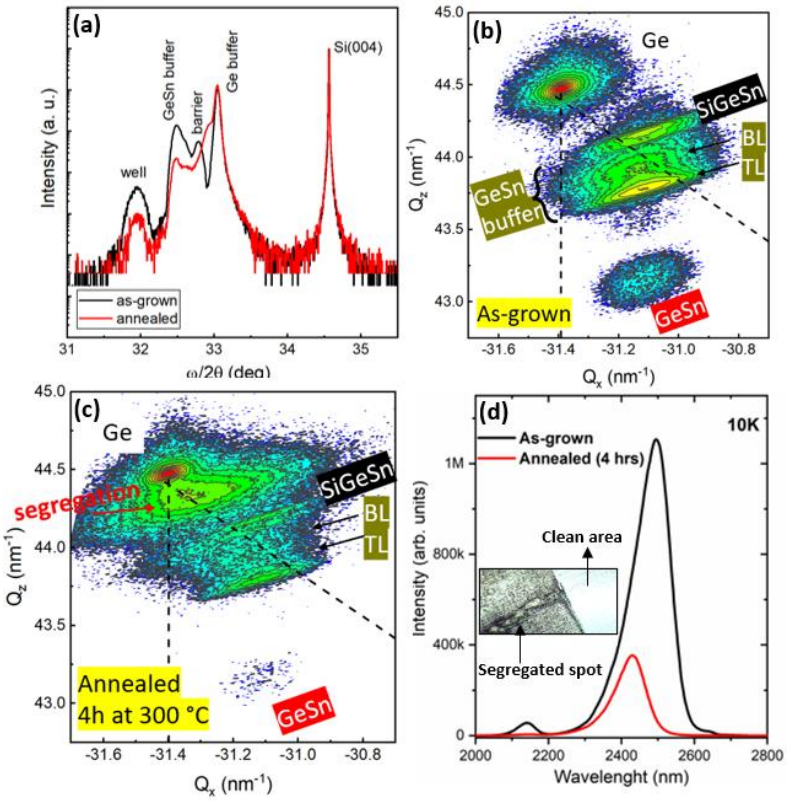

Figure 8.1. X-ray diffraction 004 ω/2θ scans, (b) and (c) X-ray diffraction $\bar{2}\bar{2}4$ RSMs before and after annealing for 4 hours at 300°C (c) PL spectra at 10K before and after annealing for 4 hours

Figures 8.1 (a) and 8.1 (b) shows the X-ray diffraction RSMs before and after annealing for 4 hours. The Sn segregation is further identified in the RSM plot Fig. 8.1 (c) of the annealed

sample (see red arrow). Although not shown, the visual appearance of the sample after annealing is marked by two distinct regions: a 'clean' portion (dark) with similar the outlook of the sample before thermal subjection and a 'segregated' greyed-out sporadically distributed portion (see inset in Fig. 8.1 (d). Based on these observations, it is observed that the regions with original barrier/well/barrier structure are preserved while the location of the peaks (SiGeSn, BL, TL, GeSn) on the RSM of the annealed sample seems to not differ sufficiently compared to the as-grown sample. As for the PL outcome, the sample shows a significant drop in intensity after annealing with a noticeable shift to lower wavelength (red-shifted).

For more revelatory insights on the material evolution, this work will pursue lower annealing time of shorter increments (30 mins or hourly intervals). This approach would enable the understanding of the transitory evolution of the Sn segregation as well as the possibility of an enhanced emission within these intervals. Following these attempts, we will then perform the same experimental procedures on two and four QW materials with the intent of extracting leading deductions about the optical and structural properties.

References

[1] Vlasov Y, Green W M J and Xia F 2008 High-throughput silicon nanophotonic wavelength-insensitive switch for on-chip optical networks *Nature Photon* **2** 242–6

[2] Anon 2010 Simply silicon *Nature Photon* **4** 491–491

[3] Leuthold J, Koos C and Freude W 2010 Nonlinear silicon photonics *Nature Photon* **4** 535–44

[4] Soref R A 1993 Silicon-based optoelectronics *Proceedings of the IEEE* **81** 1687–706

[5] Wang Z, Tian B, Pantouvaki M, Guo W, Absil P, Van Campenhout J, Merckling C and Van Thourhout D 2015 Room-temperature InP distributed feedback laser array directly grown on silicon *Nature Photon* **9** 837–42

[6] Liang D and Bowers J E 2010 Recent progress in lasers on silicon *Nature Photon* **4** 511–7

[7] Tanabe K, Watanabe K and Arakawa Y 2012 III-V/Si hybrid photonic devices by direct fusion bonding *Sci Rep* **2** 349

[8] Du W, Ghetmiri S A, Conley B R, Mosleh A, Nazzal A, Soref R A, Sun G, Tolle J, Margetis J, Naseem H A and Yu S-Q 2014 Competition of optical transitions between direct and indirect bandgaps in Ge1−xSnx *Appl. Phys. Lett.* **105** 051104

[9] Ghetmiri S A, Du W, Margetis J, Mosleh A, Cousar L, Conley B R, Domulevicz L, Nazzal A, Sun G, Soref R A, Tolle J, Li B, Naseem H A and Yu S-Q 2014 Direct-bandgap GeSn grown on silicon with 2230 nm photoluminescence *Appl. Phys. Lett.* **105** 151109

[10] Rong H, Jones R, Liu A, Cohen O, Hak D, Fang A and Paniccia M 2005 A continuous-wave Raman silicon laser *Nature* **433** 725–8

[11] Homewood K P and Lourenço M A 2015 The rise of the GeSn laser *Nature Photonics* **9** 78–9

[12] Thomson D, Zilkie A, Bowers J E, Komljenovic T, Reed G T, Vivien L, Marris-Morini D, Cassan E, Virot L, Fédéli J-M, Hartmann J-M, Schmid J H, Xu D-X, Boeuf F, O'Brien P, Mashanovich G Z and Nedeljkovic M 2016 Roadmap on silicon photonics *J. Opt.* **18** 073003

[13] Wang X and Liu J 2018 Emerging technologies in Si active photonics *J. Semicond.* **39** 061001

[14] Asghari M and Krishnamoorthy A V 2011 Energy-efficient communication *Nature Photon* **5** 268–70

[15] Bogaerts W, Fiers M and Dumon P 2014 Design Challenges in Silicon Photonics *IEEE Journal of Selected Topics in Quantum Electronics* **20** 1–8

[16] Soref R A and Perry C H 1991 Predicted band gap of the new semiconductor SiGeSn *Journal of Applied Physics* **69** 539–41

[17] Soref R A and Friedman L 1993 Direct-gap Ge/GeSn/Si and GeSn/Ge/Si heterostructures *Superlattices and Microstructures* **14** 189–93

[18] Pham T, Du W, Tran H, Margetis J, Tolle J, Sun G, Soref R A, Naseem H A, Li B and Yu S-Q 2016 Systematic study of Si-based GeSn photodiodes with 2.6 µm detector cutoff for short-wave infrared detection *Opt. Express, OE* **24** 4519–31

[19] Elbaz A, Buca D, von den Driesch N, Pantzas K, Patriarche G, Zerounian N, Herth E, Checoury X, Sauvage S, Sagnes I, Foti A, Ossikovski R, Hartmann J-M, Boeuf F, Ikonic Z, Boucaud P, Grützmacher D and El Kurdi M 2020 Ultra-low-threshold continuous-wave and pulsed lasing in tensile-strained GeSn alloys *Nature Photonics* **14** 375–82

[20] Margetis J, Al-Kabi S, Du W, Dou W, Zhou Y, Pham T, Grant P, Ghetmiri S, Mosleh A, Li B, Liu J, Sun G, Soref R, Tolle J, Mortazavi M and Yu S-Q 2018 Si-Based GeSn Lasers with Wavelength Coverage of 2–3 μm and Operating Temperatures up to 180 K *ACS Photonics* **5** 827–33

[21] Zhou Y, Dou W, Du W, Ojo S, Tran H, Ghetmiri S A, Liu J, Sun G, Soref R, Margetis J, Tolle J, Li B, Chen Z, Mortazavi M and Yu S-Q 2019 Optically Pumped GeSn Lasers Operating at 270 K with Broad Waveguide Structures on Si *ACS Photonics* **6** 1434–41

[22] Chrétien J, Pauc N, Armand Pilon F, Bertrand M, Thai Q-M, Casiez L, Bernier N, Dansas H, Gergaud P, Delamadeleine E, Khazaka R, Sigg H, Faist J, Chelnokov A, Reboud V, Hartmann J-M and Calvo V 2019 GeSn Lasers Covering a Wide Wavelength Range Thanks to Uniaxial Tensile Strain *ACS Photonics* **6** 2462–9

[23] Zhou Y, Miao Y, Ojo S, Tran H, Abernathy G, Grant J M, Amoah S, Salamo G, Du W, Liu J, Margetis J, Tolle J, Zhang Y-H, Sun G, Soref R A, Li B and Yu S-Q 2020 Electrically injected GeSn lasers on Si operating up to 100 K *arXiv:2004.09402 [physics]*

[24] Abernathy G, Zhou Y, Ojo S, Alharthi B, Grant P C, Du W, Margetis J, Tolle J, Kuchuk A, Li B and Yu S-Q 2020 Study of SiGeSn/GeSn single quantum well towards high-performance all-group-IV optoelectronics *arXiv:2009.12254 [physics]*

[25] Menéndez J, Sinha K, Höchst H and Engelhardt M A 1990 Phonons in epitaxially grown α-Sn1−xGex alloys *Appl. Phys. Lett.* **57** 380–2

[26] Goodman C H L 1982 Direct-gap group IV semiconductors based on tin *IEE Proceedings: Solid-State Electron Devices* **129** 189–92

[27] Moontragoon P, Soref R A and Ikonic Z 2012 The direct and indirect bandgaps of unstrained SixGe1−x−ySny and their photonic device applications *Journal of Applied Physics* **112** 073106

[28] Groves S and Paul W 1963 Band Structure of Gray Tin *Phys. Rev. Lett.* **11** 194–6

[29] Farrow R F C 1983 The stabilization of metastable phases by epitaxy *Journal of Vacuum Science & Technology B: Microelectronics Processing and Phenomena* **1** 222–8

[30] Farrow R F C, Robertson D S, Williams G M, Cullis A G, Jones G R, Young I M and Dennis P N J 1981 The growth of metastable, heteroepitaxial films of α-Sn by metal beam epitaxy *Journal of Crystal Growth* **54** 507–18

[31] Kouvetakis J, Menendez J and Chizmeshya A V G 2006 TIN-BASED GROUP IV SEMICONDUCTORS: New Platforms for Opto- and Microelectronics on Silicon *Annual Review of Materials Research* **36** 497–554

[32] Chang G-E, Chang S-W and Chuang S L 2010 Strain-Balanced $\rm Ge_z\rm Sn_1-z\hbox–\rm Si_x\rm Ge_y\rm Sn_1-x-y$ Multiple-Quantum-Well Lasers *IEEE Journal of Quantum Electronics* **46** 1813–20

[33] Beeler R, Roucka R, Chizmeshya A V G, Kouvetakis J and Menéndez J 2011 Nonlinear structure-composition relationships in the Ge${}_{1\ensuremath{-}y}$Sn${}_{y}$/Si(100) ($y<0.15$) system *Phys. Rev. B* **84** 035204

[34] Pukite P R, Harwit A and Iyer S S 1989 Molecular beam epitaxy of metastable, diamond structure SnxGe1−x alloys *Appl. Phys. Lett.* **54** 2142–4

[35] Zheng J, Wang S, Zhou T, Zuo Y, Cheng B and Wang Q 2015 Single-crystalline $Ge_{1-x-y}Si_xSn_y$ alloys on Si (100) grown by magnetron sputtering *Opt. Mater. Express, OME* **5** 287–94

[36] Gupta S, Chen R, Magyari-Kope B, Lin H, Yang B, Nainani A, Nishi Y, Harris J S and Saraswat K C 2011 GeSn technology: Extending the Ge electronics roadmap *2011 International Electron Devices Meeting* 2011 International Electron Devices Meeting p 16.6.1-16.6.4

[37] Hickey R, Fernando N, Zollner S, Hart J, Hazbun R and Kolodzey J 2017 Properties of pseudomorphic and relaxed germanium1−xtinx alloys ($x < 0.185$) grown by MBE *Journal of Vacuum Science & Technology B* **35** 021205

[38] Kormoš L, Kratzer M, Kostecki K, Oehme M, Šikola T, Kasper E, Schulze J and Teichert C 2017 Surface analysis of epitaxially grown GeSn alloys with Sn contents between 15% and 18% *Surface and Interface Analysis* **49** 297–302

[39] Wang W, Zhou Q, Dong Y, Tok E S and Yeo Y-C 2015 Critical thickness for strain relaxation of Ge1−xSnx ($x \leq 0.17$) grown by molecular beam epitaxy on Ge(001) *Appl. Phys. Lett.* **106** 232106

[40] Lin H, Chen R, Lu W, Huo Y, Kamins T I and Harris J S 2012 Structural and optical characterization of SixGe1−x−ySny alloys grown by molecular beam epitaxy *Appl. Phys. Lett.* **100** 141908

[41] Wallace P M, Senaratne C L, Xu C, Sims P E, Kouvetakis J and Menéndez J 2017 Molecular epitaxy of pseudomorphic Ge1-ySny(y= 0.06–0.17) structures and devices on Si/Ge at ultra-low temperatures via reactions of Ge4H10and SnD4 *Semicond. Sci. Technol.* **32** 025003

[42] Chen R, Gupta S, Huang Y-C, Huo Y, Rudy C W, Sanchez E, Kim Y, Kamins T I, Saraswat K C and Harris J S 2014 Demonstration of a Ge/GeSn/Ge Quantum-Well Microdisk Resonator on Silicon: Enabling High-Quality Ge(Sn) Materials for Micro- and Nanophotonics *Nano Lett.* **14** 37–43

[43] Dou W, Benamara M, Mosleh A, Margetis J, Grant P, Zhou Y, Al-Kabi S, Du W, Tolle J, Li B, Mortazavi M and Yu S-Q 2018 Investigation of GeSn Strain Relaxation and Spontaneous Composition Gradient for Low-Defect and High-Sn Alloy Growth *Sci Rep* **8** 5640

[44] von den Driesch N, Stange D, Wirths S, Rainko D, Povstugar I, Savenko A, Breuer U, Geiger R, Sigg H, Ikonic Z, Hartmann J-M, Grützmacher D, Mantl S and Buca D 2017 SiGeSn Ternaries for Efficient Group IV Heterostructure Light Emitters *Small* **13** 1603321

[45] Radamson H H, Noroozi M, Jamshidi A, Thompson P E and Östling M 2013 Strain Engineering in GeSnSi Materials *ECS Trans.* **50** 527

[46] Jiang L, Xu C, Gallagher J D, Favaro R, Aoki T, Menendez J and Kouvetakis J 2014 Development of light emitting group IV ternary alloys on Si platforms for long wavelength optoelectronic applications *Chemistry of Materials* **26** 2522–31

[47] Bogumilowicz Y, Hartmann J M, Truche R, Campidelli Y, Rolland G and Billon T 2004 Chemical vapour etching of Si, SiGe and Ge with HCl$\mathsemicolon$ applications to the formation of thin relaxed SiGe buffers and to the revelation of threading dislocations *Semicond. Sci. Technol.* **20** 127–34

[48] D'Costa V R, Fang Y-Y, Tolle J, Kouvetakis J and Menéndez J 2009 Tunable Optical Gap at a Fixed Lattice Constant in Group-IV Semiconductor Alloys *Phys. Rev. Lett.* **102** 107403

[49] Soref R A, Emelett S J and Buchwald W R 2006 Silicon waveguided components for the long-wave infrared region *Journal of Optics A: Pure and Applied Optics* **8** 840–8

[50] Sun G, Soref R A and Cheng H H 2010 Design of an electrically pumped SiGeSn/GeSn/SiGeSn double-heterostructure midinfrared laser *Journal of Applied Physics* **108** 033107

[51] Sun G, Soref R A and Cheng H H 2010 Design of a Si-based lattice-matched room-temperature GeSn/GeSiSn multi-quantum-well mid-infrared laser diode *Opt. Express, OE* **18** 19957–65

[52] Chang G-E, Chang S-W and Chuang S L 2010 Strain-Balanced $\rm Ge_z\rm Sn_1-z\hbox–\rm Si_x\rm Ge_y\rm Sn_1-x-y$ Multiple-Quantum-Well Lasers *IEEE Journal of Quantum Electronics* **46** 1813–20

[53] Gassenq A, Gencarelli F, Campenhout J V, Shimura Y, Loo R, Narcy G, Vincent B and Roelkens G 2012 GeSn/Ge heterostructure short-wave infrared photodetectors on silicon *Opt. Express, OE* **20** 27297–303

[54] Li H, Chang C, Chen T P, Cheng H H, Shi Z W and Chen H 2014 Characteristics of Sn segregation in Ge/GeSn heterostructures *Appl. Phys. Lett.* **105** 151906

[55] Chen J-Z, Li H, Cheng H H and Chang G-E 2014 Structural and optical characteristics of $Ge_{1-x}Sn_x$/Ge superlattices grown on Ge-buffered Si(001) wafers *Opt. Mater. Express, OME* **4** 1178–85

[56] Oehme M, Widmann D, Kostecki K, Zaumseil P, Schwartz B, Gollhofer M, Koerner R, Bechler S, Kittler M, Kasper E and Schulze J 2014 GeSn/Ge multiquantum well photodetectors on Si substrates *Opt. Lett., OL* **39** 4711–4

[57] Tonkikh A A, Eisenschmidt C, Talalaev V G, Zakharov N D, Schilling J, Schmidt G and Werner P 2013 Pseudomorphic GeSn/Ge(001) quantum wells: Examining indirect band gap bowing *Appl. Phys. Lett.* **103** 032106

[58] Schwartz B, Oehme M, Kostecki K, Widmann D, Gollhofer M, Koerner R, Bechler S, Fischer I A, Wendav T, Kasper E, Schulze J and Kittler M 2015 Electroluminescence of GeSn/Ge MQW LEDs on Si substrate *Opt. Lett., OL* **40** 3209–12

[59] Stange D, Driesch N von den, Rainko D, Schulte-Braucks C, Wirths S, Mussler G, Tiedemann A T, Stoica T, Hartmann J M, Ikonic Z, Mantl S, Grützmacher D and Buca D 2016 Study of GeSn based heterostructures: towards optimized group IV MQW LEDs *Opt. Express, OE* **24** 1358–67

[60] Olorunsola O, Ojo S, Abernathy G, Zhou Y, Amoah S, Grant P C, dou wei, Margetis J, Tolle J, Kuchuk A, Du W, Li B, Zhang Y-H and Yu S-Q (Fisher) 2021 Investigation of SiGeSn/GeSn/SiGeSn single quantum well with enhanced well emission *Nanotechnology*

[61] Anon Frontiers | Direct Growth of Ge1−xSnx Films on Si Using a Cold-Wall Ultra-High Vacuum Chemical-Vapor-Deposition System | Materials

[62] Margetis J, Mosleh A, Al-Kabi S, Ghetmiri S A, Du W, Dou W, Benamara M, Li B, Mortazavi M, Naseem H A, Yu S-Q and Tolle J 2017 Study of low-defect and strain-relaxed GeSn growth via reduced pressure CVD in H2 and N2 carrier gas *Journal of Crystal Growth* **463** 128–33

[63] Bragg W H 1913 The Reflection of X-Rays by Crystals *Nature* **91** 477–477

[64] Schreck M, Gsell S, Brescia R and Fischer M 2017 Ion bombardment induced buried lateral growth: the key mechanism for the synthesis of single crystal diamond wafers *Sci Rep* **7** 44462

[65] Krivoglaz M A 1969 *Theory of X-Ray and Thermal Neutron Scattering by Real Crystals* (Springer US)

[66] Daniš S and Holý V 2006 Diffuse x-ray scattering from misfit and threading dislocations in $\mathrm{Pb}\mathrm{Te}/\mathrm{Ba}{\mathrm{F}}_{2}/\mathrm{Si}(111)$ thin layers *Phys. Rev. B* **73** 014102

[67] Kaganer V M, Köhler R, Schmidbauer M, Opitz R and Jenichen B 1997 X-ray diffraction peaks due to misfit dislocations in heteroepitaxial structures *Phys. Rev. B* **55** 1793–810

[68] Kopp V, Kaganer V, Capellini G, Seta M D and Zaumseil P 2012 X-ray diffraction study of plastic relaxation in Ge-rich SiGe virtual substrates

[69] Binnig G and Rohrer H 1983 Scanning tunneling microscopy *Surface Science* **126** 236–44

[70] Scheel H J, Binning G and Rohrer H 1982 Atomically flat LPE-grown facets seen by scanning tunneling microscopy *Journal of Crystal Growth* **60** 199–202

[71] Binnig G K 1987 Atomic-Force Microscopy *Phys. Scr.* **T19A** 53–4

[72] Rajagopal S 2017 Identification of Probe of an Atomic Force Microscope Using Curve Fitting

[73] Soref R, Buca D and Yu S-Q 2016 Group IV Photonics: Driving Integrated Optoelectronics *Optics & Photonics News, OPN* **27** 32–9

[74] Jenkins null and Dow null 1987 Electronic properties of metastable GexSn *Phys Rev B Condens Matter* **36** 7994–8000

[75] D'Costa V R, Cook C S, Birdwell A G, Littler C L, Canonico M, Zollner S, Kouvetakis J and Menendez J 2006 Optical critical points of thin-film Ge1-y Sny alloys: A comparative Ge1-y Sny Ge1-x six study *Giant-magnetoresistance anomaly associated with a magnetization process in UFe4Al8* **73** 125207

[76] Alberi K, Blacksberg J, Bell L D, Nikzad S, Yu K M, Dubon O D and Walukiewicz W 2008 Band anticrossing in highly mismatched ${\mathrm{Sn}}_{x}{\mathrm{Ge}}_{1\ensuremath{-}x}$ semiconducting alloys *Phys. Rev. B* **77** 073202

[77] Soref R 2010 Mid-infrared photonics in silicon and germanium *Nature Photon* **4** 495–7

[78] Tseng H H, Wu K Y, Li H, Mashanov V, Cheng H H, Sun G and Soref R A 2013 Mid-infrared electroluminescence from a Ge/Ge0.922Sn0.078/Ge double heterostructure p-i-n diode on a Si substrate *Appl. Phys. Lett.* **102** 182106

[79] Gallagher J D, Senaratne C L, Wallace P M, Menéndez J and Kouvetakis J 2015 Electroluminescence from Ge1−ySny diodes with degenerate pn junctions *Appl. Phys. Lett.* **107** 123507

[80] Al-Kabi S, Ghetmiri S A, Margetis J, Pham T, Zhou Y, Dou W, Collier B, Quinde R, Du W, Mosleh A, Liu J, Sun G, Soref R A, Tolle J, Li B, Mortazavi M, Naseem H A and Yu S-Q 2016 An optically pumped 2.5 μm GeSn laser on Si operating at 110 K *Appl. Phys. Lett.* **109** 171105

[81] Reboud V, Gassenq A, Pauc N, Aubin J, Milord L, Thai Q M, Bertrand M, Guilloy K, Rouchon D, Rothman J, Zabel T, Armand Pilon F, Sigg H, Chelnokov A, Hartmann J M and Calvo V 2017 Optically pumped GeSn micro-disks with 16% Sn lasing at 3.1 μm up to 180 K *Appl. Phys. Lett.* **111** 092101

[82] Oehme M, Schmid M, Kaschel M, Gollhofer M, Widmann D, Kasper E and Schulze J 2012 GeSn p-i-n detectors integrated on Si with up to 4% Sn *Appl. Phys. Lett.* **101** 141110

[83] Zheng J, Liu Z, Xue C, Li C, Zuo Y, Cheng B and Wang Q 2018 Recent progress in GeSn growth and GeSn-based photonic devices *J. Semicond.* **39** 061006

[84] Rong H, Liu A, Jones R, Cohen O, Hak D, Nicolaescu R, Fang A and Paniccia M 2005 An all-silicon Raman laser *Nature* **433** 292–4

[85] Wirths S, Geiger R, von den Driesch N, Mussler G, Stoica T, Mantl S, Ikonic Z, Luysberg M, Chiussi S, Hartmann J M, Sigg H, Faist J, Buca D and Grützmacher D 2015 Lasing in direct-bandgap GeSn alloy grown on Si *Nature Photon* **9** 88–92

[86] Dou W, Ghetmiri S A, Al-Kabi S, Mosleh A, Zhou Y, Alharthi B, Du W, Margetis J, Tolle J, Kuchuk A, Benamara M, Li B, Naseem H A, Mortazavi M and Yu S-Q 2016 Structural and Optical Characteristics of GeSn Quantum Wells for Silicon-Based Mid-Infrared Optoelectronic Applications *Journal of Elec Materi* **45** 6265–72

[87] Ghetmiri S A, Zhou Y, Margetis J, Al-Kabi S, Dou W, Mosleh A, Du W, Kuchuk A, Liu J, Sun G, Soref R A, Tolle J, Naseem H A, Li B, Mortazavi M and Yu S-Q 2017 Study of a SiGeSn/GeSn/SiGeSn structure toward direct bandgap type-I quantum well for all group-IV optoelectronics *Opt. Lett., OL* **42** 387–90

[88] Du W, Ghetmiri S A, Margetis J, Al-Kabi S, Zhou Y, Liu J, Sun G, Soref R A, Tolle J, Li B, Mortazavi M and Yu S-Q 2017 Investigation of optical transitions in a SiGeSn/GeSn/SiGeSn single quantum well structure *Journal of Applied Physics* **122** 123102

[89] Margetis J, Zhou Y, Dou W, Grant P C, Alharthi B, Du W, Wadsworth A, Guo Q, Tran H, Ojo S, Abernathy G, Mosleh A, Ghetmiri S A, Thompson G B, Liu J, Sun G, Soref R, Tolle J, Li B, Mortazavi M and Yu S-Q 2018 All group-IV SiGeSn/GeSn/SiGeSn QW laser on Si operating up to 90 K *Appl. Phys. Lett.* **113** 221104

[90] Stange D, Driesch N von den, Rainko D, Roesgaard S, Povstugar I, Hartmann J-M, Stoica T, Ikonic Z, Mantl S, Grützmacher D and Buca D 2017 Short-wave infrared LEDs from GeSn/SiGeSn multiple quantum wells *Optica, OPTICA* **4** 185–8

[91] von den Driesch N, Stange D, Rainko D, Povstugar I, Zaumseil P, Capellini G, Schröder T, Denneulin T, Ikonic Z, Hartmann J, Sigg H, Mantl S, Grützmacher D and Buca D 2018 Advanced GeSn/SiGeSn Group IV Heterostructure Lasers *Adv Sci (Weinh)* **5** 1700955

[92] Stange D, von den Driesch N, Zabel T, Armand-Pilon F, Rainko D, Marzban B, Zaumseil P, Hartmann J-M, Ikonic Z, Capellini G, Mantl S, Sigg H, Witzens J, Grützmacher D and Buca D 2018 GeSn/SiGeSn heterostructure and multi quantum well lasers *ACS Photonics* 4628–36

[93] Mosleh A, Alher M, Du W, Cousar L C, Ghetmiri S A, Al-Kabi S, Dou W, Grant P C, Sun G, Soref R A, Li B, Naseem H A and Yu S-Q 2015 SiyGe1−x−ySnx films grown on Si using a cold-wall ultrahigh-vacuum chemical vapor deposition system *Journal of Vacuum Science & Technology B* **34** 011201

[94] Du W, Al-Kabi S, Ghetmiri S, Tran H, Pham T, Alharthi B, Mosleh A, Margetis J, Tolle J, Naseem H A, Mortazavi M, Sun G, Soref R, Li B and Yu S-Q 2016 (Invited) Development of SiGeSn Technique Towards Mid-Infrared Devices in Silicon Photonics *ECS Trans.* **75** 231

[95] Margetis J, Ghetmiri S, Du W, Conley B, Mosleh A, Soref R, Sun G, Domulevicz L, Naseem H, Yu S-Q and Tolle J 2014 Growth and Characterization of Epitaxial Ge1-XSnx Alloys and Heterostructures Using a Commercial CVD System

[96] Moontragoon P, Pengpit P, Burinprakhon T, Maensiri S, Vukmirovic N, Ikonic Z and Harrison P 2012 Electronic properties calculation of Ge1−x−ySixSny ternary alloy and nanostructure *Journal of Non-Crystalline Solids* **358** 2096–8

[97] Bourdon G, Robert I, Sagnes I and Abram I 2002 Spontaneous emission in highly excited semiconductors: Saturation of the radiative recombination rate *Journal of Applied Physics* **92** 6595–600

[98] Wirths S, Buca D and Mantl S 2016 Si–Ge–Sn alloys: From growth to applications *Progress in Crystal Growth and Characterization of Materials* **62** 1–39

[99] Wirths S, Buca D, Mussler G, Tiedemann A T, Holländer B, Bernardy P, Stoica T, Grützmacher D and Mantl S 2013 Reduced Pressure CVD Growth of Ge and Ge1−xSnx Alloys *ECS J. Solid State Sci. Technol.* **2** N99

[100] Zhao Y, Zhang Y-H, Bertoni M, King R, Holman Z, and Arizona State University 2016 The Design and Demonstration of Monocrystalline CdTe/MgCdTe Double-Heterostructure Solar Cells *ASU Electronic Theses and Dissertations* (Arizona State University)

[101] Schnitzer I, Yablonovitch E, Caneau C and Gmitter T J 1993 Ultrahigh spontaneous emission quantum efficiency, 99.7% internally and 72% externally, from AlGaAs/GaAs/AlGaAs double heterostructures *Appl. Phys. Lett.* **62** 131–3

[102] Anon Optical enhancement of the open-circuit voltage in high quality GaAs solar cells: Journal of Applied Physics: Vol 113, No 12

[103] Tran H, Du W, Ghetmiri S A, Mosleh A, Sun G, Soref R A, Margetis J, Tolle J, Li B, Naseem H A and Yu S-Q 2016 Systematic study of Ge1−xSnx absorption coefficient and refractive index for the device applications of Si-based optoelectronics *Journal of Applied Physics* **119** 103106

[104] Wang J-B, Ding D, Johnson S R, Yu S-Q and Zhang Y-H 2007 Determination and improvement of spontaneous emission quantum efficiency in GaAs/AlGaAs heterostructures grown by molecular beam epitaxy *physica status solidi (b)* **244** 2740–51

[105] Centurioni E 2005 Generalized matrix method for calculation of internal light energy flux in mixed coherent and incoherent multilayers *Appl. Opt., AO* **44** 7532–9

[106] Liu S, Zhang Y-H, Johnson S R, Vasileska D, Yu H, and Arizona State University 2015 Towards High-Efficiency Thin-Film Solar Cells: from Theoretical Analysis to Experimental Exploration *ASU Electronic Theses and Dissertations* (Arizona State University)

[107] Anon A semi-analytical model for semiconductor solar cells: Journal of Applied Physics: Vol 110, No 12

[108] Chang Y, Tan I, Zhang Y, Bimberg D, Merz J and Hu E 1993 Reduced quantum efficiency of a near-surface quantum well *Journal of Applied Physics* **74** 5144–8

[109] Andersson J Y and Lundqvist L 1991 Near-unity quantum efficiency of AlGaAs/GaAs quantum well infrared detectors using a waveguide with a doubly periodic grating coupler *Appl. Phys. Lett.* **59** 857–9

[110] Mosleh A, Alher M A, Cousar L, Abusafe H, Dou W, Grant P, Al-Kabi S, Ghetmiri S A, Alharthi B, Tran H, Du W, Benamara M, Li B, Mortazavi M, Yu S-Q and Naseem H A 2015 Enhancement of Material Quality of (Si)GeSn Films Grown by SnCl4 Precursor *ECS Trans.* **69** 279

[111] Toko K, Yoshimine R, Moto K and Suemasu T 2017 High-hole mobility polycrystalline Ge on an insulator formed by controlling precursor atomic density for solid-phase crystallization *Sci Rep* **7** 16981

[112] Grant P C, Margetis J, Zhou Y, Dou W, Abernathy G, Kuchuk A, Du W, Li B, Tolle J, Liu J, Sun G, Soref R A, Mortazavi M and Yu S-Q 2018 Direct bandgap type-I GeSn/GeSn quantum well on a GeSn- and Ge- buffered Si substrate *AIP Advances* **8** 025104

[113] Oehme M, Werner J, Gollhofer M, Schmid M, Kaschel M, Kasper E and Schulze J 2011 Room-Temperature Electroluminescence From GeSn Light-Emitting Pin Diodes on Si *IEEE Photonics Technology Letters* **23** 1751–3

[114] Zhou Y, Dou W, Du W, Pham T, Ghetmiri S A, Al-Kabi S, Mosleh A, Alher M, Margetis J, Tolle J, Sun G, Soref R, Li B, Mortazavi M, Naseem H and Yu S-Q 2016 Systematic study of GeSn heterostructure-based light-emitting diodes towards mid-infrared applications *Journal of Applied Physics* **120** 023102

[115] Wirths S, Geiger R, Ikonic Z, Tiedemann A T, Mussler G, Hartmann J-M, Mantl S, Sigg H, Grützmacher D and Buca D 2014 Epitaxy and photoluminescence studies of high quality GeSn heterostructures with Sn concentrations up to 13 at.% *11th International Conference on Group IV Photonics (GFP)* 11th International Conference on Group IV Photonics (GFP) pp 15–6

[116] Senaratne C L, Gallagher J D, Aoki T, Kouvetakis J and Menéndez J 2014 Advances in Light Emission from Group-IV Alloys via Lattice Engineering and n-Type Doping Based on Custom-Designed Chemistries *Chem. Mater.* **26** 6033–41

[117] Huang Y-H, Chang G-E, Li H and Cheng H H 2017 Sn-based waveguide p-i-n photodetector with strained GeSn/Ge multiple-quantum-well active layer *Opt. Lett., OL* **42** 1652–5

[118] Zheng J, Wang S, Cong H, Fenrich C S, Liu Z, Xue C, Li C, Zuo Y, Cheng B, Harris J S and Wang Q 2017 Characterization of a $Ge_{1-x-y}Si_ySn_x/Ge_{1-x}Sn_x$ multiple quantum well structure grown by sputtering epitaxy *Opt. Lett., OL* **42** 1608–11

[119] Grant P C, Margetis J, Du W, Zhou Y, Dou W, Abernathy G, Kuchuk A, Li B, Tolle J, Liu J, Sun G, Soref R A, Mortazavi M and Yu S-Q 2018 Study of direct bandgap type-I GeSn/GeSn double quantum well with improved carrier confinement *Nanotechnology* **29** 465201

[120] Oehme M, Kostecki K, Arguirov T, Mussler G, Ye K, Gollhofer M, Schmid M, Kaschel M, Körner R A, Kittler M, Buca D, Kasper E and Schulze J 2014 GeSn Heterojunction LEDs on Si Substrates *IEEE Photonics Technology Letters* **26** 187–9

[121] Oehme M, Kostecki K, Schmid M, Oliveira F, Kasper E and Schulze J 2014 Epitaxial growth of strained and unstrained GeSn alloys up to 25% Sn *Thin Solid Films* **557** 169–72

[122] Talamas Simola E, Kiyek V, Ballabio A, Schlykow V, Frigerio J, Zucchetti C, De Iacovo A, Colace L, Yamamoto Y, Capellini G, Grützmacher D, Buca D and Isella G 2021 CMOS-Compatible Bias-Tunable Dual-Band Detector Based on GeSn/Ge/Si Coupled Photodiodes *ACS Photonics* **8** 2166–73

[123] Anon GeSn lasers for CMOS integration | IEEE Conference Publication | IEEE Xplore

[124] Tseng H H, Wu K Y, Li H, Mashanov V, Cheng H H, Sun G and Soref R A 2013 Mid-infrared electroluminescence from a Ge/Ge0.922Sn0.078/Ge double heterostructure p-i-n diode on a Si substrate *Appl. Phys. Lett.* **102** 182106

[125] Du W, Zhou Y, Ghetmiri S A, Mosleh A, Conley B R, Nazzal A, Soref R A, Sun G, Tolle J, Margetis J, Naseem H A and Yu S-Q 2014 Room-temperature electroluminescence from Ge/Ge1-xSnx/Ge diodes on Si substrates *Appl. Phys. Lett.* **104** 241110

[126] Tseng H H, Li H, Mashanov V, Yang Y J, Cheng H H, Chang G E, Soref R A and Sun G 2013 GeSn-based p-i-n photodiodes with strained active layer on a Si wafer *Appl. Phys. Lett.* **103** 231907

[127] Kondratenko S V, Hyrka Yu V, Mazur Yu I, Kuchuk A V, Dou W, Tran H, Margetis J, Tolle J, Yu S-Q and Salamo G J 2019 Photovoltage spectroscopy of direct and indirect bandgaps of strained Ge1-xSnx thin films on a Ge/Si(001) substrate *Acta Materialia* **171** 40–7

[128] Ghetmiri S A, Du W, Conley B R, Mosleh A, Nazzal A, Sun G, Soref R A, Margetis J, Tolle J, Naseem H A and Yu S-Q 2014 Shortwave-infrared photoluminescence from Ge1−xSnx thin films on silicon *Journal of Vacuum Science & Technology B* **32** 060601

[129] Tonkikh A A, Zakharov N D, Suvorova A A, Eisenschmidt C, Schilling J and Werner P 2014 Cubic Phase Sn-Rich GeSn Nanocrystals in a Ge Matrix *Crystal Growth & Design* **14** 1617–22

[130] Wirths S, Buca D, Ikonic Z, Harrison P, Tiedemann A T, Holländer B, Stoica T, Mussler G, Breuer U, Hartmann J M, Grützmacher D and Mantl S 2014 SiGeSn growth studies using reduced pressure chemical vapor deposition towards optoelectronic applications *Thin Solid Films* **557** 183–7

[131] Mosleh A, Alher M, Cousar L C, Du W, Ghetmiri S A, Al-Kabi S, Dou W, Grant P C, Sun G, Soref R A, Li B, Naseem H A and Yu S-Q 2016 Buffer-Free GeSn and SiGeSn Growth on Si Substrate Using In Situ SnD4 Gas Mixing *Journal of Electronic Materials* **45** 2051–8

[132] Harris T R, Ryu M-Y, Yeo Y K, Wang B, Senaratne C L and Kouvetakis J 2016 Direct bandgap cross-over point of Ge1-ySny grown on Si estimated through temperature-dependent photoluminescence studies *Journal of Applied Physics* **120** 085706

[133] Stange D, Wirths S, von den Driesch N, Mussler G, Stoica T, Ikonic Z, Hartmann J M, Mantl S, Grützmacher D and Buca D 2015 Optical Transitions in Direct-Bandgap $Ge_{1-x}Sn_x$ Alloys *ACS Photonics* **2** 1539–45

[134] Stanchu H V, Kuchuk A V, Mazur Y I, Pandey K, de Oliveira F M, Benamara M, Teodoro M D, Yu S-Q and Salamo G J 2021 Quantitative Correlation Study of Dislocation Generation, Strain Relief, and Sn Outdiffusion in Thermally Annealed GeSn Epilayers *Crystal Growth & Design* **21** 1666–73

[135] Anon Tensile strained epitaxial Ge films on Si(100) substrates with potential application in L-band telecommunications: Applied Physics Letters: Vol 84, No 6

[136] Stanchu H, Kuchuk A V, Mazur Y I, Margetis J, Tolle J, Richter J, Yu S-Q and Salamo G J 2020 X-ray diffraction study of strain relaxation, spontaneous compositional gradient, and dislocation density in GeSn/Ge/Si(100) heterostructures *Semiconductor Science and Technology* **35** 075009

[137] de Kersauson M, Jakomin R, El Kurdi M, Beaudoin G, Zerounian N, Aniel F, Sauvage S, Sagnes I and Boucaud P 2010 Direct and indirect band gap room temperature electroluminescence of Ge diodes *Journal of Applied Physics* **108** 023105

[138] Sun X, Liu J, Kimerling L C and Michel J 2009 Direct gap photoluminescence of n-type tensile-strained Ge-on-Si *Appl. Phys. Lett.* **95** 011911

[139] Pezzoli F, Giorgioni A, Patchett D and Myronov M 2016 Temperature-Dependent Photoluminescence Characteristics of GeSn Epitaxial Layers *ACS Photonics* **3** 2004–9

[140] Zelazna K, Wełna M, Misiewicz J, Dekoster J and Kudrawiec R 2016 Temperature dependence of energy gap of Ge1−xSnx alloys with x < 0.11 studied by photoreflectance *J. Phys. D: Appl. Phys.* **49** 235301

[141] Matthews J W and Blakeslee A E 1974 Defects in epitaxial multilayers: I. Misfit dislocations *Journal of Crystal Growth* **27** 118–25

[142] People R and Bean J C 1985 Calculation of critical layer thickness versus lattice mismatch for GexSi1−x/Si strained-layer heterostructures *Appl. Phys. Lett.* **47** 322–4

[143] Mosleh A, Alher M A, Cousar L C, Du W, Ghetmiri S A, Pham T, Grant J M, Sun G, Soref R A, Li B, Naseem H A and Yu S-Q 2015 Direct Growth of Ge1−xSnx Films on Si Using a Cold-Wall Ultra-High Vacuum Chemical-Vapor-Deposition System *Frontiers in Materials* **2** 30

[144] Margetis J, Yu S-Q, Bhargava N, Li B, Du W and Tolle J 2017 Strain engineering in epitaxial Ge1-xSnx: a path towards low-defect and high Sn-content layers *Semicond. Sci. Technol.* **32** 124006

[145] Anon Study of low-defect and strain-relaxed GeSn growth via reduced pressure CVD in H2 and N2 carrier gas

[146] von den Driesch N, Stange D, Rainko D, Breuer U, Capellini G, Hartmann J-M, Sigg H, Mantl S, Grützmacher D and Buca D 2019 Epitaxy of Si-Ge-Sn-based heterostructures for CMOS-integratable light emitters *Solid-State Electronics* **155** 139–43

[147] Zaumseil P, Hou Y, Schubert M A, von den Driesch N, Stange D, Rainko D, Virgilio M, Buca D and Capellini G 2018 The thermal stability of epitaxial GeSn layers *APL Materials* **6** 076108

[148] Nicolas J, Assali S, Mukherjee S, Lotnyk A and Moutanabbir O 2020 Dislocation Pipe Diffusion and Solute Segregation during the Growth of Metastable GeSn *Crystal Growth & Design* **20** 3493–8

[149] Olorunsola O, Stanchu H, Ojo S, Pandey K, Said A, Margetis J, Tolle J, Kuchuk A, Mazur Y I, Salamo G and Yu S-Q 2021 Impact of Long-Term Annealing on Photoluminescence from Ge1−xSnx Alloys *Crystals* **11** 905

[150] von den Driesch N, Wirths S, Troitsch R, Mussler G, Breuer U, Moutanabbir O, Grützmacher D and Buca D 2020 Thermally activated diffusion and lattice relaxation in (Si)GeSn materials *Phys. Rev. Materials* **4** 033604

[151] Cannon D D, Liu J, Ishikawa Y, Wada K, Danielson D T, Jongthammanurak S, Michel J and Kimerling L C 2004 Tensile strained epitaxial Ge films on Si(100) substrates with potential application in L-band telecommunications *Appl. Phys. Lett.* **84** 906–8

[152] Hartmann J M, Abbadie A, Papon A M, Holliger P, Rolland G, Billon T, Fédéli J M, Rouvière M, Vivien L and Laval S 2004 Reduced pressure–chemical vapor deposition of Ge thick layers on Si(001) for 1.3–1.55-μm photodetection *Journal of Applied Physics* **95** 5905–13

[153] Stanchu H V, Kuchuk A V, Mazur Y I, Margetis J, Tolle J, Yu S-Q and Salamo G J 2020 Strain suppressed Sn incorporation in GeSn epitaxially grown on Ge/Si(001) substrate *Appl. Phys. Lett.* **116** 232101

[154] Fitzgerald E A 1989 The effect of substrate growth area on misfit and threading dislocation densities in mismatched heterostructures *Journal of Vacuum Science & Technology B: Microelectronics Processing and Phenomena* **7** 782–8

[155] Albrecht M, Christiansen S, Michler J, Dorsch W, Strunk H P, Hansson P O and Bauser E 1995 Surface ripples, crosshatch pattern, and dislocation formation: Cooperating mechanisms in lattice mismatch relaxation *Appl. Phys. Lett.* **67** 1232–4

[156] Béal R 2015 Laser induced quantum well intermixing : reproducibility study and fabrication of superluminescent diodes *undefined*

[157] Chen Q, Wu S, Zhang L, Fan W and Tan C S 2021 Simulation of High-Efficiency Resonant-Cavity-Enhanced GeSn Single-Photon Avalanche Photodiodes for Sensing and Optical Quantum Applications *IEEE Sensors Journal* **21** 14789–98

[158] Imbrenda D, Hickey R, Carrasco R A, Fernando N S, VanDerslice J, Zollner S and Kolodzey J 2018 Infrared dielectric response, index of refraction, and absorption of germanium-tin alloys with tin contents up to 27% deposited by molecular beam epitaxy *Appl. Phys. Lett.* **113** 122104

[159] Rakels J H 1996 Influence of the surface height distribution on the total integrated scatter (TIS) formula *Nanotechnology* **7** 43–6

[160] Rim K, Hoyt J L and Gibbons J F 2000 Fabrication and analysis of deep submicron strained-Si n-MOSFET's *IEEE Transactions on Electron Devices* **47** 1406–15

[161] Shimokawa R, Yamanaka M and Sakata I 2007 Very Low Temperature Epitaxial Growth of Silicon Films for Solar Cells *Jpn. J. Appl. Phys.* **46** 7612

[162] Mosleh A, Ghetmiri S A, Conley B R, Abu-Safe H H, Benamara M, Waqar Z, El-Ghazaly S, Yu S-Q and Naseem H A 2014 Investigation of Growth Mechanism and Role of H2 in Very Low Temperature Si Epitaxy *ECS Trans.* **64** 967–75

[163] Anon Fundamentals of semiconductor fabrication (Book, 2004) [WorldCat.org]

[164] Finch R H, Queisser H J, Thomas G and Washburn J 1963 Structure and Origin of Stacking Faults in Epitaxial Silicon *Journal of Applied Physics* **34** 406–15

[165] Szekeres A, Nikolova T, Simeonov S, Gushterov A, Hamelmann F and Heinzmann U 2006 Plasma-assisted chemical vapor deposited silicon oxynitride as an alternative material for gate dielectric in MOS devices *Microelectronics Journal* **37** 64–70

[166] Moreno M and Cabarrocas P R i 2010 Ultra-thin crystalline silicon films produced by plasma assisted epitaxial growth on silicon wafers and their transfer to foreign substrates *EPJ Photovolt.* **1** 10301

[167] Bray K R, Gupta A and Parsons G N 2002 Effect of hydrogen on adsorbed precursor diffusion kinetics during hydrogenated amorphous silicon deposition *Appl. Phys. Lett.* **80** 2356–8

[168] Rosenblad C, Känel H von, Kummer M, Dommann A and Müller E 2000 A plasma process for ultrafast deposition of SiGe graded buffer layers *Applied Physics Letters* **76** 427

[169] Rużyłło J 2004 *Cleaning Technology in Semiconductor Device Manufacturing VIII: Proceedings of the International Symposium* (The Electrochemical Society)

[170] Suzuki S, Takai H, Okuda H and Itoh T 1980 Silicon Epitaxy by Plasma Dissociation of Silane *Jpn. J. Appl. Phys.* **19** 647

[171] Gupta A, Yang H and Parsons G N 2002 Ab initio analysis of silyl precursor physisorption and hydrogen abstraction during low temperature silicon deposition *Surface Science* **496** 307–17

[172] Raviswaran A, Liu C-P, Kim J, Cahill D G and Gibson J M 2001 Evolution of coherent islands during strained-layer Volmer-Weber growth of Si on Ge(111) *Phys. Rev. B* **63** 125314

[173] Marée P M J, Nakagawa K, Mulders F M, van der Veen J F and Kavanagh K L 1987 Thin epitaxial Ge−Si(111) films: Study and control of morphology *Surface Science* **191** 305–28

[174] Venables J 2000 *Introduction to Surface and Thin Film Processes* (Cambridge University Press)

[175] Teplin C W, Iwaniczko E, To B, Moutinho H, Stradins P and Branz H M 2006 Breakdown physics of low-temperature silicon epitaxy grown from silane radicals *Phys. Rev. B* **74** 235428

[176] Yu S Q, Ghetmiri S A, Du W, Margetis J, Zhou Y, Mosleh A, Al-Kabi S, Nazzal A, Sun G, Soref R A, Tolle J, Li B and Naseem H A 2015 Si based GeSn light emitter: mid-infrared devices in Si photonics **9367** 93670R

[177] Tran H, Pham T, Margetis J, Zhou Y, Dou W, Grant P C, Grant J M, Al-Kabi S, Sun G, Soref R A, Tolle J, Zhang Y-H, Du W, Li B, Mortazavi M and Yu S-Q 2019 Si-Based GeSn Photodetectors toward Mid-Infrared Imaging Applications *ACS Photonics* **6** 2807–15

[178] Gurdal O, Desjardins P, Carlsson J R A, Taylor N, Radamson H H, Sundgren J-E and Greene J E 1998 Low-temperature growth and critical epitaxial thicknesses of fully strained metastable Ge1−xSnx (x≲0.26) alloys on Ge(001)2×1 *Journal of Applied Physics* **83** 162–70

[179] Chen R, Lin H, Huo Y, Hitzman C, Kamins T I and Harris J S 2011 Increased photoluminescence of strain-reduced, high-Sn composition Ge1−xSnx alloys grown by molecular beam epitaxy *Appl. Phys. Lett.* **99** 181125

[180] Tao P, Huang L, Cheng H H, Wang H-H and Wu X-S 2014 Epitaxial growth of Ge 1– x Sn x films with x up to 0.14 grown on Ge (00l) at low temperature *Chinese Phys. B* **23** 088112

[181] Kouvetakis J and G. Chizmeshya A V 2007 New classes of Si-based photonic materials and device architectures via designer molecular routes *Journal of Materials Chemistry* **17** 1649–55

[182] Vincent B, Gencarelli F, Bender H, Merckling C, Douhard B, Petersen D H, Hansen O, Henrichsen H H, Meersschaut J, Vandervorst W, Heyns M, Loo R and Caymax M 2011 Undoped and in-situ B doped GeSn epitaxial growth on Ge by atmospheric pressure-chemical vapor deposition *Appl. Phys. Lett.* **99** 152103

[183] Loo R, Shimura Y, Ike S, Vohra A, Stoica T, Stange D, Buca D, Kohen D, Margetis J and Tolle J 2018 Epitaxial GeSn: impact of process conditions on material quality *Semicond. Sci. Technol.* **33** 114010

[184] Assali S, Attiaoui A, Atalla M R M, Dijkstra A, Kumar A, Mukherjee S, Abdi S and Moutanabbir O 2020 Epitaxial GeSn and its integration in MIR Optoelectronics *Conference on Lasers and Electro-Optics (2020), paper SM3M.2* CLEO: Science and Innovations (Optical Society of America) p SM3M.2

[185] Grant P C, Dou W, Alharthi B, Grant J M, Tran H, Abernathy G, Mosleh A, Du W, Li B, Mortazavi M, Naseem H A and Yu S-Q 2019 UHV-CVD growth of high quality GeSn

using $SnCl_4$: from material growth development to prototype devices *Opt. Mater. Express* **9** 3277

[186] Mosleh A, Ghetmiri S A, Conley B R, Hawkridge M, Benamara M, Nazzal A, Tolle J, Yu S-Q and Naseem H A 2014 Material Characterization of Ge1−xSnxAlloys Grown by a Commercial CVD System for Optoelectronic Device Applications *Journal of Elec Materi* **43** 938–46

[187] Dou W 2018 High-Sn-content GeSn Alloy towards Room-temperature Mid Infrared Laser *Graduate Theses and Dissertations*

[188] Chang G-E, Chang S-W and Chuang S L 2010 Strain-Balanced $${$$\backslash$rm Ge$}$ _ ${$z$}$${$$\backslash$rm Sn$}$ _ ${$1-z$}$$\backslash$hbox ${$–$}$${$$\backslash$rm Si$}$ _ ${$x$}$${$$\backslash$rm Ge$}$ _ ${$y$}$${$$\backslash$rm Sn$}$ _ ${$1-xy$}$ $ Multiple-Quantum-Well Lasers *IEEE journal of Quantum Electronics* **46** 1813–20

[189] Beeler R, Roucka R, Chizmeshya A V G, Kouvetakis J and Menéndez J 2011 Nonlinear structure-composition relationships in the Ge 1 − y Sn y /Si(100) (y < 0.15) system *Physical Review B* **84** 035204

[190] Fitzgerald E A 1995 GeSijSi NANOSTRUCTURES *Annu. Rev. Mater. Sci* **25** 417–54

[191] Martins J L and Zunger A 1984 Bond lengths around isovalent impurities and in semiconductor solid solutions *Physical Review B* **30** 6217–20

[192] Xie J, Chizmeshya A V G, Tolle J, D'Costa V R, Menendez J and Kouvetakis J 2010 Synthesis, Stability Range, and Fundamental Properties of Si−Ge−Sn Semiconductors Grown Directly on Si(100) and Ge(100) Platforms *Chemistry of Materials* **22** 3779–89

[193] Chen Z, Ikonic Z, Indjin D and Kelsall R W 2021 Design optimization of tensile-strained SiGeSn/GeSn quantum wells at room temperature *Journal of Applied Physics* **129** 123102

Appendix A Band structure material parameters used in this dissertation

Table A1. Structural and optical parameters used in calculation the band structures[187].

Parameters	Ge	Sn
Lattice constant a (nm)	0.56573[188]	0.64892[188]
Bowing parameter b (nm)	-0.0066[189]	
Effective mass m_c (m0)	0.038[188]	0.058[188]
Effective mass $m_{t,L}$ (m0)	0.0807[188]	0.075[188]
Effective mass $m_{l,L}$ (m0)	1.57[188]	1.478[188]
Luttinger's parameters γ_1	13.38[188]	-14.97[188]
Luttinger's parameters γ_2	4.24[188]	-10.61[188]
Luttinger's parameters γ_3	5.69[188]	-8.52[188]
Bandgap E_g^{Γ} (eV)	0.7985[188]	-0.413[188]
Bandgap E_g^{L} (eV)	0.664[188]	0.092[188]
Deformation potentials a_c (eV)	-8.24[188]	-6[188]
Deformation potentials a_L (eV)	-1.54[188]	-2.14[188]
Deformation potentials a_v (eV)	1.24[188]	1.58[188]
Deformation potentials b_v (eV)	-2.9[188]	-2.7[188]
Elastic constants C_{11} (GPa)	128.53[188]	69.00[188]
Elastic constants C_{12} (GPa)	48.26[188]	29.30[188]
Elastic constants C_{44} (GPa)	68.30[188]	36.20[188]
Calculated Poisson ratio $\boldsymbol{v = \frac{C_{12}}{C_{11} + C_{12}}}$	0.27	0.30
Shear modulus μ (GPa)**[190]** $\boldsymbol{\mu = C_{44} - \frac{(2C_{44} + C_{12} - C_{11})}{3}}$	49.52	25.30
Interaction parameter α (eV)	0.27[191][192]	

(Si)GeSn band structure review

The band parameters of SiGeSn alloys and their dependence on alloy composition are significant device parameters. However, investigations of many device parameters have been obstructed by a lack of definite knowledge of various material parameters. This appendix provides a database on the fundamental material properties of SiGeSn ternary, which eases the design of the devices from the bulk to the quantum well (QW) structures. The model applied here is based on an interpolation scheme and therefore, entails that those values of the material parameters for the related elements are known. This appendix also presents a comparison between our previous review of SiGeSn band parameters and a recent review from Chen *et al.* [193]. The comparison helps us to enrich our comprehension of SiGeSn band parameters. Moreover, it is necessary to experimentally verify the database by studying different structures such as bulk and QW.

Table A2. The constituent values of Si, Ge, and Sn

Parameter	Symbol	Ref. **[193]**			Our previous review		
		Si	Ge	Sn	Si	Ge	Sn
Pikus-Bir DP	a_c (eV)	-10.06	-8.24	-6	-10.06	-8.24	-6
Pikus-Bir DP	a_v (eV)	2.46	1.24	1.58	2.46	1.24	1.58
Pikus-Bir DP	b (eV)	-2.1	-2.9	-2.7	-2.1	-2.9	-2.7
Pikus-Bir DP	d (eV)	-5.3	-4.8	-4.1	NA	NA	NA
L-valley DP	a_L (eV)	-0.66	-1.54	-2.14	-0.66	-1.54	-2.14
Stiffness Constant	C_{11} (GPa)	165.77	128.53	69	165.77	128.53	69
Stiffness Constant	C_{12} (Gpa)	63.93	48.26	29.3	63.93	48.26	29.3
Stiffness Constant	C_{44} (Gpa)	79.51	66.7	36.2	NA	NA	NA

Parameter	Symbol	Ref. [193]			Our previous review		
		Si	Ge	Sn	Si	Ge	Sn
Refractive Index	n_r	3.4	4	6.18	NA	NA	NA
Lattice Constant	a_{lat} (Å)	5.4307	5.6579	6.489	5.4307	5.6573	6.4892
Bandgap (L)	$E_g^L(eV)$	2.716	0.74	0.1	1.65	0.744	0.092
Split-off energy	$\Delta_{SO}(eV)$	0.044	0.26	0.6	0.044	0.29	0.8
Luttinger	γ_1	4.285	13.38	-12	4.22	NA	NA
Luttinger	γ_2	0.339	4.24	-8.45	0.39	NA	NA
Luttinger	γ_3	1.446	5.69	-6.84	NA	NA	NA
Momentum energy	$E_p(eV)$	21.6	26.3	23.8	NA	NA	NA
Valence band offset	$E_v(eV)$	-1.86	-0.91	0	NA	NA	NA
Effective mass (Γ)	m_e^Γ	0.188	0.038	-0.058	0.528	0.038	0.058
Longitudinal effective mass (L)	m_l^L	1.418	1.61	1.478	1.659	1.57	1.478
Transverse effective mass (L)	m_t^L	0.13	0.081	0.075	0.133	0.807	0.075

Table A3. Bowing parameters.

Parameter	Symbol	Ref. [1]			Our previous review		
		SiGe	SiSn	GeSn	SiGe	SiSn	GeSn
Bowing for lattice constant	$B_{a_{lat}}$	0.026	0	-0.041	0.026	0	-0.166
Bowing for bandgap $(\boldsymbol{\Gamma})$	$B_{E_g^\Gamma}$	NA	NA	NA	0.21	3.915	2.24
Bowing for bandgap $(\boldsymbol{L})$	$B_{E_g^L}$	NA	NA	NA	0.335	2.124	0.68

Appendix B

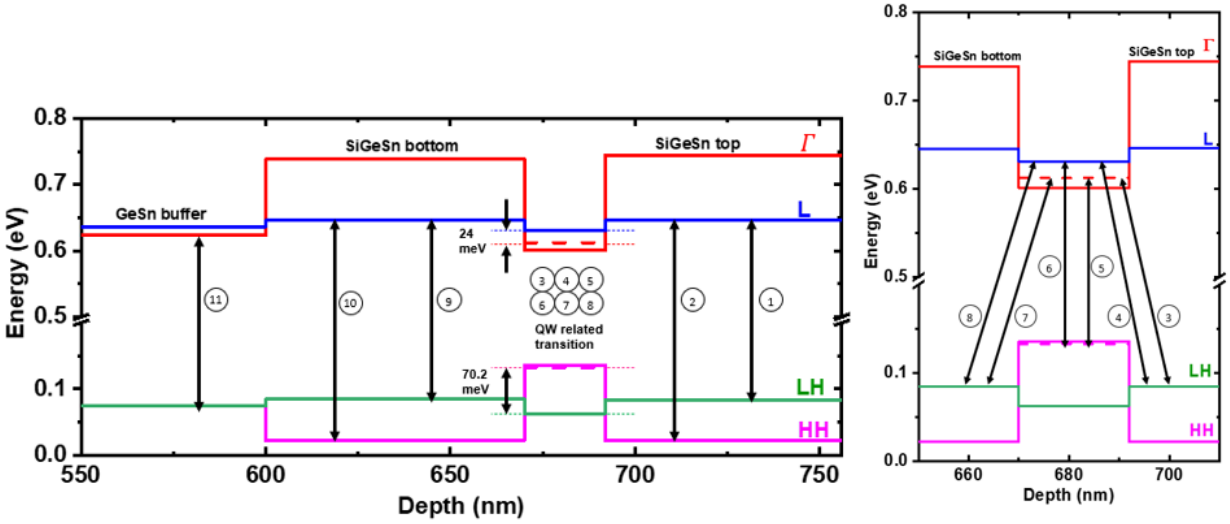

Figure B2. Thicker well 22 nm in well) band diagram and possible optical transition.

Table B1. Detailed summary of all possible transitions and their corresponding energies

	Possible Transitions	Energy (meV)
QW	⑤ **Γ – HH**	**481**
	⑥ **L – HH**	**498**
QW-related (Type II)	③ Γ (QW) – LH (SiGeSn top)	528
	⑦ Γ (QW) – LH (SiGeSn bottom)	528
QW-related (Type II)	④ L (QW) – LH (SiGeSn top)	546
	⑧ L (QW) – LH (SiGeSn bottom)	546
GeSn buffer	⑪ Γ – HH	549
SiGeSn top	① L – LH	562
SiGeSn bottom	⑨ L – LH	562
SiGeSn top	② L – HH	625
SiGeSn bottom	⑩ L – HH	625

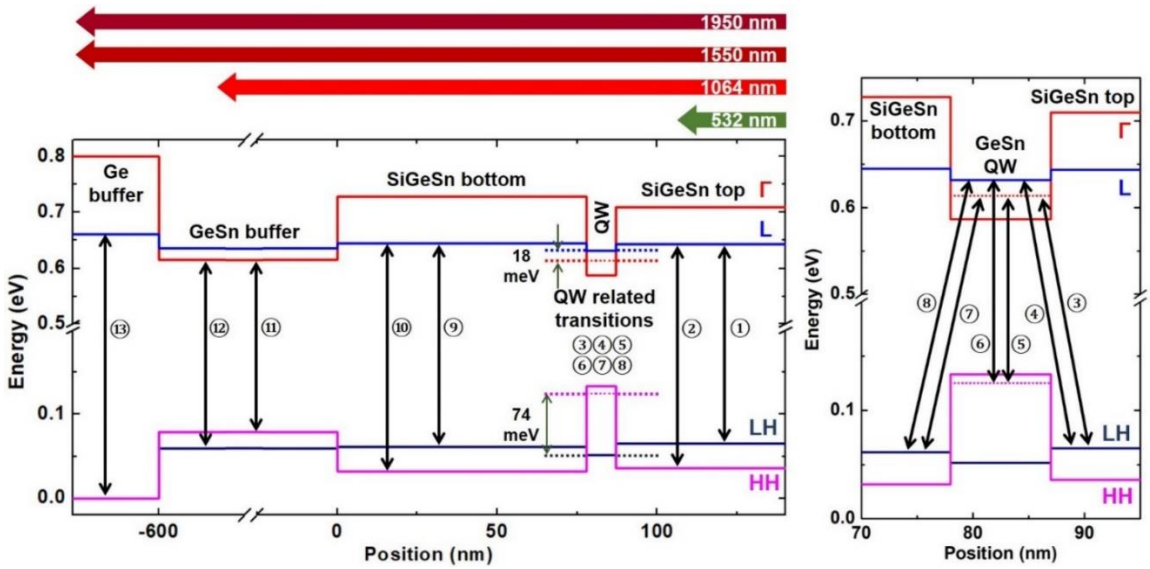

Figure B2. Thinner well (9 nm in well) band diagram and possible optical transition [24].

Table B2. Detailed summary of all possible transitions and their corresponding energies [24]

	Possible Transitions	Energy (meV)
QW	⑤ Γ – HH	**489**
	⑥ L – HH	**507**
GeSn buffer	⑪ Γ – HH	536
QW-related (Type II)	③ Γ (QW) – LH (SiGeSn top)	549
	⑦ Γ (QW) – LH (SiGeSn bottom)	552
GeSn buffer	⑫ Γ – LH	556
QW-related (Type II)	④ L (QW) – LH (SiGeSn top)	567
	⑧ L (QW) – LH (SiGeSn bottom)	570
SiGeSn top	① L – LH	579
SiGeSn bottom	⑨ L – LH	583
SiGeSn top	② L – HH	608
SiGeSn bottom	⑩ L – HH	613
Ge buffer	*⑬ L – HH/LH*	*660*

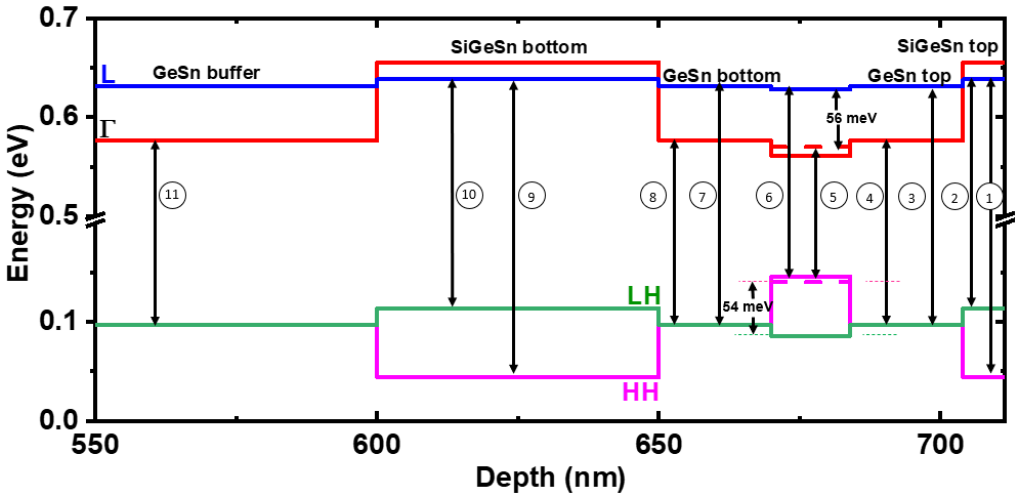

Figure B3. SCH structure band diagram and possible optical transition.

Table B3. Detailed summary of all possible transitions and their corresponding energies

Layer	Transition Type	Transition ID	Energy (meV)
SiGeSn Top	L-HH	①	592
	L-LH	②	524
GeSn Top	L-HH/LH	③	534
	Γ-HH/LH	④	479
QW	**Γ-HH**	⑤	**437**
	L-HH	⑥	**488**
GeSn bottom	L-HH/LH	⑦	534
	Γ-HH/LH	⑧	479
SiGeSn bottom	L-HH	⑨	595
	L-LH	⑩	524
Ge buffer	Γ-LH	⑪	479

Appendix C: Description of Research for Popular Publication

The digital age has met a retinue of technological breakthroughs; from the enterprise realities of machine learning and artificial intelligence to the application of cloud computing, a new revolution at innovation is reached, as both the unthinkable and the unimaginable continues to find way into the ruggedness of the wild and the comforts of our work-from-home remote spaces. But for the simultaneous advancements in electronics and optical technologies, many theoretical concepts of computer science and advanced statistics would have remained a relic of texts. Thanks to the modern practicalities of nanotechnology, photonics and optoelectronics!

Today, with the realizations of advanced optoelectronics, what was once a consumer non-reality is fast becoming commonplace in our society. In fact, it is practically possible to get anything done from the convenience of one's mobile phone or portable computer. From sending emails, to organized Zoom® calls, to online payments, to remote gaming, all the way to the virtual machinations of the Metaverse®. These applications are far-flung and there is no stopping just yet. While the internet continues to make ease enjoyable for human livelihood, the use of optoelectronics sensors have also gained traction over their continued use in facial recognition technologies as well as the provision of precise navigation experience to automobiles through LiDAR systems.

The branch of study devoted to the practicality of these optoelectronics devices is called Si photonics. This technology integrates a suite of optical devices (lasers, modulators, waveguides and photodetectors) on a single Si platform while delivering cost-effective, compact, reliable and high-performance characteristics. Unfortunately, developing light emission capabilities on this platform has remained a constant challenge due to its incompatibility with currently used semiconductor materials. Although, III-V materials have achieved discrete light

emitting measures upon integration with Si substrates, the product of these hybridizations are both expensive and incompatible with standard semiconductor processing techniques. As a result, the need for a novel material that brings to reality the promised light emitting objective without the challenges associated with current practices, cannot be overemphasized.

The candidate materials for these light emission possibilities are the GeSn (Germanium-tin) and SiGeSn (Silicon-Germanium-Tin) alloys. These semiconductor materials evade the many challenges associated with III-Vs in that they are less-expensive, possess high-performance potentials while also covering an extensive wavelength range up to the mid and near infrared spectrum. Mr. Oluwatobi (Tobi) Olorunsola, a current doctoral (Ph.D.) fellow in the Microelectronics-Photonics program at the University of Arkansas. He has been working on understanding the optical and structural properties of (Si)GeSn heterostructures that aims at developing efficient Sn-based light emitters on Si platforms. He currently works in a research team led by Dr. Shui-Qing (Fisher) Yu, a Professor of Electrical Engineering at the University of Arkansas, Fayetteville. The overarching goal of this research is to develop efficient and high-performance Sn-based light emission and detection technologies that will surpass the current performance realities of current III-V devices.

Tobi's research focuses on improving the emission characteristics of GeSn bulk and quantum well through optimized heterostructure design, growth and advanced optical and structural studies. The outcome of which has given rise to an improved emission characteristics that allows for the measurement of the first-ever quantum efficiency of a SiGeSn/GeSn quantum well structure. The quantum efficiency (QE) parameter is a measure of the emission efficiency of a laser. It helps us quantify the performance of a light emitting device. "While there are other subtle ways of monitoring the GeSn material development progress, the QE metric provides a

more practical definition to the progress we've so far'' Tobi said. "This is an exciting stride in the history of the (Si)GeSn material development. It deserves a place of note on the timeline.'' Other aspects of Tobi's work also focus on solving other structural and optical challenges that will lead to the fuller realization of high-performance Sn-based devices for future commercial exploits in the fields of computing, data communication, detection and sensing.

Appendix D: Executive Summary of Newly Created Intellectual Property

This research is divided into three distinct thrusts. The first targets the improvement of the carrier confinement properties of SiGeSn QW samples using advanced design optimization strategies. The second thrust of this work investigates the stability requirements of GeSn bulk and quantum wells. The initial part of the stability exploration deals with the annealing study of bulk GeSn materials near the indirect-direct optical transition point, while the second sub-part investigates the intervention of Si/Sn diffusion (intermixing) within depth layers of MQWs. The third thrust aims to discover a suitable growth window for GeSn heterostructures through a systematic pressure dependent study. The major results of these dissertation thrusts are outlined below:

1st Thrust: Optical Property Study of Quantum Well Samples

1. QW confinement study based on thick (22 nm) vs. thin (9 nm) SiGeSn QW comparison
    i. Thicker well show improved carrier confinement (24 meV) and QW emission, reduced leakage
    ii. Enhanced emission allows for the first-ever estimation of GeSn QWs quantum efficiency (QE)
2. Separate Confined Heterostructure (SCH) QW study
    i. SCH QW design with competitive optical confinement at 56 meV (first time)

2nd Thrust: Annealing & Stability Investigations

3. GeSn bulk annealing study
    i. Established the connection between strain, composition, defect density and the PL before and after annealing.
    ii. Composition and level of strain influenced the separation between the indirect and direct optical transitions

iii. Competition between defect density and indirect-direct energy separation (ΔE) determine the impact of annealing on optical emission.

This part of the dissertation provides insight into what happens to the optical property of annealed GeSn bulk samples near the transition point.

4. Si/Sn intermixing during the growth of GeSn/SiGeSn MQWs

   i. PL and SIMS analysis show evidence of intermixing diffusion during growth, especially along the deeper GeSn/SiGeSn interfaces below the surface.

   ii. Intermixing and diffusion events can be pronounced for situations where higher growth temperatures are applied or for objectives with post-growth annealing requirements

3rd Thrust: GeSn Growth & Characterization

5. Pressure dependent growth optimization study

   i. Possible growth window exists between 10 and 15 Torrs.

Appendix E: Potential Patent and Commercialization Aspects of Listed Intellectual Property Item

E. 1 Patentability of Intellectual Property (Could Each Item be Patented)

The following items are considered first from the perspective of whether or not the items should be should be patented.

1. The GeSn/SiGeSn QW thick well design that achieved the enhanced should not be patented since similar designs has been utilized to investigate the same optical emission objective. Besides, the practicality of this QW design is may be considered incremental novelty the only difference in the design is the change in well width.
2. The SiGeSn/GeSn separate confinement heterostructure (SCH) QW design used to achieve superior carrier confinement and emission at low power should be considered for intellectual property protection. The structure is exclusively based on GeSn and SiGeSn material and is considered the first SCH structure to demonstrate such optical capability.
3. The experimental method and approach used to calculate the external and spontaneous quantum efficiency (EQE and SQE) has been implemented for a different material system (III-V) and should not be considered intellectual property material.
4. The X-ray method used in estimating the Sn composition, strain and defect density cannot be patented since the techniques has been applied to a wider range of semiconductor material system
5. The GeSn systematic growth optimization process has been applied to other growth objectives that targets material quality improvements. This cannot be patented.

E. 2 Commercialization Prospects (Should Each Item Be Patented)

The SiGeSn/GeSn separate confinement heterostructure (SCH) single QW design can be patented since it delivers superior carrier confinement and emission when compared to other

reference QW designs. This optical property improvement would favor the development of high-performance GeSn laser and other optoelectronics devices.

E. 3 Possible Prior Disclosure of IP

i) Not applicable

Appendix F: Broader Impact of Research

F. 1 Applicability of Research Methods to Other

The systematic method of solutions employed in this research will not only apply to problems in semiconductor materials physics but also the larger scopes of nanoscale material and device engineering. From the QW design strategies to the exploration of the complex relationships between GeSn/SiGeSn structural and optical material properties, as well as the growth optimization techniques of these Group IV alloys, the methods and approach discussed in this dissertation will provide a deeper understanding to the physics of materials with quasi-direct bandgap properties.

F. 2 Impact of Research Results on U.S. and Global Society

The understanding of the optical and structural properties of GeSn/SiGeSn bulk and QW materials is a step towards the realization of cheap, fast and reliable optoelectronics systems. With Silicon photonics at the brink of technological breakthrough, the integration of the GeSn materials on Si platforms will help develop a new suite of Si-based infrared lasers and detector device with accelerated market adoption for both U.S. and the global market at large. These device systems can potentially revolutionize the defense, consumer electronics, telecommunication and medical industries given their unique and diverse application metric. For example, Si-based infrared cameras can be harnessed for driverless-car technologies, enabling safer and clearer navigation optics. The finer application of these infrared technologies also applies extensively to military defense and space systems. Compared to their group III-V counterparts, GeSn devices are less expensive with high tolerance to radiation effects while also bagging the rare capability of providing better and competitive efficiency.

F. 3 Impact of Research Results on the Environment

Although traditional device processing methods requires the use of large volume chemical precursors for the growth and fabrication of semiconductor devices, the idea to miniaturize the GeSn devices while making them integrable to Si platforms makes for lesser use of these toxic substance since production is will be more discretized. Additionally, the extensive development of group-IV based photonic devices will prompt the reduction of mining activities of rare-earth minerals that are both toxic to humans, the environment and the versed ecosystem at large. An attempt to increase the energy efficiencies of these devices will also tantamount to lesser dependence and demands on fossil fuels thus creating a greener and cleaner environment.

Appendix G: Microsoft Project for MS MicroEP Degree Plan

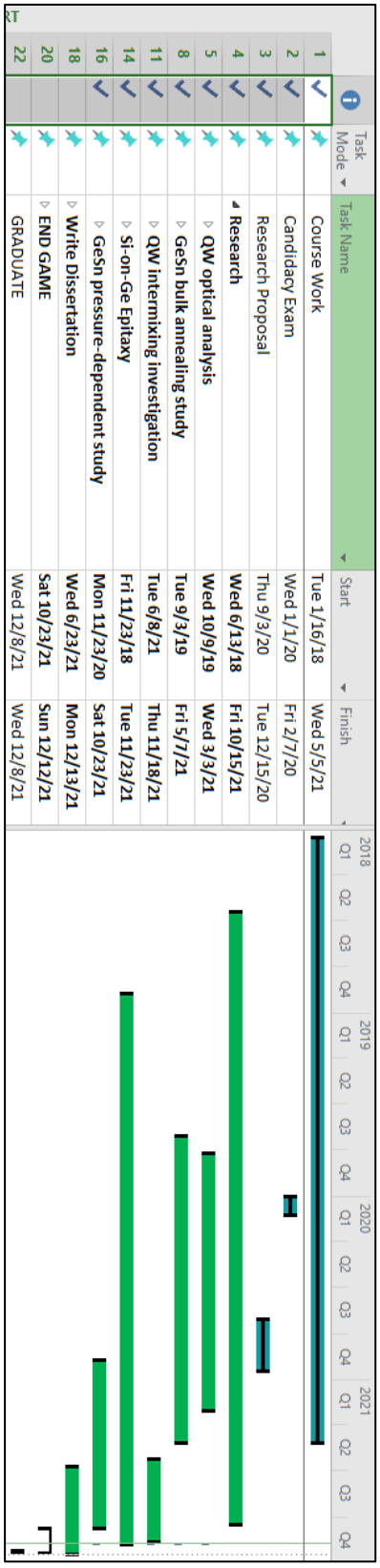

Appendix H: Identification of All Software Used in Research and Thesis Generation

Computer #1:
- Model Number: HP Laptop 17-by1xxx
- Serial Number: 5CG93704G5
- Location: Personal laptop
- Owner: Dr. Shui-Qing Yu

Software #1:
- Name: Microsoft 365 Apps for enterprise
- Purchased by: Electrical Engineering Department, University of Arkansas

Software #2:
- Name: Microsoft Project Professional 2013
- Provided by: Electrical Engineering Department, University of Arkansas

Software #3:
- Name: Zotero

Purchased by: Free download available from Zotero.org

Software #4
- Name: OriginPro 2021 (student version)
- Serial Number: GA3S4-6089-7245285
- Purchased by Oluwatobi Olorunsola

Software #5
- Name: GNU Image Manipulation Program (GIMP)
- Purchased by: Free download available from gimp.org

Computer #2:
- Model Number: Dell Vostro
- Serial Number: 52M6XK1
- Location: ENRC Room 2923
- Owner: Dr. Shui-Qing Yu

Software #1:
- Name: SynerJY with built-in Origin software
- Purchased by: Dr. Shui-Qing Yu

Computer #3:
- Model Number: Dell Inspiron
- Serial Number: 52M6XK1
- Location: ENRC Room 2923
- Owner: Dr. Shui-Qing Yu

Appendix I: All Publications Published, Submitted, and Planned

I.1. Articles in Refereed Journals

2021

[3]. Oluwatobi Olorunsola, Stanchu H, Ojo S, Pandey K, Said A, Margetis J, Tolle J, Kuchuk A, Mazur Y I, Salamo G and Yu S-Q 2021 "Impact of Long-Term Annealing on Photoluminescence from Ge1−xSnx Alloys" *Crystals* 11 905

[2]. Oluwatobi Olorunsola, Wei Du, Solomon Ojo, Grey Abernathy, Yiyin Zhou, Sylvester Amoah, P.C. Grant, Wei Dou, Joe Margetis, John Tolle, Baohua Li, Yong-Hang Zhang, and Shui-Qing Yu, "Investigation of SiGeSn/GeSn/SiGeSn single quantum well with enhanced well emission" Nanotechnology

2020

[1]. Seyedeh Fahimeh Banihashemian, Joshua M Grant, Abbas Sabbar, Huong Tran, Oluwatobi Olorunsola, Solomon Ojo, Sylvester Amoah, Mehrshad Mehboudi, Shui-Qing Yu, Aboozar Mosleh, Hameed A Naseem "Growth and characterization of low-temperature $Si_{1-x}Sn_x$ on Si using plasma enhanced chemical vapor deposition," Opt. Mater. Express, vol. 10, no. 9, p. 2242, Sep. 2020, doi: 10.1364/OME.398958.

I.2. Articles and Abstracts in Conference Proceedings

2021

[4]. Wei Du, Oluwatobi Olorunsola, Solomon Ojo, Grey Abernathy, Yiyin Zhou, Sylvester Amoah, P.C. Grant, Wei Dou, Joe Margetis, John Tolle, Baohua Li, Yong-Hang Zhang, and Shui-Qing Yu, Investigation of SiGeSn quantum well for the development of Si-based lasers, 2021 Air-Force Research Lab (AFRL) workshop, September 2021

[3]. Oluwatobi Olorunsola, Wei Du, Solomon Ojo, Grey Abernathy, Yiyin Zhou, Sylvester Amoah, P.C. Grant, Wei Dou, Joe Margetis, John Tolle, Baohua Li, Yong-Hang Zhang, and Shui-Qing Yu, Study of SiGeSn/GeSn/SiGeSn single quantum well towards all-Group-IV Lasers, 15th Mid Infrared Optoelectronics Materials and Devices (MIOMD) Conference, 1-3 September 2021

I.3. Conference Presentations

2019

[2]. Jake Bass, Grey Abernathy, Sylvester Amoah, Huong Tran, Samir Saha, Solomon Ojo, Oluwatobi Olorunsola, and Shui-Qing (Fisher) Yu, Towards Fully-Integrated Optical Systems, 2019 CHECCS IMWP Summer (meeting), August 11-13, Fayetteville, AR (2019)

[1] Oluwatobi Olorunsola, Perry Christian Grant, Wei Dou, Bader Alharthi, Joshua Mathew Grant, Huong Tran, Grey Abernathy, Aboozar Mosleh, Wei Du, Baohua Li, Mansour Mortazavi, Hameed Naseem, and Shui-Qing (Fisher) Yu, Towards Fully-Integrated Optical Systems, 2019 CHECCS IMWP Summer (meeting), August 11-13, Fayetteville, AR (2019)

I.4. Submitted

[3] Oluwatobi Olorunsola, Hryhorii Stanchu, Abdulla Said, Solomon Ojo, Emmanuel Wangila, Mohammad Alavijeh, Gregory Salamo, and Shui-Qing Yu, "Optical and structural properties of multiple quantum wells for infrared optoelectronics"

[2]. Oluwatobi Olorunsola, Abdulla Said, Solomon Ojo, Grey Abernathy, Samir Saha, Emmanuel Wangila, Hryhorii Stanchu, Joe Margetis, John Tolle, Wei Du, Baohua Li, and Shui-Qing Yu, "Enhanced carrier confinement of GeSn single quantum well towards all-group-IV photonics applications, APL

[1]. Joshua Grant, Grey Abernathy, Oluwatobi Olorunsola, Solomon Ojo, Sylvester Amoah, Emmanuel Wangila, Samir K Saha, Abbas Sabbar, Wei Du, Murtadha Alher, Baohua Li, and Shui-Qing "Growth of pseudomorphic GeSn at low pressure with Sn com-position of 16.7%" Submitted to Materials (2021)

I.5. Planned

2021

[1]. Oluwatobi Olorunsola, Grey Abernathy, Solomon Ojo, Grey Abernathy, P.C. Grant, Wei Dou, Bader Alharthi, Joe Margetis, John Tolle, Wei Du, Baohua Li, and Shui-Qing Yu, "A Review of GeSn/SiGeSn Quantum Well Materials and Devices''

Appendix J: Publishing Agreements/Permissions

Crystals Journal

Re: Permission for reproduction in dissertation

Crystals <crystals@mdpi.com>
Tue 8/17/2021 1:17 AM
To: Oluwatobi Olorunsola <ogolorun@uark.edu>
Cc: constanze.schelhorn@mdpi.com <constanze.schelhorn@mdpi.com>

Dear Dr. Olorunsola,

Thanks for your kindly reply.

No special permission is required to reuse *all or part* of this article, including figures and tables.

For articles published under an open access Creative Common CC BY license, any part of the article may be reused without permission *provided that the original article is clearly cited*. Reuse of an article does not imply endorsement by MDPI.
https://nam11.safelinks.protection.outlook.com/?url=https%3A%2F%2Fwww.mdpi.com%2Fauthors%2Frights&data=04%7C01%7Cogolorun%40uark.edu%7C92557acb96b942c39afe08d961467e87%7C79c742c4e61c4fa5be89a3cb566a80d1%7C0%7C0%7C637647778700589386%7CUnknown%7CTWFpbGZsb3d8eyJWIjoiMC4wLjAwMDAiLCJQIjoiV2luMzIiLCJBTiI6Ik1haWwiLCJXVCI6Mn0%3D%7C3000&sdata=vvoARq6Nf2xQMusAB5f49X0yaniliE2tJWf0L63QCY4%3D&reserved=0

I hope that you find the information above useful.

Best regards,

Ms. Autumn Du
Managing Editor, MDPI Wuhan
Email: autumn.du@mdpi.com

MDPI Branch Office, Wuhan
5.5 Creative Industry Park, 25th Floor, No.6 Jingan Road, 430064 Wuhan,
Hubei Province, China
Tel.: +86 27 8780 8658

On 2021/8/17 5:22, Oluwatobi Olorunsola wrote:
> Greetings,
>
> I would like to ask if any permission for to reuse my first-authored
> Crystals journal in my dissertation. If yes, could you please provide
> permission for me?
>
> The article is published in Crystals:
>
> Title: Impact of Long-Term Annealing on Photoluminescence from Ge1−xSnx
> Alloys
> Crystals 2021, 11(8), 905; https://nam11.safelinks.protection.outlook.com/?url=https%3A%2F%2Fdoi.org%2F10.3390%2Fcryst11080905&data=04%7C01%7Cogolorun%40uark.edu%7C92557acb96b942c39afe08d961467e87%7C79c742c4e61c4fa5be89a3cb566a80d1%7C0%7C0%7C637647778700758638%7CUnknown%7CTWFpbGZsb3d8eyJWIjoiMC4wLjAwMDAiLCJQIjoiV2luMzIiLCJBTiI6Ik1haWwiLCJXVCI6Mn0%3D%7C3000&sdata=2AOSLLdercsC8MzDO72iz5q3pqTR2IlpT8IarXdIGNM%3D&reserved=0
> <https://nam11.safelinks.protection.outlook.com/?url=https%3A%2F%2Fdoi.org%2F10.3390%2Fcryst11080905&data=04%7C01%7Cogolorun%40uark.edu%7C92557acb96b942c39afe08d961467e87%7C79c742c4e61c4fa5be89a3cb566a80d1%7C0%7C0%7C637647778700758638%7CUnknown%7CTWFpbGZsb3d8eyJWIjoiMC4wLjAwMDAiLCJQIjoiV2luMzIiLCJBTiI6Ik1haWwiLCJXVCI6Mn0%3D%7C3000&sdata=2AOSLLdercsC8MzDO72iz5q3pqTR2IlpT8IarXdIGNM%3D&reserved=0>
>
> Impact of Long-Term Annealing on Photoluminescence from Ge1−xSnx Alloys
> <https://nam11.safelinks.protection.outlook.com/?url=https%3A%2F%2Fdoi.org%2F10.3390%2Fcryst11080905&data=04%7C01%7Cogolorun%40uark.edu%7C92557acb96b942c39afe08d961467e87%7C79c742c4e61c4fa5be89a3cb566a80d1%7C0%7C0%7C637647778700758638%7CUnknown%7CTWFpbGZsb3d8eyJWIjoiMC4wLjAwMDAiLCJQIjoiV2luMzIiLCJB

> Best regards,
>
> _____
>
> Oluwatobi Olorunsola, Ph.D. Candidate
>
> Microelectronics-Photonics Program
>
> Department of Electrical Engineering
>
> University of Arkansas
>
> Fayetteville, AR 72701
>
> Cell: (309) 868-6920
>
> Email:ogolorun@email.uark.edu <mailto:ogolorun@email.uark.edu>

Nanotechnology

"Assignment of copyright and publication agreement IOP Publishing Limited ("IOP") agrees to publish:

Manuscript Title: Investigation of SiGeSn/GeSn/SiGeSn single quantum well with enhanced well emission (the "Article") written by

Names of all authors: Oluwatobi Olorunsola, Wei Du, Solomon Ojo, Grey Abernathy, Yiyin Zhou, Sylvester Amoah, P.C. Grant, Wei Dou, Joe Margetis, John Tolle, Baohua Li, Yong-Hang Zhang, and Shui-Qing Yu ("the Named Authors") in the following journal Nanotechnology ("the Journal")

Name of copyright owner(s) (if not the Named Author(s) – see Important Information

above): ("the Copyright Owner")

IOP Ref: NANO-129960.R1

Part 1 - Publication on a Subscription basis

1.1 In consideration for acceptance and publication of the Article, the Named Authors of the Article and/or the Copyright Owner hereby assign, where necessary by present assignment of future copyright, to IOP with full title guarantee the entire copyright in all original material published as part of the Article (which expression includes but is not limited to the text, abstract, tables, figures and graphs, related corrigenda or "comments" and multimedia content but excludes any other item referred to as supplementary material and/or any video abstract) throughout the world for the full term of copyright (including any extensions or renewals thereof) for all media and formats, whether known or unknown. Such assignment shall be effective only if the Article (or any resubmission of the Article) is accepted for publication. For the avoidance of doubt, copyright does not subsist in any fundamental data underlying the Article and nothing in this agreement is intended to limit access to or use of such data.

1.2 If the Article, or any part of it, is protected by Crown copyright, in consideration for acceptance and publication of the Article, the relevant Named Authors and the relevant originating department or agency hereby grant IOP a non-exclusive royalty-free worldwide freely transferrable license for the full term of copyright (including any extensions or renewals thereof) for all media and formats, whether known or unknown, to do in relation to the Article all acts restricted by copyright worldwide including, but not limited to, the right of action under section 101A of the Copyright Designs and Patents Act 1988. Such license shall be effective only if the Article is accepted for publication.

1.3 If all the Named Authors are employees of the US Government, they represent and warrant to IOP that the Article was prepared as part of their official duties. In such circumstances, or where the Article was created as part of a work for hire, none of the original content within the Article is subject to copyright protection as it is in the public domain.

1.4 In consideration for acceptance and publication of the Article, the Named Authors and/or the Copyright Owner hereby grant IOP a royalty-free non-exclusive worldwide freely transferrable license for the full term of copyright (including any extensions or renewals thereof) to do in relation to any supplementary material not deemed to be part of the Article and/or any video abstract all acts restricted by copyright worldwide. This shall include, but not be limited to, making the material available under any license that IOP deems appropriate for purposes including, but not limited to, the maximization of visibility and the long-term preservation of the content.

1.5 Each of the Named Authors consents to all publication and processing of their personal data by IOP, as that data is displayed on the Article, including, but not limited to, the names and email addresses of the Named Authors. Accordingly, the Named Authors shall not object on data protection grounds to the use of their personal data on the Article wherever IOP chooses to display it, whether itself or via a third party.

Representations and warranties

2.1 The Copyright Owner and/or the Submitting Author on behalf of the Named Authors (as appropriate) represent and warrant that:

2.1.1 the Article is the original work of the Named Authors;

2.1.2 the Article has not been published previously in any form, other than in accordance with our Preprint pre-publication policy;

2.1.3 each of the Named Authors has made a material contribution to the conception and/or writing of the Article, has received the final version of the Article, has agreed to its submission on the terms contained herein and takes responsibility for it and submission has been approved as necessary by the authorities at the establishment where

the research was carried out;

2.1.4 the Submitting Author completes and returns this agreement as authorized agent for and on behalf of all the Named Authors and the Copyright Owner (as applicable) and has the full power to enter into this agreement and to make the grants and assignments it contains;

2.1.5 the Article has not been and shall not be submitted to another publisher prior to withdrawal or rejection by IOP;

2.1.6 the Article does not infringe any third-party rights, it contains nothing libelous or unlawful, all factual statements are to the best of the Named Authors' knowledge true or based on valid research conducted according to accepted norms and all required permissions have been obtained in writing;

2.1.7 the Article expressly acknowledges any third-party funding and/or potential conflicts of interest; and

2.1.8 any supplementary material or video abstract is the original work of the Named Authors, or is the property of the Copyright Owner, or permission has been obtained from its owner(s) for its publication by IOP and permission has been obtained for the inclusion of any third-party content.

2.2 The Named Authors and/or the Copyright Owner (as appropriate) indemnify and will keep indemnified IOP against all costs and expenses suffered or incurred by IOP as a result of and/or arising out of any breach of the representations and/or warranties in this section 2.

The Named Authors' rights

173

3.1 IOP grants the Named Authors the rights specified in paragraphs 3.2 and 3.3. All such rights must be exercised solely for non-commercial purposes. Where possible, any use should display citation information and IOP's copyright notice, and, for electronic use, best efforts must be made to include a link to the online abstract in the Journal.

Exercise of the rights in paragraph 3.2 may use the peer reviewed, edited, formatted and

typeset version of the Article including any tagging, indexing and other enhancements published by IOP and/or its licensors ("Final Published Version").

Exercise of the rights referred to in paragraph 3.3 must not use the Final Published Version and extend only to the version of the Article accepted for publication including all changes made as a result of the peer review process, and which may also include the addition to the article by IOP of a header, an article ID, a cover sheet and/or an 'Accepted Manuscript' watermark, but excluding any other editing, typesetting or other changes made by IOP and/or its licensors (the "Accepted Manuscript") and must be accompanied by the following statement of provenance:

'This is the Accepted Manuscript version of an article accepted for publication in Nanotechnology. IOP Publishing Ltd is not responsible for any errors or omissions in this version of the manuscript or any version derived from it. The Version of Record is available online at [insert DOI].'

3.2 The rights are:

3.2.1 To make copies of the Final Published Version of the Article (all or part) for teaching purposes;

3.2.2 To include the Final Published Version of the Article (all or part) in a research thesis or dissertation provided it is not then published commercially;

3.2.3 To make oral presentation of the Final Published Version of the Article (all or part) and to include a summary and/or highlights of it in papers distributed at such presentations or in conference proceedings; and

3.2.4 To use original figures and text from the Final Published Version of the Article falling within the quota outlined in and subject to the STM Permissions Guidelines (http://www.stmassoc.org/permissions-guidelines/) at the relevant time in force.

For the avoidance of doubt, the Named Authors retain all proprietary rights in the Article other than copyright.

3.3 Additional rights of the Named Authors are to:

3.3.1 Use the Accepted Manuscript (all or part) without modification in personal

compilations of the Named Authors' own works (provided not created by a third party publisher); and 3.3.2 Include the Accepted Manuscript (all or part) on the Named Authors' own Personal Website(s), institutional website(s), repositories, Scientific Social Networks and third-party websites provided that this is fully in accordance with the Author Rights set out at the following URL legal.ioppublishing.org/author-rights on the date of submission of the agreement.

Miscellaneous

4. To the extent that there are moral rights in the Article, all the Named Authors expressly reserve and assert their moral rights to be identified as the authors of the Article.

5. The Named Authors and/or the Copyright Owner shall execute such further documents, and take such actions and do such things, as may be requested by IOP at IOP's reasonable expense to give full effect to the terms of the agreement.

174

6. For the avoidance of doubt, the grants and assignment envisaged herein shall become effective only upon acceptance of the Article for publication. In the event that the Article is withdrawn prior to acceptance, or is rejected, this agreement shall have no effect and no party shall be bound by it.

7. The agreement shall be governed by English Law and subject to the non-exclusive jurisdiction of the English courts.

Confirmation

8. By selecting to publish on a subscription basis, the Submitting Author is responsible for ensuring that, where relevant all Named Authors, who are affiliated to a university/institution which has an open access policy which is incompatible with IOP's green open access policy, obtain a waiver for the Article from their institution or university's open access policy and retain such waiver as evidence of compliance. These Named Authors agree that they shall obtain such waivers and provide them to IOP promptly on request.

9. By typing the Submitting Author's name into the box at Part 3 below and clicking

"Submit", the Named Authors agree to these terms. The Authorized Signatories of any third party Copyright Owner(s) and/or the Submitting Author agree, on behalf of such Copyright Owner(s), to these terms by typing the Copyright Owner's name into the "Copyright Owner" box at the top of the page."